UNIVERSIDAD COMPLUTENSE DE MADRID

DEPARTAMENTO DE FÍSICA ATÓMICA, MOLECULAR Y NUCLEAR

Observation of the Monoceros Loop SNR with the HEGRA system of Čerenkov Telescopes

Ph.D. Thesis

by

Fabrizio Lucarelli

supervised by

Dr. **María Victoria Fonseca González**
Universidad Complutense Madrid
Madrid (Spain)

Dr. **Alexander Konopelko**
Max Planck Institut für Kernphysik
Heidelberg (Germany)

Abstract

The HEGRA collaboration has built one of the most powerful instrument to detect very high energy photons (E> 500 GeV) from astrophysical sources.

In this PhD thesis, I will review the possibility of the HEGRA system of Čerenkov telescopes in observation of extended γ-rays emission from supernova remnants (SNRs) (Chapter 6). By means of very detailed Monte Carlo simulation, we show that the detector is still very efficient for γ-rays -induced cascade coming off the telescopes axis, as could be the case of those ones emitted by SNRs.

As practical study, we observed a very extended shell-type SNRs, the Monoceros Loop SNR, which is supposedly to interact with a very dense molecular cloud, the Rosette Nebula. The data analysis (Chapter 7), based on very sophisticated techniques of background estimation, has shown the presence of hints of γ-rays extended emission.

A brief review of the *γ-rays astronomy* and the sources of very high energy photons have been given in the first Chapter. The technique to detect VHE photons by ground-based telescopes and the physical processes involved are given in Chapter 2 and 3. Chapter 4, is explicitly dedicated to the description of the system of five imaging atmospheric Čerenkov telescopes, which was deployed at La Palma Canary Islands and was shutdown on Sept. 2002.

As one of the main goal of the next generation of Čerenkov telescopes is to lower the energy threshold down to the sub-TeV energy range, we also implemented a technique to lower the energy threshold of the HEGRA system (Chapter 5). This technique made use of an advanced *topological trigger* and permitted to lower the energy threshold by a factor 1.4 without any hardware changes.

Contents

Chapter 1

The highest energy photons detected from space

1.1 Historical background

The study of astrophysical sources of photons with $E > 10^6$ eV, the *γ-ray astronomy*, is a relative new field and still in an explorative phase[1]. Historically, this new field has been developed along with the study of the origin of the cosmic rays (CR), when it became clear that high energy photons were emitted in the same CR acceleration processes. Indeed, the main goal of this new branch of astrophysics was (and, still it is) to locate the sources of CR particles. Since γ-rays propagate undeviated by intergalactic and interstellar magnetic fields, they can be traced back to the place of emission, which is also thought to be the site of CR acceleration.

Two distinct types of detectors are employed in γ-ray astronomy: satellite-based and ground-based detectors. The use of either the first one or the second one marks a difference in the energy range of the photons to be detected: satellites are sensitive to the *High Energy (HE)* γ-rays range, 30 MeV to 30 GeV, while ground-based instruments detect *Very High Energy (VHE)* γ-rays, covering the range between tenths of GeV up to 50 TeV [3]. It is usually referred as "TeV γ-ray astronomy" the study of sources of VHE γ-rays[2].

[1] For an exhaustive review on γ-ray astronomy see [1] [2]

[2] Less frequent is the citation of "PeV or EeV astronomy" since any or very few sources have been

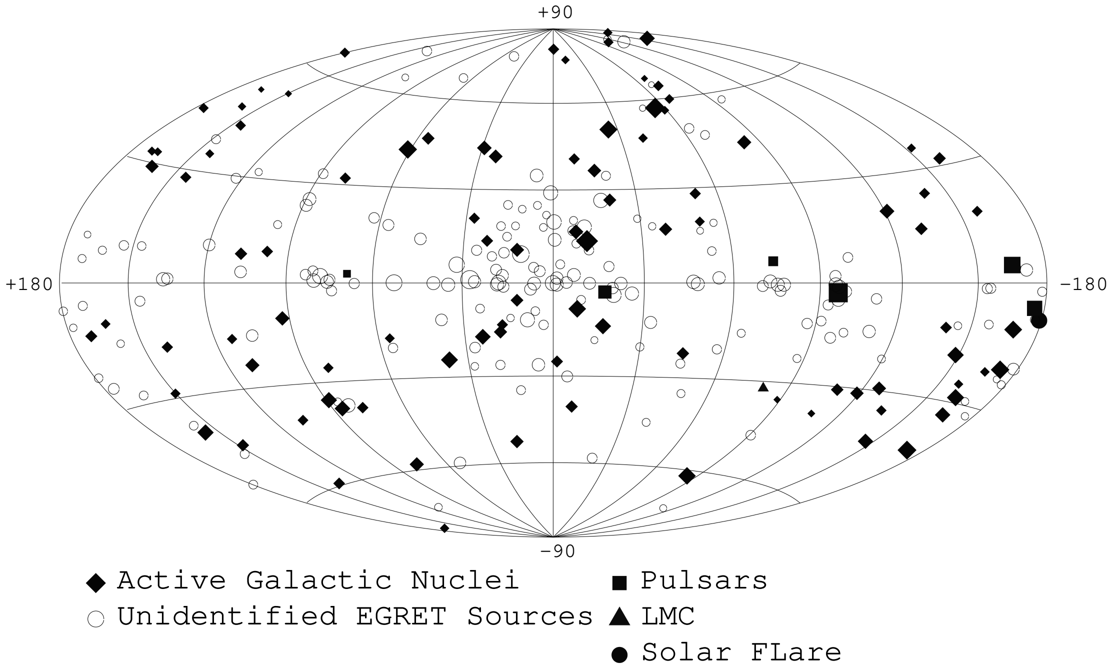

Figure 1.1: *The sky at $E > 100$ MeV seen by the EGRET experiment on board of the CGRO satellite (from the 3rd EGRET catalogue [5]).*

Satellites detect HE γ-rays via photon conversion, tracking the resulting electron-positron pair to determine the photon arrival direction. The first detections of high energy γ-rays by satellite-based experiments were due to the SAS-2 and COS-B satellites. They detected photons in the range 35 MeV-5 GeV from 25 point-like sources and diffuse emission from the galactic plane.

To date, the most sensitive HE γ-ray telescope has been the EGRET experiment on board the Compton Gamma Ray Observatory [4], with more than 100 sources detected in the energy range 30 MeV - 30 GeV (see Fig. 1.1), most of them yet unidentified.

The ground-based detectors use a different technique to detect VHE γ-rays, as we shall see more diffusively in the next chapters. Due to the relative weakness of the sources and the low sensitivity of the actual instruments, the number of TeV sources is still quite low (see Fig. 1.2).

It is worthwhile to stress that, though the techniques used are distinct, the phys-

detected to emit photons with energies greater than 50 TeV.

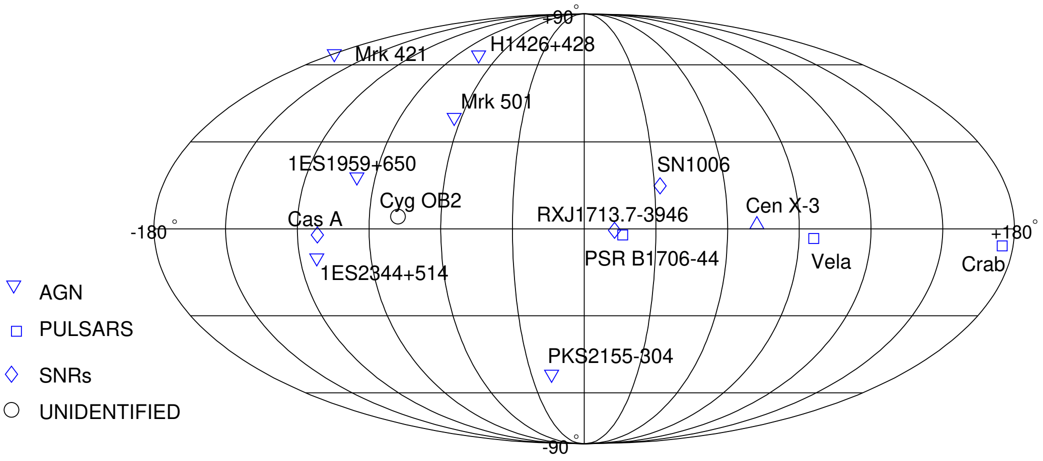

Figure 1.2: *The sky seen at energies $E > 100$ GeV by ground-based experiments.*

ical processes addressed by the satellite- and ground-based instruments are the same. In what follows, we shall make a brief review of the physics of the main γ-rays emitters.

1.2 Cosmic Accelerators and VHE γ-rays

VHE and HE γ-rays have energies ten order of magnitudes greater that the typical optical photons ($E \sim 1$ eV), therefore typical thermal production mechanisms of low-energy photons cannot be applied in this case. The emission of high energy γ-rays always involves extreme and violent processes where intense magnetic and gravitational fields play a crucial role and new physics may be also required to explain it. The power source can be a very massive black hole, like in the active galactic nuclei, or a pulsar, a neutron rotating star, as in the Crab Nebula. Since γ-rays are neutral, the emission can only occur as result of secondary particles interactions. The primary particles, either

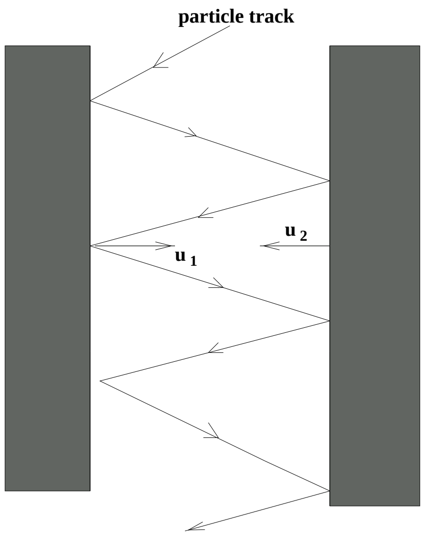

Figure 1.3: *The first-order Fermi acceleration mechanism.*

leptonic or hadronic in nature, are accelerated by Fermi acceleration mechanisms and can gathered up to 10^{20} eV in energy. The acceleration can take place at the shock front region in a extreme astrophysical environment (like an expanding supernova shell or an accretion region of matter around a black hole or a neutron star). The particle, being trapped between the upstream and downstream region of the shock, gains energy each time it crosses the shock front, as it were reflected by an approaching wall (see Fig. 1.3). This mechanism is known as *first-order Fermi acceleration* [6] [7]. The energy spectrum of the accelerated particles population typically follows a power law, which is also reflected in the secondary products. The *second-order Fermi acceleration mechanism* [8] is much less efficient and slow: it takes place in the interstellar medium between clouds of plasma and charged particles, which gain energy when the cloud moves towards them and loose it when the cloud moves away. Acceleration of particles can occur as well via electromagnetic processes, in pulsar or close to an accretion disk of matter.

The acceleration of particles is closely related with the CR origin. The accelerated plasma (protons or electrons) can interact with ambient photons or matter surrounding the shock region, leading to production of secondary particles as neutral pions which decay into γ-rays, or up-scattering the low-energy ambient photons to γ energies by Inverse Compton effect. If the density of matter surrounding the acceleration site is not such as high[3], γ-rays can escape. Thus, observation of VHE and HE γ-rays can bring us direct information about the CR accelerator sites.

1.3 Sources of VHE γ-rays

All the γ-rays sources detected up to now by means of satellite or ground-based instruments involve astrophysical object where acceleration processes are taking place, like active galactic nuclei, pulsars, X-rays binaries and so on. In what follows, we shall briefly review each type of sources (or potential sources) of γ-rays, focusing our attention to the class of objects detected at TeV energies.

[3]Less than ~ 1 radiation length, which is defined as the path the γ-rays travel before their flux decrease by $1/e$ due to pair production.

1.3.1 Active Galactic Nuclei (AGN)

In general, the term AGN states for a galaxy where the power emitted from the central bulge is several orders of magnitude greater than that one emitted from the rest of the host galaxy. There are several divisions in classes and sub-classes, the most important being the distinction between radio-loud and radio-quiet galaxies, based on the different fraction of luminosity emitted in the radio band ($1/10^3$ and $1/10^6$ of the total luminosity, respectively).

A further distinction between these two classes is found in the high grade of light polarization and variability in the optical band of the radio-loud AGNs, which also show in their emission spectrum both the thermal component and the non-thermal one. Around 90% of the AGNs are radio-quiet. A typical representation of a radio-loud AGN is that one reported in Fig. 1.4: a supermassive central black hole, with $M \sim 10^7 - 10^{10} M_\odot$[4], surrounded by a thick disk of matter, the accretion disk, and two pair of well-collimated jets of plasma ejected perpendicularly to the accretion disk.

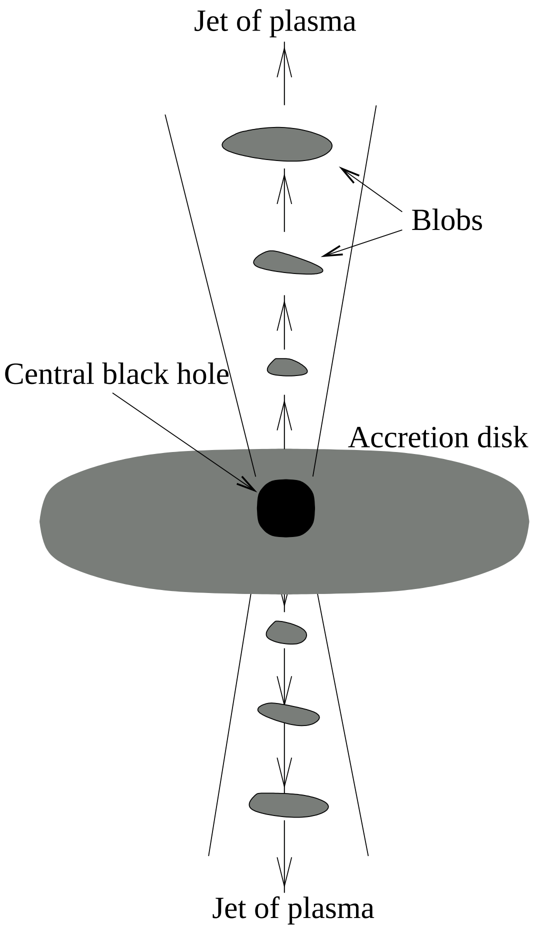

Figure 1.4: *The unified AGN model.*

The jets are mainly composed by electrons and protons accelerated via Fermi mechanisms at the base of the jet, close to the black hole. They interact with the dense photon field surrounding the nucleus giving the whole observed electromagnetic spectrum, from the radio to the TeV γ-rays.

Most of the different AGN classifications derives from the different viewing angles to the observer with respect to the rotation axis. Those AGNs with the relativistic

[4] $1\ M_\odot = 1$ solar mass $= 2 \times 10^{33}$ gr

jets forming a small angle with the line of sight are named *blazars*.

The observational properties of the blazars are directly related with the Doppler boosting of the relativistic jet towards the observer. Given the Doppler boosting factor $\delta \equiv [\Gamma(1-\beta\cos\theta)]^{-1}$, where Γ is the bulk Lorentz factor of the plasma in the jet and θ is the angle between the jet and the line of sight to the observer, they can be summarized as follows: i) blobs of plasma moving at superluminal speed (that is, apparent motion that is greater than the speed of light); ii) enhancement of the observed luminosity by a factor $\delta^{2+\alpha}$, where α is the power law spectral index of the source luminosity[5] [9]; iii) time scales of the variability of the emission reduced by a factor $1/\delta$ (time scales decrease as the viewing angle decreases).

BL Lacs objects belong to this class of AGNs, and are the only class observed to emit VHE photons. There are mainly two models explaining the emission of TeV γ-rays from blazars: the leptonic models [10] [11] and the hadronic ones [12] [13]. In the leptonic scheme, relativistic electrons interact with the ambient photon field surrounding the central engine and scatter these low energy photons to higher energies via Inverse-Compton (IC) effect. In case the target of the dump interaction is formed by the synchrotron-radiation photons emitted by the same accelerated electrons, we refer to Self-Synchrotron-Compton (SSC) models. In the hadronic models, proton beams collide with the ambient photons, producing secondary pions via photo-production of the Δ resonance, which decay and emit γ-rays and neutrinos ($p\,\gamma \rightarrow \Delta \rightarrow \pi^0 \rightarrow \gamma\,\gamma$).

1.3.2 Pulsars

Pulsars are rapidly rotating neutron stars, with periods between a few milliseconds and a few seconds, originated from a supernova explosion. The neutron star has a maximum mass of $\sim 3\ M_\odot$ and a radius up to 10 km. The magnetic fields are very intense, with values up to $10^{11}-10^{12}$ G.

The star co-rotating magnetosphere generates strong electric fields which are able to extract electrons (or positrons, depending on the magnetic field sign) from the star surface. The plasma of electrons and positrons redistributes itself in the magneto-

[5] In case of a single blob inside the jet moving towards the observer, the enhancement factor is $\delta^{3+\alpha}$. By integrating over the area of the jet gets to the factor reported in the text.

sphere in such a way that $\mathbf{E}\cdot\mathbf{B}=0$, making the particle acceleration prohibited. The radius where the magnetic field lines rotate at the speed of light sets the light cylinder: beyond that, the field lines are opened and starts the pulsar wind region (see Fig 1.5).

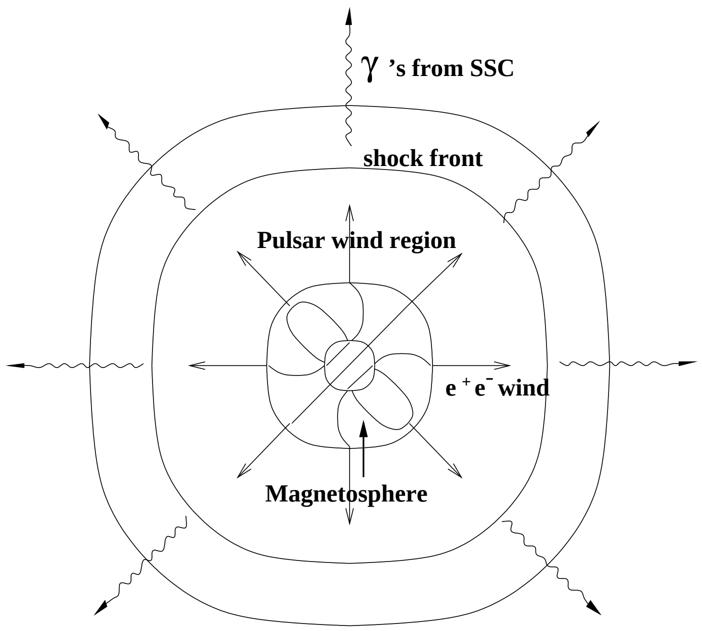

Figure 1.5: *Schematic view of a plerion.*

The acceleration becomes possible only in areas of the magnetosphere devoid of plasma, where $\mathbf{E}\cdot\mathbf{B}\neq 0$. These regions can appear near the magnetic poles (polar cap models [20] [21]) or in vacuum gaps near the light cylinder (outer gap models [22] [23]). The observed pulsed emission from the radio wavelengths to the GeV energy range is thought to originate from these regions.

Up to now, TeV γ-rays have been only detected from *plerions*, pulsars embedded in the nebula originating from the supernova explosion. The TeV emission comes from the high energy electrons and positrons accelerated by the intense magnetic field of the central pulsar and which escape the magnetosphere along the open field lines. When they reach the pulsar wind region, they interact with the ambient photons within the nebula (being the same synchrotron photons emitted by the accelerated particles (self-Compton model [24]) or the microwave background radiation) which are up-scattered to TeV energies by Inverse Compton effect. The Crab Nebula [25], Vela [26] and PSR 1706-44 [27] belong to this sub-class of pulsars.

1.3.3 Supernova remnants

Supernova remnants (SNRs) are widely believed to be one of the sites of cosmic rays acceleration up to $E < 10^{14} - 10^{15}$ eV. The acceleration of particles by first-order Fermi shock mechanism in the expanding shell naturally explains the observed cosmic ray spectrum and its composition. Besides, the SNRs are the only galactic site with sufficient power to explain the observed cosmic ray energy density. Detection of TeV photons from these objects represents a key feature of a galactic cosmic ray acceleration site [14] [15]. If matter is accelerated within a SNR, it is expected that protons interact with the ambient matter (either ejected from the supernova explosion or nearby molecular clouds) giving γ-rays photons via π^0 decay: $pp \to \pi^0 \to \gamma\gamma$.

Despite the theoretical expectations, only three SNRs have been detected as TeV γ-rays emitters: SN1006 [16], RX J1713.7-3946 [17] and Cassiopeia A [18]. For SN1006 and Cas A, the TeV emission is explained by non-thermal relativistic electrons which emit γ-rays via IC effect over the cosmic microwave background photons, whereas the measured TeV energy spectrum of RX J1713.7-3946 matches that one expected in the case of hadronic origin of the emission, yet there is great debate about that [19].

We will talk more deeply of cosmic ray and TeV γ-rays emission from SNRs in § 7, focusing our attention to the particular case in which an expanding supernova shell collides with a nearby molecular cloud, which is the case of the Monoceros Loop - Rosette Nebula region, the main subject of this thesis.

1.3.4 X-ray binary sources

X-ray binary systems are composed by a neutron star and a main sequence star rapidly rotating around each other. Matter flows from the star companion onto the neutron star forming an accretion disk around it. The matter spirals inward along the open field lines onto the magnetic poles of the neutron star, creating "hot spots" with temperature of order $T \simeq$10-15 keV. If the rotation and magnetic axes are not aligned, an X-ray pulse is observed as the magnetic poles sweep past the observer.

A possible scenario for pulsed γ-rays emission (from decay of neutral pions) is that one shown in Fig 1.6 (a). Protons accelerated in the polar cap or outer gap

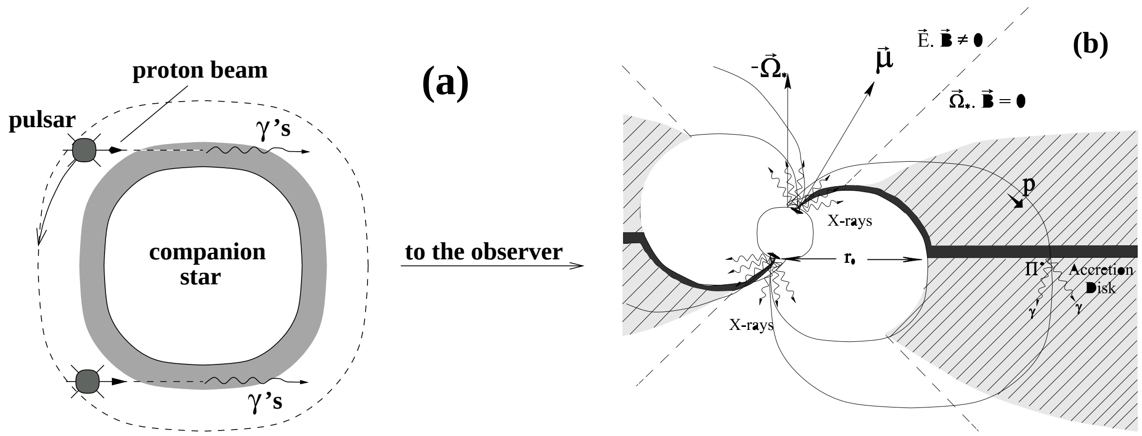

Figure 1.6: *(a) Proton beam dump between a pulsar and its companion star; (b) π^0 γ-rays from proton beam dump onto an accretion disk around a pulsar (from [30]).*

regions of the pulsar can dump on the near star companion atmosphere producing π^0 which decay in γ's [28]. Alternatively, the proton beam can collide with the accretion disk producing γ's by π^0 decay [29] [30] (Fig 1.6 (b)).

Some binary systems show the presence of relativistic jets, similar to those ones observed in a radio-loud AGN, obviously on a galactic scale. They are also known as *micro-quasars*. HE γ-rays are expected from non-thermal accelerated particles inside the jet: indeed, some of the unidentified EGRET source can be associated with micro-quasars [31] [32]. In the early 1980s, several claims of TeV and PeV γ-rays detection were reported from X-ray binary systems (Cygnus X-3, Hercules X-1) which have not been confirmed by the more recent ground-based TeV instruments. Very recently the HEGRA collaboration has reported detection of TeV emission near the core of the Cygnus OB2 association [33]. The TeV emission can be related with stellar winds emitted by the young stars within the association and colliding with nearby molecular clouds (γ's via neutral pions decay) but can also be related with a mini-jet coming from the Cygnus X-3 binary system (70 pc away), aligned with the TeV source.

1.3.5 Gamma Ray Bursts

Since the time of their discovery, in the 1960s, the Gamma Ray Bursts (GRBs) have represented an outstanding puzzle for modern astrophysics. GRBs are the most energetic phenomena in the Universe: a fraction of a solar mass of energy ($\sim 10^{53}$ ergs) is released over a time scale of the order 1 second into photons with a very hard spectrum. Their distribution looks uniform over the whole sky and their frequency is extremely high: about 1 per day.

The most recent theoretical models place the origin of GRB at cosmological distances (*fireball models*) [34] or in the galactic halo [35]. In the first case, the burst explosion derives from merger of two neutron stars forming a binary system, while in the case of a galactic halo location it should involve small explosions on a neutron star surface.

EGRET observed emission from a handful of GRBs, setting several constrains on the source size and the energy of the photons that can escape the source. Especially in cosmological models, γ-rays photons can escape from an intense source only if the source is boosting towards us, like in the AGN jets. The X-rays, radio and optical counterparts together with the afterglows detected in the last few year seem to favor the fireball model and a cosmological origin of GRBs.

No detection of GRBs at energies above TeV has been reported up to now by the current ground-based experiment [36].

1.4 The γ-ray horizon

A source of VHE γ-rays can be detected just up to a certain distance due to the inter-galactic absorption by pair production over background radiation: $\gamma\gamma \to e^+e^-$. The target photons span from the microwave background radiation to the diffuse infrared/optical emission by galaxies. The energy threshold of the reaction is such that the energy of the center of mass must double the rest mass of the electron: $E_{\gamma-inc}\ \epsilon(1-\cos\theta) = 2(m_e c^2)^2 \simeq 10^{12}(\text{eV})^2$, where ϵ is the soft (background) photon energy, $E_{\gamma-inc}$ is the incident photon energy and θ is the incidence angle. Thus, TeV (10^{12} eV) and PeV (10^{15} eV) γ-rays will be absorbed by optical/infrared photons (~ 1 eV) and the microwave background radiation (10^{-4}(eV)), respectively.

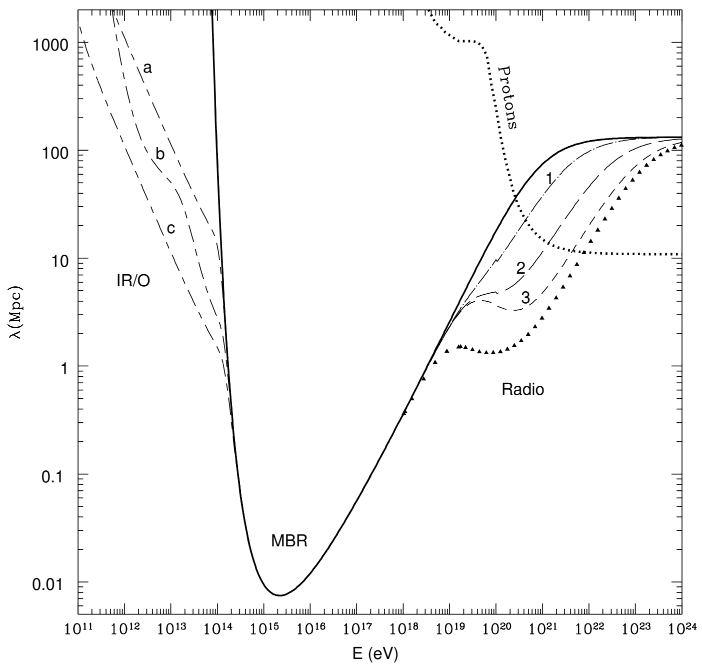

Figure 1.7: *Mean free path λ in Mpc for γ-rays of energy E (from [37]). The three curves (a,b,c) correspond to three different DEBRA models.*

The infrared diffuse extra-galactic background radiation (DEBRA) is the main responsible for TeV γ-rays absorption ($E_{\gamma-inc} > 10^{11}$ eV). This field of radiation is not well measured: nevertheless, its density increases with the wavelength and, consequently, the optical depth for VHE γ-rays increases quickly with increasing energies (see Fig. 1.7). Thus only nearby galaxies can be observed at these energies, while for distances greater than 1 Gpc (z=0.3) the galaxies will be completely obscured or their spectra heavily distorted.

The most distant AGN detected up to now at TeV range is H1426+528 with z=0.129. Its spectrum shows a heavy distortion due to the inter-galactic pair production. The level of absorption seems to be in agreement with the current DEBRA models [38].

Chapter 2

From the top of the atmosphere to the ground.

2.1 VHE γ-rays, Cosmic Rays and Extensive Air Showers

The VHE γ-rays produced in the extreme energetic astrophysical processes shown in the previous chapter, can be detected mainly by means of large detectors placed on the ground. The atmosphere is opaque to these VHE γ-rays . However, it can be used as target and calorimeter. When a γ-ray with $E > 1$ GeV enter the atmosphere, it produces a pair of ultra-high energy electrons e^+e^-, each of which in turn generates high energy photons by bremsstrahlung, each of which generates another pair e^+e^- and so on .. (see [39]). A shower of electromagnetic particles is then developed, which traveled downward and can be detected by means of ground-based detectors. The pair creation process has to occur always in the presence of an atmospheric nucleus, for the conservation of the momentum or the energy.

The mean length traveled by a photon or a pairs before interacting is called radiation (or collision) length, which in the ultra-relativistic limit is equal to the bremsstrahlung radiation length. After several radiation lengths, the shower reaches the maximum number of particles, which depends upon the initial energy of the primary, E_0, and the critical energy E_c when the energy losses for ionization become

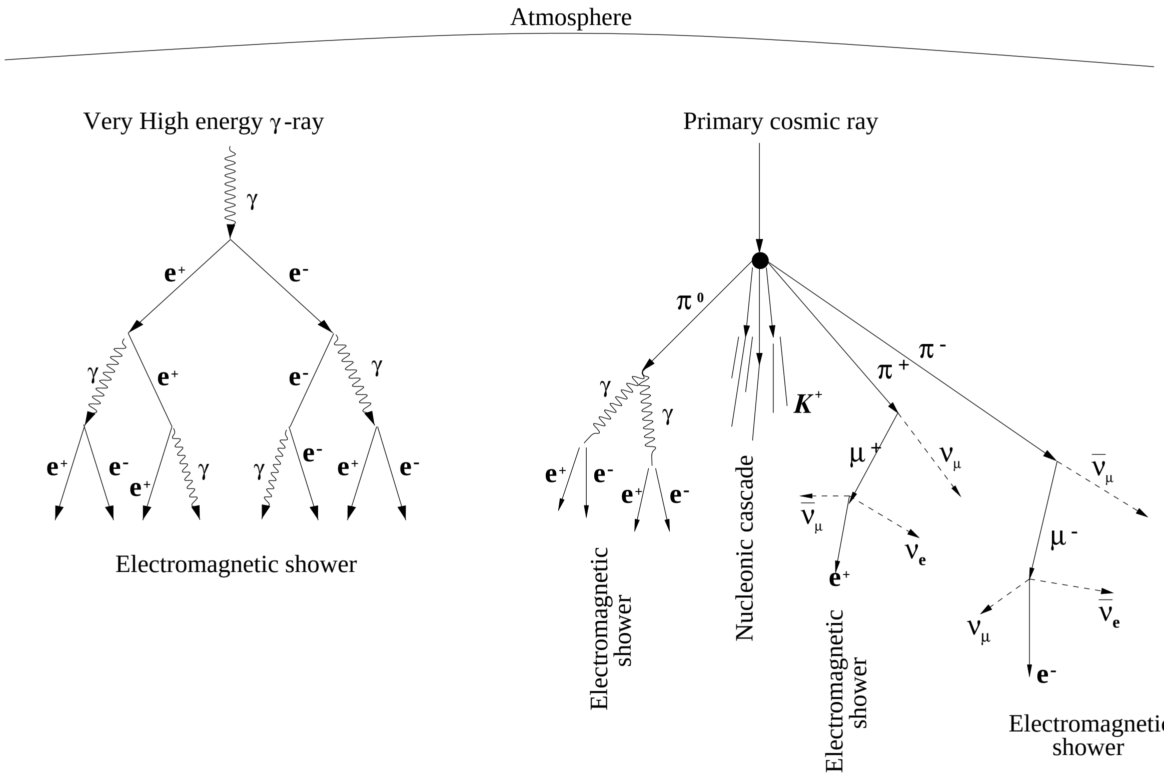

Figure 2.1: *Sketch of the electromagnetic and hadronic particles cascade induced by a VHE γ-ray and a primary cosmic ray.*

predominant and the pair production breaks. The number of particle at the shower maximum is around E_0/E_c and the maximum development is reached after a radiation length

$$X_{MAX} = \lambda \frac{\ln\left(E_0/E_c\right)}{\ln 2} \ .$$

Unfortunately, not only the VHE γ-rays we want to detect give raise to particle showers when entering the atmosphere. Also the *cosmic rays*, electrons, protons and heavier nuclei which continuously bombard the Earth and are uniformly distributed in space, when entering in the Earth atmosphere interact with a nucleus of the air and start a series of reactions which yield to the production of a cascade of secondary particles, usually charged and neutral pions, kaons, etc., which travel downward and produce other particles until the energy losses for ionization and bremsstrahlung are

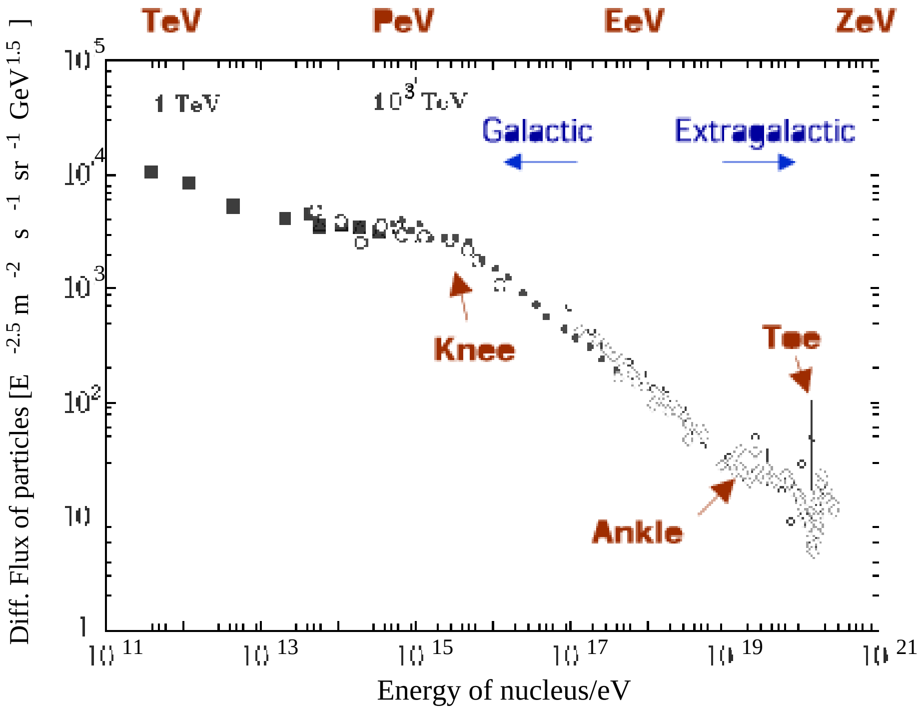

Figure 2.2: *The differential energy spectrum of the cosmic rays.*

bigger than the critical energies needed to produce other particles. The pions decay almost immediately in neutrinos and muons that reach the ground without any further interaction.

The evolution of the cascade, both for a primary γ-ray and hadron, is illustrated by the simple branching model in Fig. 2.1.

This simple toy model can be applied both to the high energy γ-ray induced showers and, in first approximation, to the hadronic showers. The γ-ray induced shower is composed by only electromagnetic particles which, as we will show later, can permit to distinguish them from the hadronic induced cascades. Another key feature of the hadronic showers is the large amount of muons generated, which come from the decays of the charged pions, and which is a factor of about 30 greater with respect to the γ showers.

The cosmic rays (CR) form an enormous background we have to deal with in the VHE γ-rays astronomy. The ratio between γ-rays and protons at the top of the atmosphere is of about 1/1000. CR with $E < 10^{15}$ eV, given their large flux, can be studied directly with instruments provided with a small acceptance (a few $m^2 \cdot sr$) by means of balloons or satellites outside the atmosphere, while for energy $E > 10^{15}$ eV the flux is so low that we have to use indirect measurements using extended arrays placed on the Earth surface. Figure 2.2 shows the measured CR differential energy spectrum, which spans up to 10 order of magnitude in energy.

2.2 The Čerenkov Effect

If the secondary particles produced in the cascade travel in the medium (in this case, the atmosphere) with a speed v great than the speed of light in the same medium, electromagnetic radiation will be emitted by Čerenkov effect. The ground-based γ-ray astronomy is just based on the detection of the Čerenkov light emitted by the passage through the atmosphere of the ultra-relativistic electron-positron pairs created by a VHE γ-ray entering in the atmosphere.

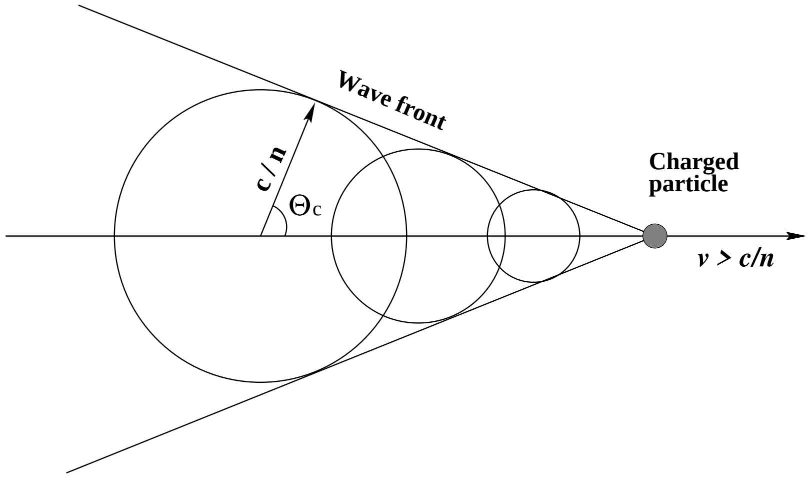

Figure 2.3: *Huygens' construction of the front wave emitted by the passage of a charged particle with speed $v > c/n$ moving through a medium of refraction index n.*

The condition to be fulfilled for a charged particle in order to trigger the Čerenkov radiation emission process is such that its speed v must be higher than the light speed in the medium:

$$v \equiv \beta c \geq c_{med} \equiv c/n$$

where $c_{med} = c/n$ is the light speed in the medium (see Fig. 2.3). Thus, the threshold for the Čerenkov effect can be written as:

$$\beta \geq \frac{1}{n} \tag{2.1}$$

The Čerenkov effect is eventually produced when the surrounded medium reacts to the passage of the charged particle, and it is totally uncorrelated with the bremsstrahlung emission, which is due to the direct interaction between the moving particle (electron or positron) and the atoms of the medium [40]. Figure 2.4 shows the behaviour of a charged particle moving, respectively, with low and relativistic speed through a dielectric medium. When $v \ll c_{med}$ the particle polarizes the medium (see Fig 2.4 (a)) and dipoles are formed along the track. After the charge has passed by, the dipole returns to the equilibrium state emitting an electromagnetic pulse. However, due to the symmetry of the polarization field around the slow moving particle,

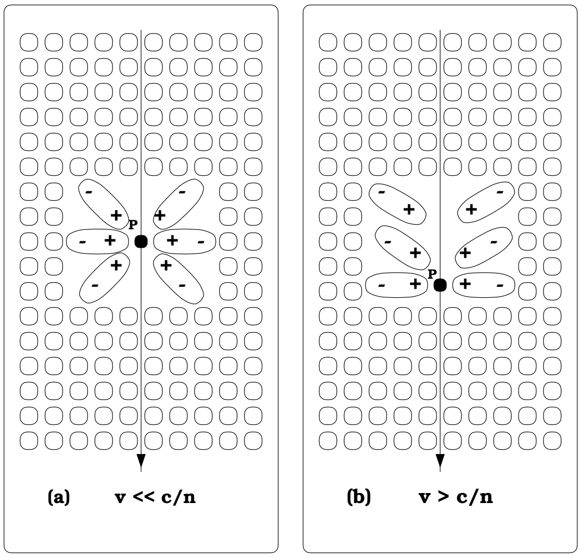

Figure 2.4: *A charged particle moving in a dielectric medium for two different cases: (a)* $v \ll c_{med}$*; (b)* $v \gtrsim c_{med}$.

the resultant field at large distances will appear as null. On the contrary, when the charged particle travels with a speed $v \gtrsim c_{med}$, the polarization field results to be highly asymmetric (see Fig 2.4 (b)) and the resultant dipole can be seen even at large distances from the track. Each dipole will emit an electromagnetic pulse when turning back to the equilibrium state and the waves, interfering constructively, will give raise to the Čerenkov front wave.

A basic property of the Čerenkov radiation is that the radiation is emitted in a narrow cone along the particle track with a fixed angle Θ_c which depends upon the refraction index of the medium, in a way similar to the acoustic waves emitted by a supersonic plane. In case of ultra-relativistic particles, the angle is independent from the particle energy and can be derived directly from the geometry of the wave emission:

$$\cos\Theta_c \ = \ \frac{c/n}{\beta c} \ = \ \frac{1}{\beta n} \tag{2.2}$$

Another important feature is that the intensity of the emitted radiation depends on the refraction index. The refraction index in the atmosphere varies with the height and the correspondent threshold energy and intensity emission change as well. The energy threshold for Čerenkov emission decreases as the shower develops further in the atmosphere and correspondingly the intensity emission increases. So, the intensity of Čerenkov emission depends upon the development of the electron-photon cascade through the atmosphere.

The features mentioned above are fundamental to work out the properties of the γ-rays which can be detected thanks to the Čerenkov light emission in the atmosphere.

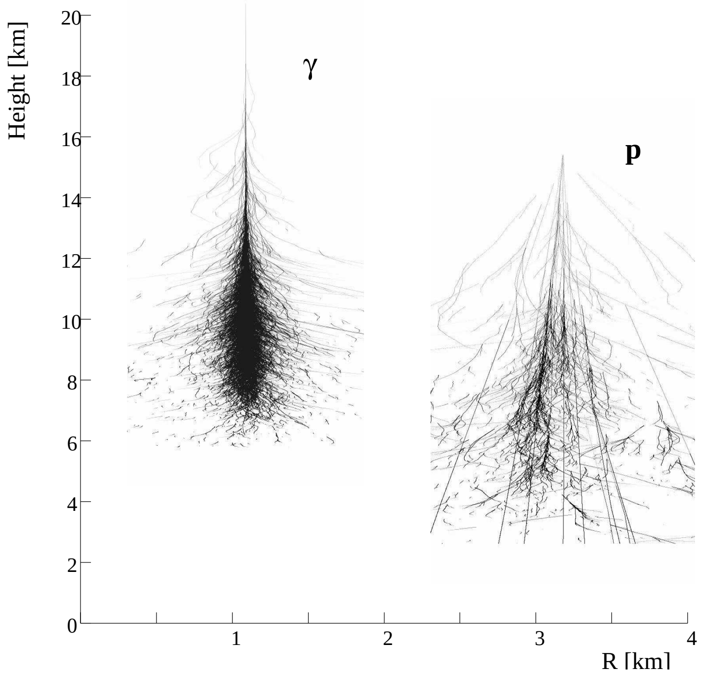

Figure 2.5: *MC simulation of 1 TeV γ-ray- and proton-induced shower.*

2.3 EAS and the ground-based γ-ray astronomy

Let us see now the main characteristics of the EAS showers and the Čerenkov radiation emitted, which are directed related with the detection of VHE γ-rays by ground-based experiments. Usually, proton/hadron-induced showers develop much further in the atmosphere than γ-ray showers, due to the different interaction length: $\sim$ 80 g cm^{-2} for a primary proton and $\sim$ 30 g cm^{-2} for a primary γ-ray. Besides, due to the presence of pions with high transverse momentum, the proton-induced cascade shows a larger lateral development than that one exhibited by γ-rays showers. Figure 2.5 shows a MC simulation of a proton and γ-ray shower development made by means of the ALTAI simulation code [41]. It is clearly visible the more compact nature of the γ-ray shower and the larger transverse amplitude of the proton shower. Since the hadronic showers develop further in the atmosphere, the bulk of Čerenkov radiation is emitted closer to the ground and this corresponds to a much intense Čerenkov photons wave front (*the light pool*) but also a less uniform photon distribution with respect to the γ showers.

For gamma rays of energies between 100 GeV and 10 TeV the maximum of the shower development occurs at a height between 10 and 7 Km above sea level. The median altitude for Čerenkov emission from a 1 TeV γ shower is 8 Km (see Fig. 2.6). Half of the emission occurs within 20 m. of the shower axis (70 m. for a proton shower [42]). The Čerenkov photons are emitted by the pairs e^+e^- within a narrow cone of $1° - 2°$, mostly in the optical wavelength band and in very narrow flash pulses, which can last between 5 and 30 ns. The Čerenkov wave front is very thin with an average angular extent on the sky of about 0.5°. The cone of the emission is smeared a bit by the fact that electrons and positrons in the shower suffer Coulomb scattering and therefore the emitting particles do not emit all along the same axis. That makes the light pool to be spread over an area of up to about 100 m. from the shower axis at the ground level. For a primary 1 TeV γ-ray, the radial density distribution of the Čerenkov photons is almost flat up to 120 m. (at 2 Km a.s.l.) from the impact point of the shower axis on the ground (the *core* of the shower) (see Fig. 2.7), with an average photon density of about 200 photon/m^2 in the visible.

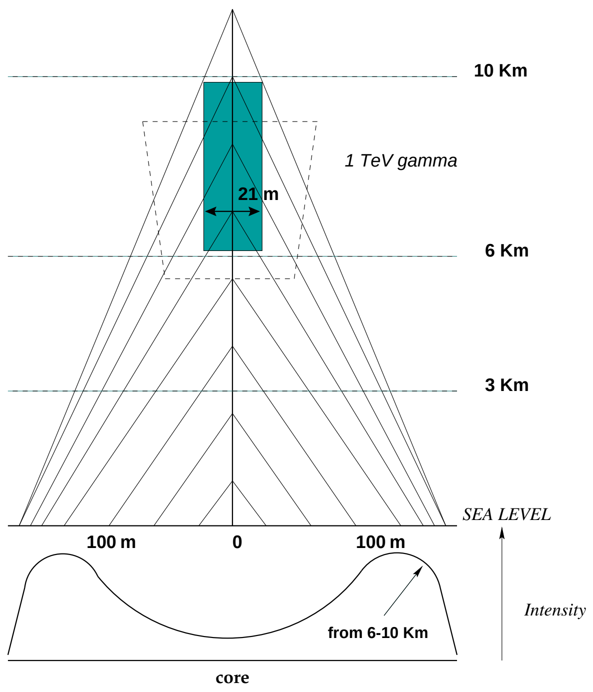

Figure 2.6: *Longitudinal development of a γ-ray-induced shower and the spatial correlation with the Čerenkov radiation emitted.*

The total distance traveled by all particles above the Čerenkov threshold and the photon density are directly related to the energy of the primary particle. Thus, the Čerenkov light yield gives a direct measurement of the initial γ-ray energy. Figure 2.8 shows the photon distribution on the ground for a γ-ray-induced air shower and a proton one, calculated by means of a MC simulation made using the CORSIKA code [43]. The differences in the two type of showers are clearly visible. The Čerenkov rings in the proton shower are caused by muons traveling perpendicularly to the

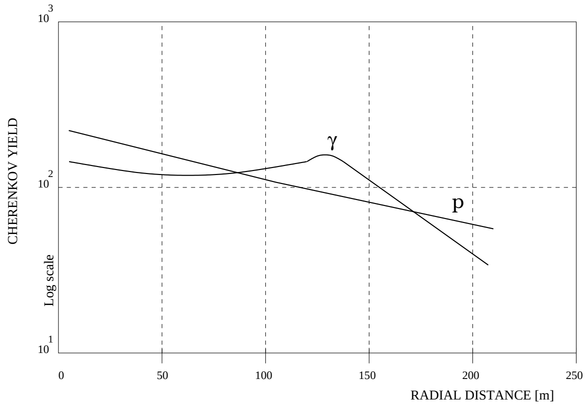

Figure 2.7: *The lateral distribution of the Čerenkov light yield for typical γ-ray and hadron showers. Note the so-called "hump" in the photon distribution at $\sim$ 120 m. from the shower axis.*

ground.

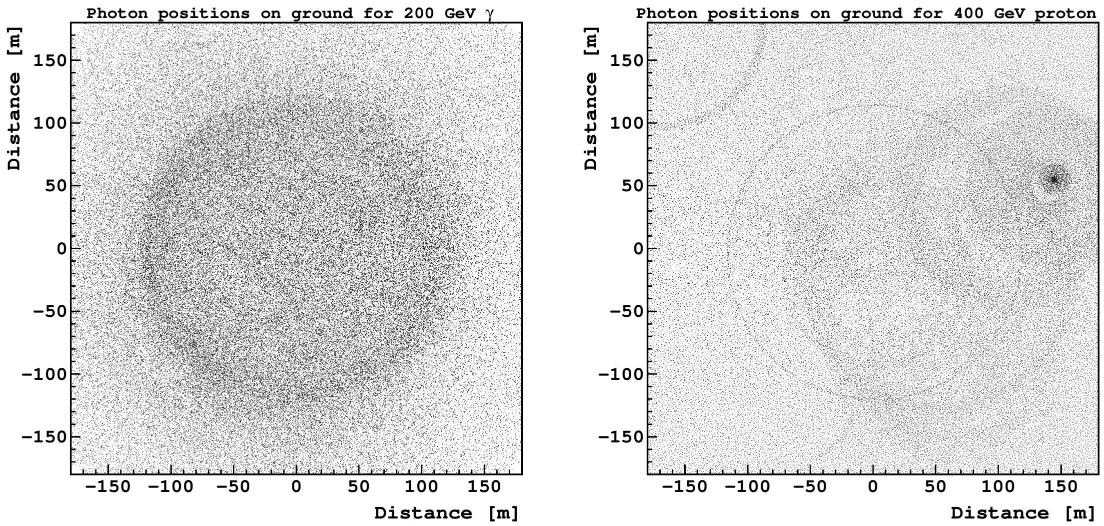

Figure 2.8: *Distributions of the photon density on the ground for vertically incident γ-ray-induced air shower (left panel) and proton-induced shower (right panel). The observation depth is 793 g cm^{-2}.*

In the next chapter it is shown how it is possible to detect VHE γ-rays by means of Čerenkov light collectors placed on the ground.

Chapter 3

The detection of VHE γ-rays with Čerenkov telescopes: the Imaging Atmospheric technique

3.1 The Čerenkov telescopes

We have seen in the previous chapter that Čerenkov radiation is emitted when the secondary particles produced in the interaction of the primary γ and cosmic rays with the atmospheric nucleons, move downward with speed greater than the light speed in the medium. The Čerenkov photons, traveling towards the ground, can be gathered by means of light collectors which focus them onto a camera formed by an array of small photo-multipliers (PMTs), generally with fractions of inches in diameter. Such a detector is known as an *imaging air Čerenkov (IAC) telescope* (for a review see [44] [45]). Since these detectors point to the VHE γ-ray source, the name telescope is perfectly suitable. Figure 3.1 shows one of the HEGRA Čerenkov telescopes.

The light collector (or reflector) is usually composed by a segmented mirror, having a parabolic or spherical shape. The mirrors do not require as a high precision as in large optical telescopes due to the fact that the angular structure of the Čerenkov light is relatively broad (~ 3 arcmin).

The PMTs camera (see Fig. 3.2) is the most important part of a Čerenkov telescope and permits to record an "image" of the shower which traces its lateral

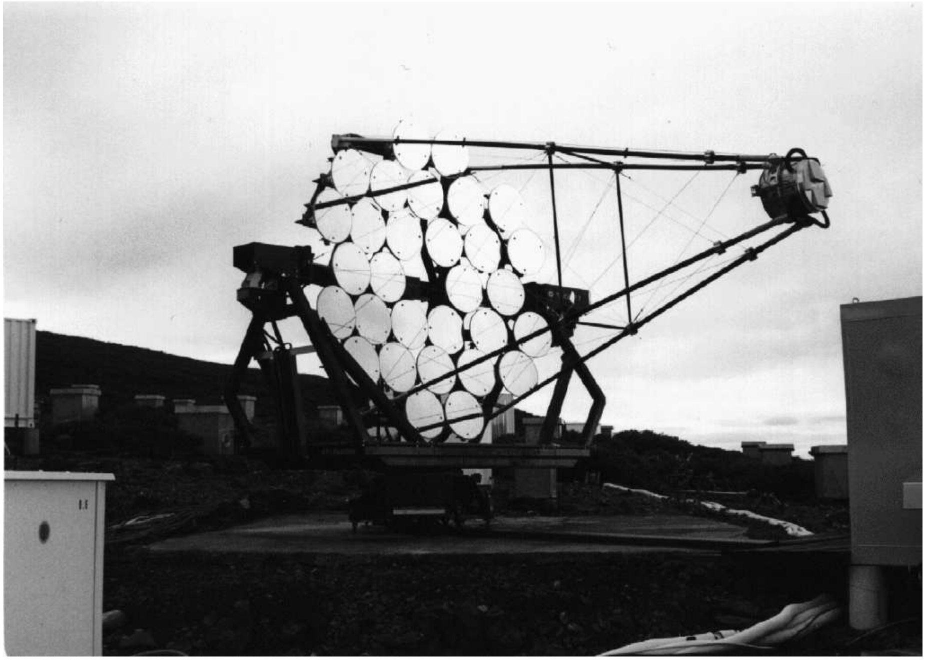

Figure 3.1: *A Čerenkov telescope.*

and longitudinal development. Due to the short duration of the Čerenkov flashes (typically between 5 and 30 ns), a fast read-out electronics is needed in order to detect, amplify and digitalize the signals, which rules out the possibility to use common astronomical instruments like CCD cameras, with typical integration time of the order of milli-seconds. Up to now, the PMTs have been the most appropriate detectors to sample the Čerenkov flashes, because of their low costs, high sensitivity to the UV/Blue wavelength band (200-600 nm) and rapidity.

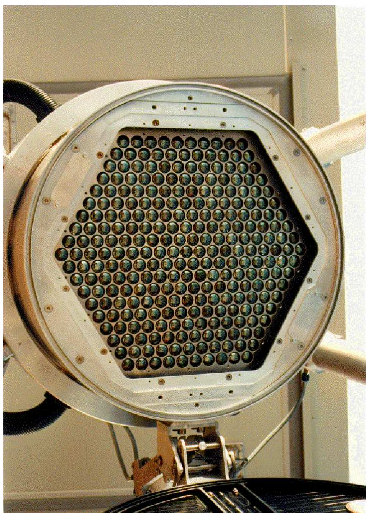

Figure 3.2: *The PMTs camera.*

The PMT pulses from the triggered channels are amplified and feed a multiplicity logic ("majority") unit which permits to form a coincidence trigger between several channels. Afterwards, the signals are sampled, digitalized and stored for off-line event analysis by means of fast analog-digital converters (Flash ADCs).

A relevant source of background noise in a Čerenkov telescope is given by the night sky light background. Under typically clear sky conditions, the flux of night sky photons amounts to about 2×10^{12} ph m^{-2} s^{-1} sr^{-1} for wavelengths between 300 and 600 nm [46], a range where the camera PMTs are sensitive to. A telescope with a field of view (FoV) of about $1°$ collects up to ~ 5 ph m^{-2} which is much less than the expected value of $\sim$ 65 ph m^{-2} generated in a 1 TeV γ-ray-induced shower. In the case of the HEGRA system of IAC telescopes (IACTs), the FoV is equals to $4.3°$ and the density of night sky photons amounts to ~ 100 ph m^{-2}.

With the aim to reduce the night sky accidental background, different trigger logics can be chosen. As we will see in the next chapter, a trigger logic applied to the PMTs camera and a fast accurate timing of the arrival times of the Čerenkov pulses in different elements of the IACTs HEGRA array, permit to drastically reduce the triggers signal arising from this background source.

3.2 The Čerenkov images and the shower image parameters

The night sky background is not the only source of noise in a Čerenkov telescope. As we have seen in the previous chapter, cosmic ray induced air showers as well emit Čerenkov photons along their development, which reach the ground and are collected and registered. This represents the main source of background, as the 99% of the showers is generated by a proton or a heavier nuclei. Two information can be used to discriminate between a γ-ray and a hadronic shower, once they have been registered: the arrival direction and the shape of the image formed in the PMTs camera by the collected photons.

The Čerenkov images carry direct information about the arrival directions of the cascade. They usually have an elongated, roughly elliptical shape, with its major axis reflecting the image of the shower axis. A shower developing right along the optical axis of a Čerenkov telescope will form a circular image exactly at the camera center. Showers with the *core* displaced at some distance from the telescope and with axes parallel to the axis telescope, will form an elliptical image with

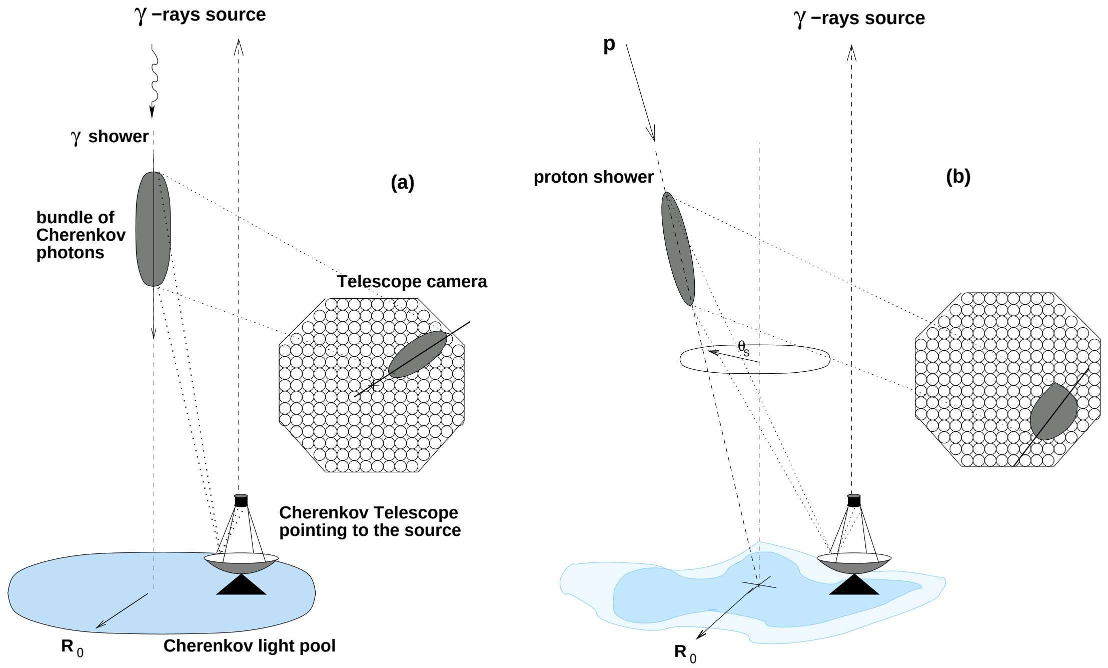

Figure 3.3: *Sketch of the formation of a Čerenkov image in the telescope camera. (a) γ-ray-induced shower; (b) cosmic ray-induced shower.*

the major axis pointing to the center of the field of view. This is what we expect from an electromagnetic shower induced by a γ-ray coming from the source the telescope is pointing to (see Fig 3.3 (a)). On the contrary, the images produced by cosmic rays-induced showers, randomly distributed in space and with arrival axes tilted with respect to the Čerenkov telescope axis, will generally form ellipses with their major axes not pointing towards the center (see Fig 3.3 (b)).

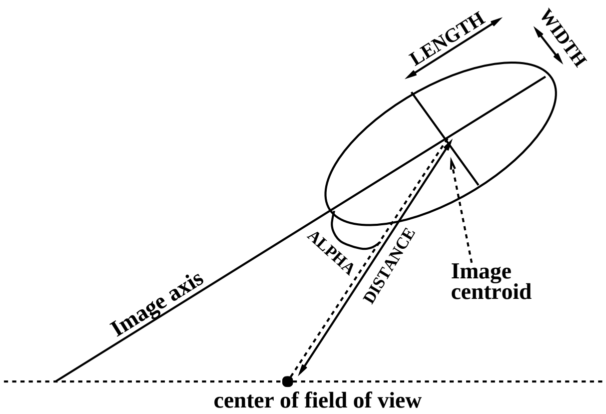

Figure 3.4: *Shower image parameters.*

Besides the arrival information, a further differentiation between γ-rays and hadronic showers based on the different images shape was introduced by Hillas [47]. This parameterization (see Fig. 3.4) is directly related to the elliptical shape of the Čerenkov images and is performed ap-

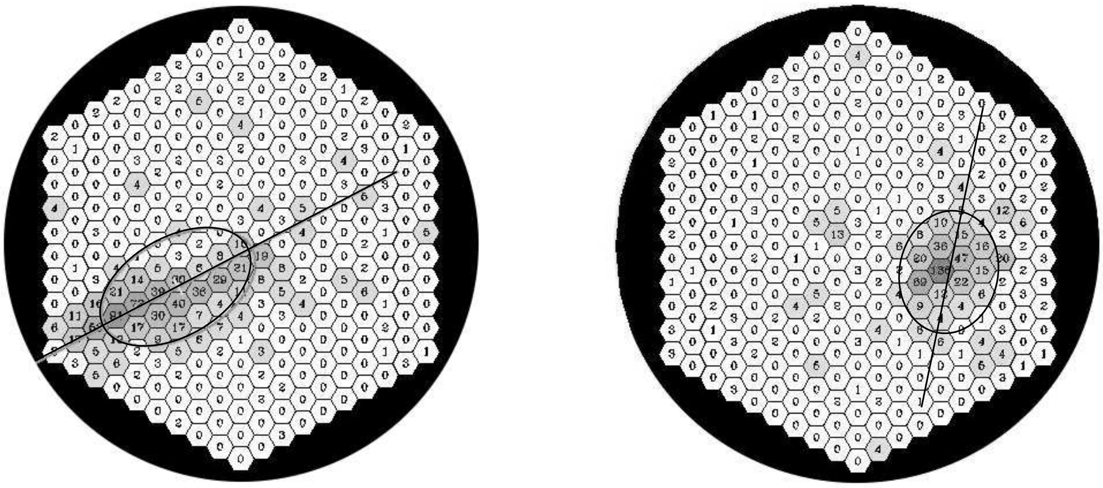

Figure 3.5: *The Čerenkov images for a γ (left) and hadron (right) candidate as recorded by the HEGRA IACTs camera. Superimposed is the image parameterization by means of the WIDTH and LENGTH parameter. The numbers represents the calibrated Flash ADC counts.*

plying a secondary moments analysis to the two-dimensional angular distribution of the image, making use of the position of the PMTs "fired" by the Čerenkov photons and the resulting ADC counts (see App. A for a detailed description of the mathematical procedure).

Figure 3.5 shows two Čerenkov images produced by a γ candidate (*left panel*) and a hadron candidate (*right panel*), respectively, as recorded by one of the HEGRA IACTs PMTs camera. Due to the discrete size of the pixels, what one actually has is a pixellated image, with a weight for each pixel depending on the number of photons recorded by that pixel. It is important for the size of the pixels to be sufficiently small in order to measure with a certain degree of precision the dispersion of the light along the semi-axis of the ellipse (at least half of the average value of the parameter we want to measure).

Table 3.1 reports the definition and the physical meaning of the main parameters while Figure 3.6 shows the distributions of the image parameters WIDTH and LENGTH for MC simulated γ-rays and real CR detected with the HEGRA IACTs array.

Table 3.1: *Definition and physical meaning of the main shower image parameters [42]*

WIDTH	The rms spread of light along the minor axis of the image. It gives a measure of the lateral development of the shower.
LENGTH	The rms spread of light along the major axis of the image. It represents the longitudinal development of the shower.
DISTANCE	The distance of the image center of gravity (cog) from the center of FoV.
ALPHA	The angle between the major axis of the image and the line connecting the image cog and the center of FoV.
SIZE	The total integrated light content of the shower≡total number of ph.e. contained in the image.

As we mentioned before, the differences in development between the electromagnetic and the hadronic showers clearly appear after the parameterization of the Čerenkov images. The first ones are much more localized and give more compact images while the big fluctuations in the hadronic showers are imaged in broader WIDTH and LENGTH distributions.

The ALPHA parameter, together with the WIDTH, is the most important in terms of γ/hadron separation in a single IAC telescope and provides with the angular information about the shower arrival direction. This angle is somehow related with the angle between the shower axis and the telescope axis. The axes of the γ-ray showers point to the γ-rays source and the major axes of the correspondent Čerenkov images are directed to the center of FoV. Hence, for γ-rays the ALPHA parameter must be distributed around zero, while it will show an uniform distribution for the random pointing hadronic showers. These differences permit to apply a very effective background discrimination.

As we will show in the next chapter, the system of IACTs HEGRA fully exploits the γ/hadron rejection based both on the arrival direction and the image shape differentiation of the atmospheric showers.

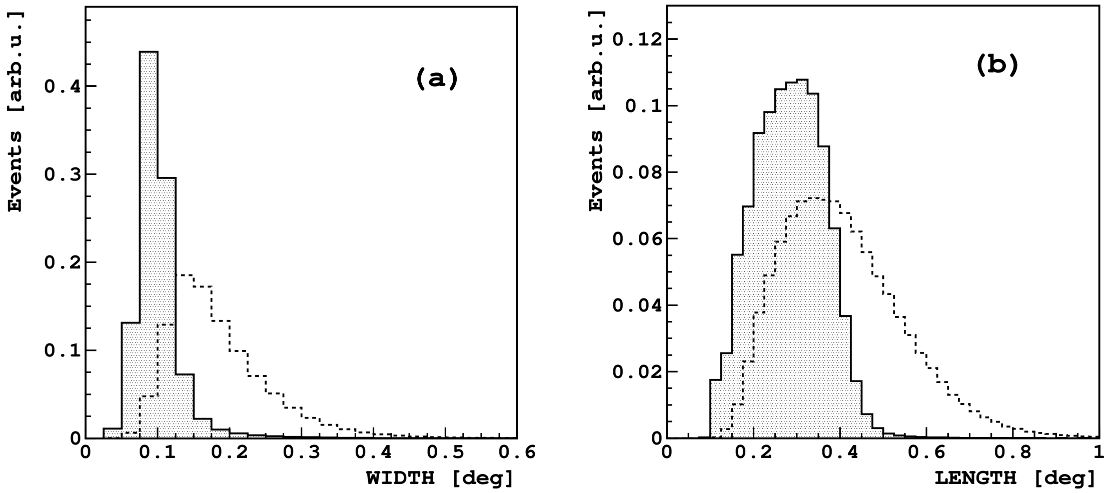

Figure 3.6: *Distributions of the image parameters WIDTH (a) and LENGTH (b) for MC simulated γ-rays (filled histograms) and real cosmic rays (dashed histograms) detected with the HEGRA IACTs array. Range of zenith angles: between 0° and 45°. MC simulations performed by means of the ALTAI simulation code [41].*

3.3 The energy threshold of a Čerenkov telescope

The minimum γ-ray photon energy detectable by a Čerenkov telescope can be assumed as the energy threshold E_{th} of the instrument[1]. Since the Čerenkov photon density emitted by the secondary particles in the shower is, in first approximation, proportional to the energy E of the primary, it is clear that the threshold depends on how much Čerenkov light is possible to collect, and transform in an electrical signal, with the reflector.

If we define S as the Čerenkov light signal contribution, we get that:

$$S = \rho_\gamma A \; \epsilon \propto E \; A \; \epsilon$$

where ρ_γ is the Čerenkov photon density, A is the collection area of the mirror and ϵ is the PMT quantum efficiency (q.e.) (usually with values between 10% and 20%).

The Čerenkov photons have to be detected upon the night sky background noise N (Poisson fluctuation dominated):

$$N \propto \sqrt{\phi \; \Omega \; A \; \epsilon \; \tau}$$

[1]Later on, we will use an alternative definition of energy threshold (see § 4.7).

where ϕ is the night sky background photon flux, Ω is the solid angle subtended by a PMT and τ is the electronic integration time. Thus, the shower energy which gives the minimum signal-to-noise ratio S/N able to trigger the telescope, can be taken as the energy threshold of the detector:

$$E_{th} \propto \frac{\phi\ \Omega\ \tau}{\sqrt{A\ \epsilon}} \tag{3.1}$$

The Čerenkov telescopes operating at present show an energy threshold of a few hundreds of GeV. Eq. 3.1 shows that if we want to lower the energy threshold, we have to increase the mirror area and/or the q.e. of the sensors. The future instruments under construction (MAGIC [49], HESS [48], VERITAS [50] etc.) tend to have as much reflector surface as possible in order to lower the instrument threshold up to tenths of GeV. Moreover, high q.e. detectors are under development, which hopefully will permit to reach values of q.e. as high as up to 80%.

An alternative method to lower the energy threshold of the instrument without changing its hardware has been implemented by the author and colleagues of the HEGRA collaboration with the HEGRA system of Čerenkov telescopes (see [52]) and it will be explained in details in § 5.

3.4 The effective area of a Čerenkov telescope

When the telescope is within the Čerenkov light pool and the Čerenkov photons density is high enough to trigger the telescope, the air shower will be detected (see Fig 3.3 as example). One of the main characteristics of a Čerenkov telescope is the ability to detect a shower even at large impact distances[2]. This means that its detection area, the *effective (or collection) area* of the telescope, is much larger than its intrinsic volume given by the mirror area. That is a great advantage with respect to satellite detectors, with present area of just a few squared centimeters against values of effective areas for the ground-based γ-rays detector as high as 10^9 cm^2.

The effective area A_γ depends upon the energy of the shower and its impact point [53]:

$$A_\gamma(E) = 2\pi \int_0^\infty P_\gamma(E,r)\ r dr$$

[2] The impact distance is defined as the distance of the telescope to the core shower position.

where $P_\gamma(E, r)$ is the probability for a shower to be triggered. This probability depends on the geometrical area of the reflector and the q.e. of the camera PMTs.

In general, as we shall see in the next chapter (§ 4.7), the effective area for a Čerenkov telescopes increases with the shower energy and for higher zenith angles of observation .

Chapter 4

The HEGRA Stereoscopic System of Imaging Air Čerenkov Telescopes

4.1 The stereoscopic technique

The stereoscopic observations of extended air showers have proven to be very effective in the investigation of galactic and extra-galactic VHE γ-ray sources. The idea is to observe the atmospheric showers from different viewing angles, in a *stereoscopic mode*, using more than one IAC telescope [54] [55].

Stereoscopic observations offer the following advantages with respect to single IAC telescope observations:

- high precision in the reconstruction of the shower arrival direction of individual air showers and improved angular resolution;
- improved γ/hadron separation;
- lower trigger thresholds;
- improved energy resolution.

The observations of γ-ray showers with a single telescope do not allow a complete geometrical reconstruction of the shower axis in space, because only one projection of the shower is available for each event. However, using advanced methods based on the strong correlation between the shape of the Čerenkov light images and their angular distances to the source position, one can achieve for a single IAC telescope an angular resolution for individual γ-ray showers of about 0.12° [56, 57, 58] using a fine pixellation camera.

A full reconstruction becomes possible in observations with two or more telescopes offering simultaneously a number of views of an individual shower. The simultaneous observation of a single air shower by at least two telescopes allows to measure the arrival direction with a typical accuracy $\leq 0.1°$ and to localize the core shower position within 10 to 15 m. This, as we see later on, permits to drastically suppress the CR background for observations of point-like sources. Figure 4.1 offers a sketch of a stereoscopic view of a γ-ray-induced air shower.

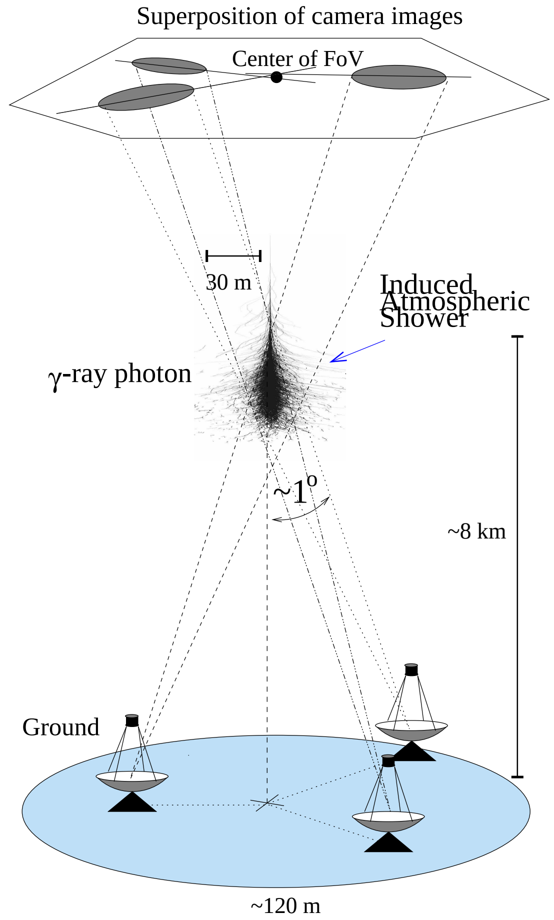

Figure 4.1: *Stereo view of a γ-induced air shower.*

The HEGRA collaboration has been the first one to apply the stereoscopic technique to the observation of VHE γ-rays by means of ground-based detectors [59]. The observations of the Crab nebula, the standard candle in γ-ray astronomy, at energies above 500 GeV at $> 5\sigma$ level in 1 hour of observation [60], the continuously monitoring of Mkn 501 [61] and Mkn 421 [62], the detection of two other AGNs, H1426+428 [38] and 1ES1959 [63], the SNR Cassiopeia A [18] and the unidentified TeV source close to the Cygnus OB2 association [33], represent very relevant results which confirm the theoretical expectations foreseen for the stereoscopic imaging technique. In what follows, we will talk in more detail of the technical aspects of the instrument.

4.2 The HEGRA System of IACTs

The HEGRA IACTs system is located on the Canary Island La Palma, at the "Observatorio del Roque de Los Muchachos" of the "Instituto Astrofísico de Canarias", at a height of about 2200 m. a.s.l. (28.8° N, 17.9° W).

The telescope array, primarily designed for stereoscopic observation of γ-radiation at energies above several hundred GeV [64], is formed by five identical IACTs, one at the center and four others at the corners of a 100 m. by 100 m. square area (fig. 4.2). The multi-mirror reflector of each telescope has an area of 8.5 m^2 and is formed by thirty 60 cm diameter front aluminized and quartz coated spherical mirrors, independently installed on an almost spherical frame supported by an alt-azimuth mount. The FWHM of the point spread function (PSF) of the reflector is better than 10 arcminutes. Each telescope is equipped with a 271 PMTs camera with a pixel size of 0.25°, which results in a telescope effective field of view of $\simeq$ 4.3° [65]. The digitization of the PMT pulses is performed with a 120 MHz Flash-ADC system.

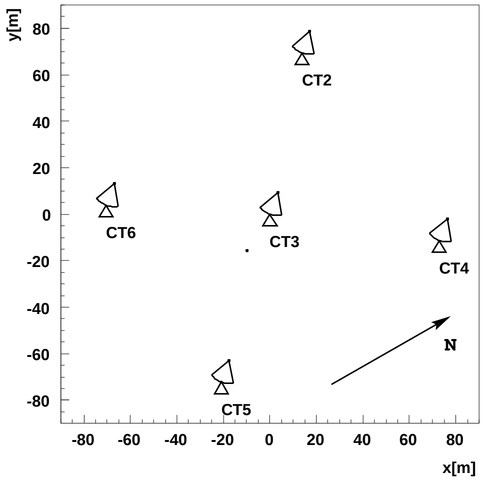

Figure 4.2: *The layout of the HEGRA system of IACTs (labeled from 2 to 6) at the Observatorio del Roque de Los Muchachos.*

4.3 The trigger logic of the HEGRA IACTs

Requiring multiple trigger coincidences between more than one telescope permits to drastically reduce the number of random coincidences due to the night sky background and the rate of triggers due to local muons. Thus, it is possible to operate the single IAC of the array with a reduced PMT trigger threshold, hence, with reduced energy thresholds (§ 3.3).

The HEGRA system of IACTs operates a two level trigger which is effective in reducing the background due to the night sky noise and to operate a selection of γ-rays already at trigger level [66]. The first level of trigger is *local* and requires for each camera of each telescope in the system to have at least 2 next-neighbour pixels over 271 (*2NN/271*) with a signal above the PMT trigger threshold q_0 (measured in ph.e). With this trigger logic, accidental background triggers caused by the light of the night sky are already reduced by a factor of about 48, while over the 95% of the compact γ-like images are kept. The improved suppression of accidental triggers allows to operate with a reduced pixel trigger threshold and therefore with a lower energy threshold. Presently, the HEGRA system of IACTs operate with a pixel trigger threshold q_0 =8 ph.e.

The second level of trigger is *global* and asks for at least 2 telescopes of the system to be triggered by an event within a given coincidence time. Due to the large separation between the telescopes (from 70 up to 140 m.), the arrival times of the Čerenkov light front at each individual telescopes can differ up to 400 ns for showers inclined at 60° from the zenith, therefore delays have to be introduced in order to allow a short temporal window for the inter-telescope coincidences. The width of the inter-telescope coincidence is set to 70 ns. Detailed comparisons of the actual hardware event rate with the simulations for different trigger configurations and thresholds q_0 are given in [67].

The multi-telescope coincidence basically suppresses the background due to the high number of muons produced in the cosmic rays induced showers, which can locally trigger at most one single IAC of the system and are rejected applying the *global* trigger.

4.4 CR detection rates

The detection rate of the HEGRA IACTs system is mainly determined by the isotropic flux of CR and depends directly from the assumed local trigger condition at each telescope and from the triggered telescope multiplicities.

The cosmic ray detection rate is given by:

Table 4.1: *CR rates measured by the HEGRA IACTs system for different triggered telescopes multiplicities and for a local trigger threshold* q_0 =*8 ph.e.*

$n_{tel} \geq 2/5$	$n_{tel} \geq 3/5$	$n_{tel} \geq 4/5$	$n_{tel} \geq 5/5$
17.6	10.4	4.7	3.5

$$R_{CR} = 2\pi \int_0^{\Omega_0} d\Omega \int_0^{R_0} RdR \int_0^{E_0} \frac{dJ_{CR}}{dEd\Omega dS}\ P_{CR}(R,E,\theta)dE\ ,$$

where E is the primary energy of a CR, R is the distance to the shower core, θ is the angle which the shower axis forms with respect to the telescope axis and $P_{CR}(R,E,\theta)$ is the probability of the shower to trigger the system. Ω is the solid angle subtended by the PMTs camera and S is the system effective area.

The higher is the shower energy, the higher is the probability to fulfill the trigger system conditions (both locally and globally, with at least 2 out of 5 telescopes triggered), even though they have very large impact distances. However, due to the very steep CR energy spectrum, $dJ_{CR}/dE \propto E^{-2.75}$, the contribution to the detection rate of CR showers with energies $E > 20$ TeV is very small.

Table 4.4 shows the measured CR rates from the HEGRA IACTs system, for different trigger multiplicities and for a local trigger threshold q_0 =8 ph.e.

4.5 Reconstruction of shower parameters.

4.5.1 Localization of the shower core.

The position of the shower at the observation level can be measured for each single event which has triggered at least two telescopes of the system, using purely geometrical reconstruction which does not relate on the image shape. The reconstruction algorithm make use of the orientation of the Čerenkov light images of each triggered telescopes. Thus, the core location is obtained by intersecting the image major axes emerging from the telescope locations, assuming that all telescopes dishes are in a

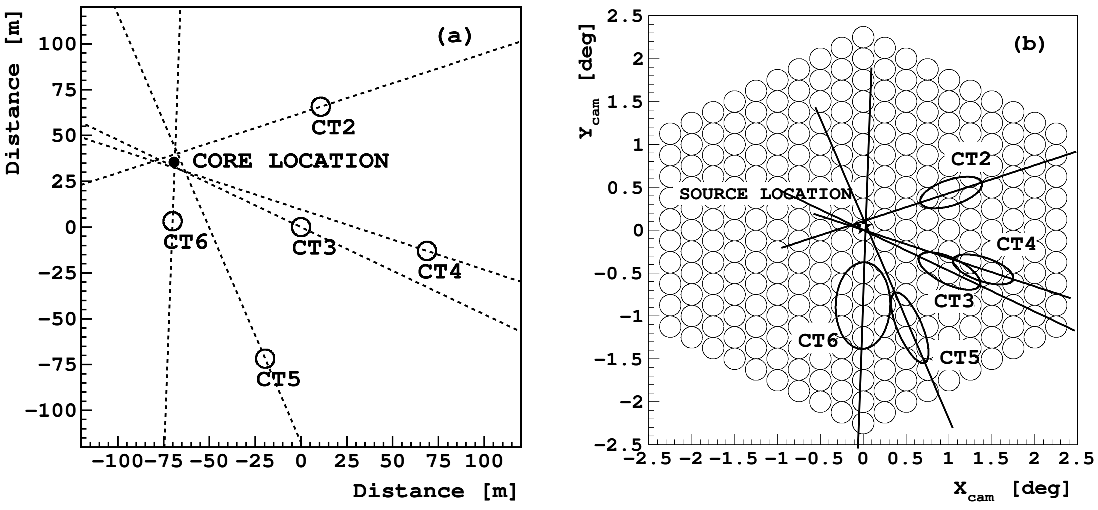

Figure 4.3: *Reconstruction of the core shower location on the ground (a) and the shower arrival direction in camera coordinates (b) for a MC simulated γ-induced vertical air shower (E_γ = 10 TeV.). The dimensions of the ellipses (WIDTH = minor axis; LENGTH = major axis) are based on the Hillas parameterization of the Čerenkov images.*

common plane (Fig. 4.3 (a)). Once the core location is known, the impact distances to each telescope can be calculated, which, as we will see further on, will be used for the γ/hadron separation. The accuracy in the core shower position is limited by the determination of the image orientation: usually, that gets worse as the zenith angle of the observed object increases. Nevertheless, observing a γ-rays source at zenith angle below 45° and restricting the impact distances from each telescope of the system to the shower core within 200 m., the average accuracy is less than 20 m., which is quite sufficient because the shape of the Čerenkov light images does not significantly change within this distance.

4.5.2 Reconstruction of the shower arrival direction.

The simultaneous observation of air showers with two or more Čerenkov telescopes, offers the possibility to reconstruct with high accuracy the orientation of the shower axis with respect to the telescope axis [55]. Each single image is superimposed on a common focal plane and the shower arrival direction is determined by the intersection of the major axes of the ellipsoid-like images (Fig. 4.3 (b)). If the telescopes are directed towards the γ-rays emitter, the reconstructed shower arrival directions for γ-ray-induced air showers have to point at the position of the γ-rays source. Figure 4.4 shows the reconstructed arrival directions, converted in celestial coordinates, of the recorded events taken pointing the HEGRA IACTs array to the direction of the Crab Nebula, the standard candle in γ-ray astronomy.

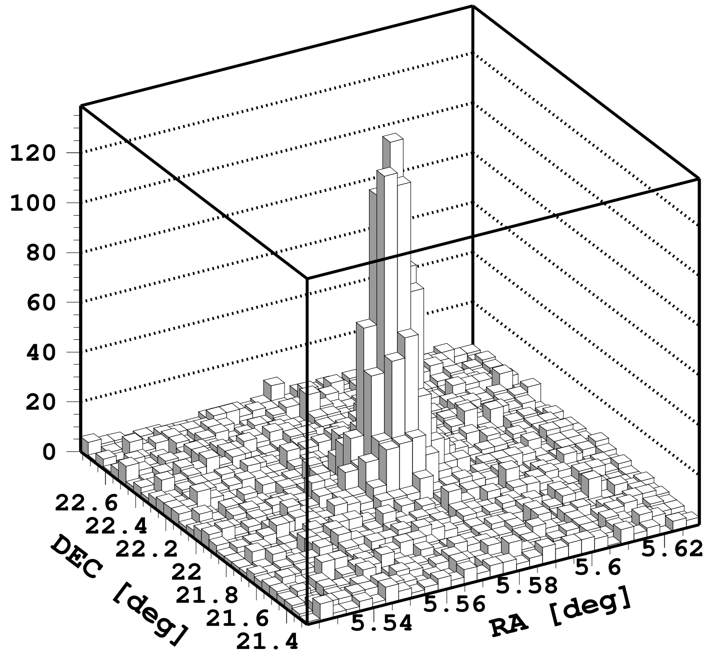

Figure 4.4: *Stereo-reconstruction of γ-ray-induced events coming from the direction of the Crab Nebula (RA(J2000): 5.576 hr; DEC(J2000): 22.014 deg) for events were at least 2 out of 5 telescopes have been triggered. Data sample from $\sim$ 32 hours taken with the HEGRA IACTs array.*

If a source emit γ-rays with a flux detectable by the instrument after a certain amount of time, an excess of events from the source position will be detected against the uniform CR background. In general, the excess is calculated as the difference: *(ON-source events)-(OFF-source events)*, usually after application of an angular and image shape cut. The OFF-source region needed to estimate the CR background content can be taken either in a dark sky region (where no γ-ray sources are known

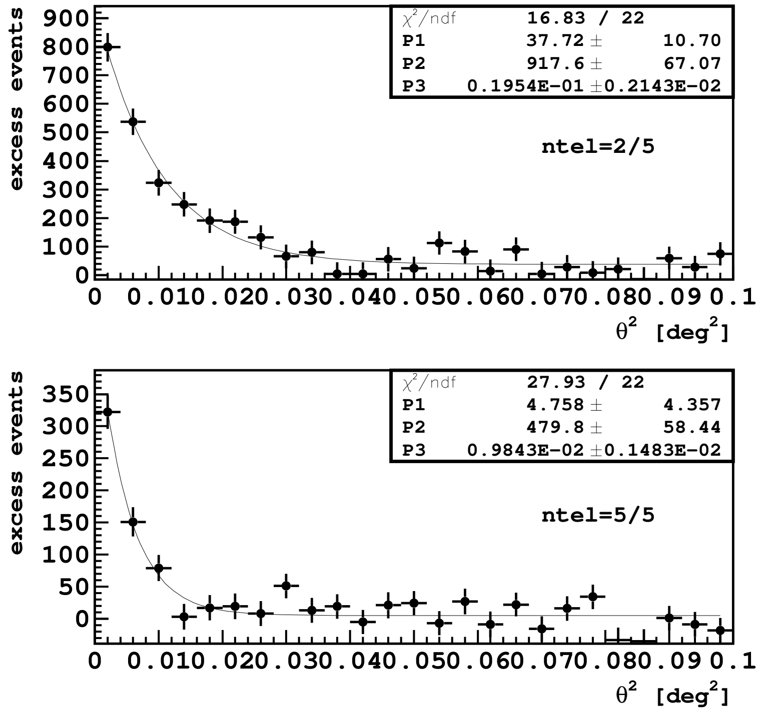

Figure 4.5: *Squared angular distance of the reconstructed excess events (ON-OFF) from the direction of the Crab Nebula, for two trigger multiplicities:* $n_{tel} = 2/5$ *(upper plot) and* $n_{tel} = 5/5$ *(lower plot). Shown is the correspondent radial Gaussian fit to the data (Eq. 4.1) and its relevant parameters.* $P3$ *corresponds to the squared angular resolution* σ^2 *of the HEGRA IACTs system. The OFF region is taken at 1° away from the source position (wobble mode of observation).*

to be present) or directly from the same field of view of the observation[1]. The large HEGRA IACTs FoV permits to observe a source in the so-called *wobble mode* of observation, in which the position of the source is shifted by 0.5° from the camera center and the corresponding OFF region is taken 1° away from the source position across the camera center. This observation mode allows to perform continuous ON-source observations. The significance of the excess, that is the probability that the excess is not due to a fluctuation in the CR background, can be estimated by means of Eqn.(17) reported in [77].

The distance θ between the true and reconstructed position of the γ source in

[1]If there are difference in the observation times between ON and OFF, a scaling factor $\alpha = T_{ON}/T_{OFF}$ must be introduced: excess=$\mathrm{N_{ON}} - \alpha \mathrm{N_{OFF}}$.

Table 4.2: *HEGRA IACTs system angular resolution for different trigger multiplicities.*

Trigger Multiplicity	$\theta_{68\%}$
$n_{tel} = 2/5$	~ 0.14
$n_{tel} = 3/5$	~ 0.13
$n_{tel} = 4/5$	~ 0.12
$n_{tel} = 5/5$	~ 0.10

the camera field of view can be assumed as a measure of the angular resolution of the IACTs system. An excess of events from a point-like source placed at the camera center can be described by:

$$\left(\frac{dN}{d\theta^2}\right) \propto e^{-\theta^2/2\sigma^2}$$

where σ is the projected angular resolution (defined as the radius within which the 68% of events are contained). Thus, the PSF of a point-like source is well fitted by:

$$F = P1 + P2\ \exp(-x/(P3/2)) \tag{4.1}$$

where $P3/2 = \sigma^2$.

Fig. 4.5 shows the squared distance of the reconstructed excess events from the direction of the Crab Nebula, which was observed in *wobble mode*, and the correspondent fit made using Eqn 4.1.

In general, the angular resolution heavily relies on the accuracy in the reconstruction of the image major axis, which in turn depends mainly on the image size and the core distance of the shower. Čerenkov images produced by air showers with relatively large impact distances show an elongated angular shape and permit an accurate determination of the image orientation. However, at very large distances of the core shower (only for central point sources) the images could be truncated by the camera edge, which worsens the angular resolution. Hence, the images with rather large number of photoelectrons (well above 40 ph.e) and with shower cores within the

Table 4.3: *CR air showers acceptances, k_{CR}, for different angular cuts $\Delta\Theta^2 < \Theta_0^2$ [deg]^2 calculated from a sample of Crab data. Trigger multiplicity: $n_{tel} \geq 3/5$.*

	$\Delta\Theta^2 < 0.01$	< 0.02	< 0.03	< 0.05
k_{CR}^{dir}	2.5×10^{-3}	4.3×10^{-3}	6.8×10^{-3}	1.5×10^{-2}

range of 50-200 m offer the best determination of the shower arriving direction [53]. That explains why, with the increase in primary energy of the shower, the angular resolution improves so much (for detailed discussion see [53] [85]). For the HEGRA array of IACTs the angular resolution for a 10 TeV γ-ray shower is a 20% better than for γ-ray showers around the energy threshold.

Finally, the angular resolution improves noticeably with the increasing trigger multiplicities (the more telescopes are triggered, the better is the stereoscopic reconstruction). Fig. 4.5 shows that increasing the trigger multiplicities from 2/5 up to 5/5 gives up to a 30% higher angular resolution. Remind that, at the same time, the use of higher trigger multiplicities leads to slightly higher energy threshold of the instrument. Table 4.2 reports the projected angular resolution for different trigger multiplicities. Note that, using a special technique described in [85] allows to lower the angular resolution down to 0.06°.

The very high angular resolution of the HEGRA system is already very effective in the rejection of the isotropic cosmic ray background. Table 4.3 reports the acceptances (that is, the fraction of remaining events after applying the directional cut) k_{CR}^{dir} for cosmic ray air showers, for different angular cuts, calculated from a sample of Crab data. An angular cut $\Delta\Theta < 0.03$ [deg^2] gives a rejection factor ($1/k_{CR}^{dir}$) as high as $\simeq 150$.

Using Crab data, we can calculate which is the optimum angular cut where the maximum excess significance is achieved. Figure 4.6 shows the significance of the excess calculated using Eqn.(17) in [77] as a function of the squared distance from the direction of the Crab Nebula. The maximum is achieved between $0.12° - 0.13°$. In general, the optimum angular cut can be estimated case-by-case using Crab data contemporaneous to the observations (if available) and can vary according to the

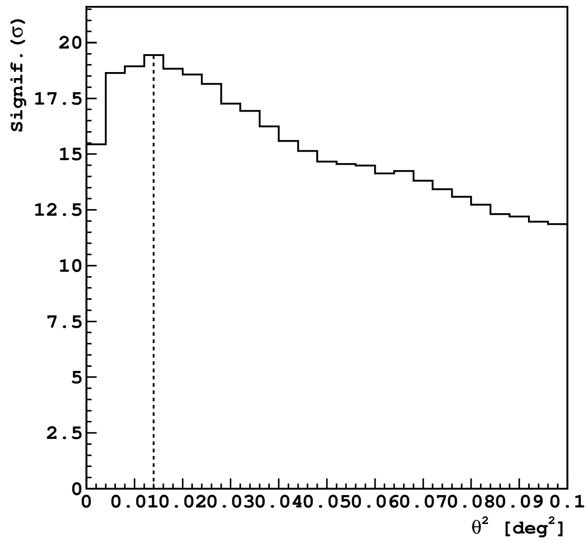

Figure 4.6: *Distribution of the significance of the excess as a function of the squared distance from the Crab nebula direction.*

ZA of the source: for higher ZA ($> 25°$) we will assume as optimum angular cut $\Delta\Theta < 0.13°$ (see Chapter §7).

In order to quantify the effectiveness of the angular cut (and, further on, of the image shape cut), a quality factor Q_F can be introduced:

$$Q_F = \frac{k_\gamma}{\sqrt{k_{CR}}} \ .$$

For the optimum angular cut, $\Theta_0 < 0.13$, ($k_\gamma^{dir} \simeq 0.7$) we got $k_{CR}^{dir} \simeq 4. \times 10^{-3}$ and a correspondent quality factor $Q_F^{dir} \sim 10$.

The reconstruction of the core location and the shower arrival directions shown in Fig. 4.3 ((a) and (b)) and Fig. 4.4 are derived from the intersection of the image major axes followed by an averaging of the intersections points. Other more accurate techniques to determine the shower parameters by a system of IACTs are discussed in [68], which include also the indetermination on the image center of gravity position and the image orientation. We shall make use of a more precise determination of the shower parameters in the search for γ-rays emission from potential extended sources.

4.5.3 Shower energy determination.

The stereoscopic system of IACTs has proven to be the most powerful tool for spectral studies of VHE γ-rays sources. As a single Čerenkov telescope cannot measure with high precision the shower core position, it is more difficult to relate the Čerenkov photons density measured at the telescope location with the shower energy. That results in a poorer energy resolution, not lower than 40%. Techniques have been developed to relate the shower core with the location and shape of the Čerenkov image within the camera, which permit to increase the resolution up to 25%-30% [69].

As we have seen previously, the shower core and the image SIZE parameter (that is, the total number of ph.e. in the image (§ 3.2)) are directly related with the energy shower. Hence, the shower energy can be calculated as inverse function of these two quantities (also depending on the zenith angle of observation). In a stereoscopic system the shower core location and its distance from a given telescope (the impact distances) of the array can be obtained by a simple geometrical reconstruction and with high precision, which permits to efficiently relate the light yields of the shower to the energy of the primary, allowing energy resolutions between 15% to 25% (see Fig 4.7).

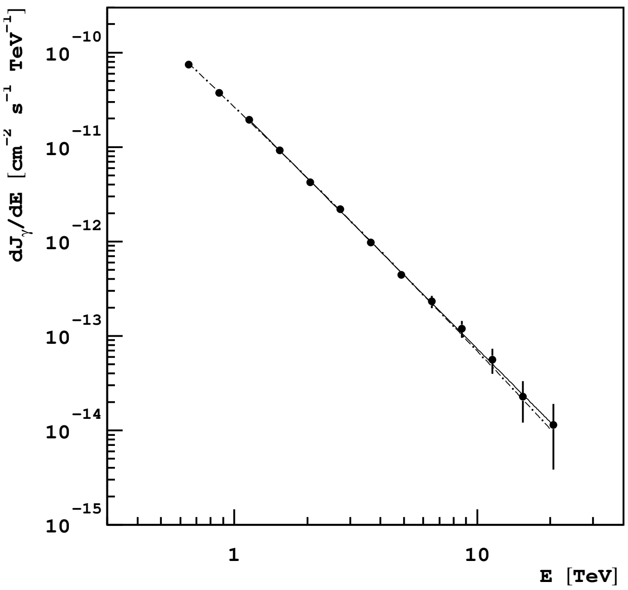

Figure 4.7: *Differential energy spectrum of the Crab nebula as measured by the HEGRA IACTs system (from [60]).*

4.6 γ/hadron separation using multiple Čerenkov images.

Apart from the directional information, which alone already provides a good CR background rejection in a system of IACTs, the hadron background suppression is also based on the noticeable differences between the development of γ- and proton-induced air showers, which are converted in a different "imaging" of the showers in the camera plane, as we have seen in the previous chapter. This permits to further reduce the CR background in order to search for γ-ray signal from the direction to the observed object.

In a single IAC telescope the γ-hadron separation is implemented applying fixed cuts on the image shape parameters: WIDTH$\leq w_0$, LENGTH$\leq l_0$, and so on. In general, the image parameters vary with the energy and impact point of a shower: the images of high energy γ-ray showers detected close to the telescopes system embrace many more pixels as compared to the low energy events or to the same event but at rather large impact distance. Furthermore, showers with different impact points will produce differences in the parameters due to the decrease of the Čerenkov photon density with the core distance. Thus, using the standard second moment analysis (App. A), one could obtain very different angular sizes for the recorded images, depending on the primary shower energy and shower impact distance. Then, it is clear that for an individual IAC variable cuts must be applied in order not to reject a significant fraction of γ-rays events.

For the HEGRA IACTs system, the γ-hadron separation is based on the so-called *mean scaled WIDTH (mscw)* cut [53], which makes use of a correlated image shape analysis. Instead of applying a multi-fold cut on the image parameter WIDTH for each single image, a single parameter cut is applied, which works very efficiently against the CR background events and improves the CR rejection up to a factor of 100. Though the images in different projections are not independent of each other, the images detected by each of the spatially separated telescopes are only partially correlated and their correlated analysis significantly improves the γ-hadron separation.

As we said before, the stereoscopic reconstruction of the core location allows to calculate the impact distances R to each telescope and to evaluate the energy E_0

of the primaries for each individual event. Using Monte Carlo simulated γ-rays-induced air showers of different energies and zenith angles, we can sort the resulting Čerenkov images for each telescope into several bins according to the value of the impact distances from each telescope, ΔR_i $(i = 1, ..n)$, and the image amplitudes in photo-electrons (that is, the image parameter SIZE), $\Delta log(S_j)$ $(j = 1, .., m)$. Then, we can derive the average image shape parameters for each bin interval [55].

In order to compensate for the dependence of the image shape upon the energy of the shower-inducing primary and the impact distance, the parameter WIDTH for each telescope is scaled according to the value predicted from the MC simulated γ-rays and corresponding to the shower core position and impact distances reconstructed for that particular event.

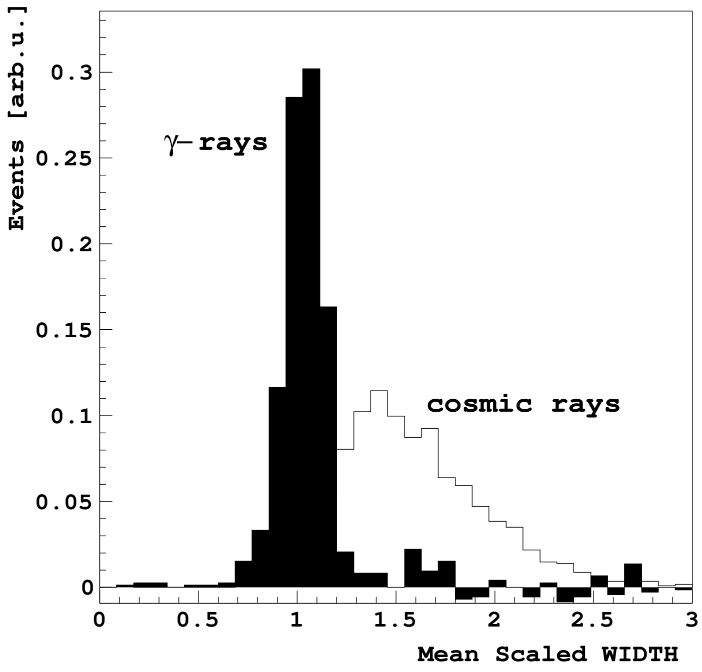

Figure 4.8: *Distributions of the mean scaled WIDTH parameter for γ-rays (filled hatched histogram) and cosmic rays (solid line histogram). The γ-ray- and cosmic ray-like events are derived from a sample of Crab nebula data.*

After a scaled WIDTH $\tilde{w}$ is calculated for each telescope, the mean scaled WIDTH is defined for that particular event by summing all over the N triggered telescopes:

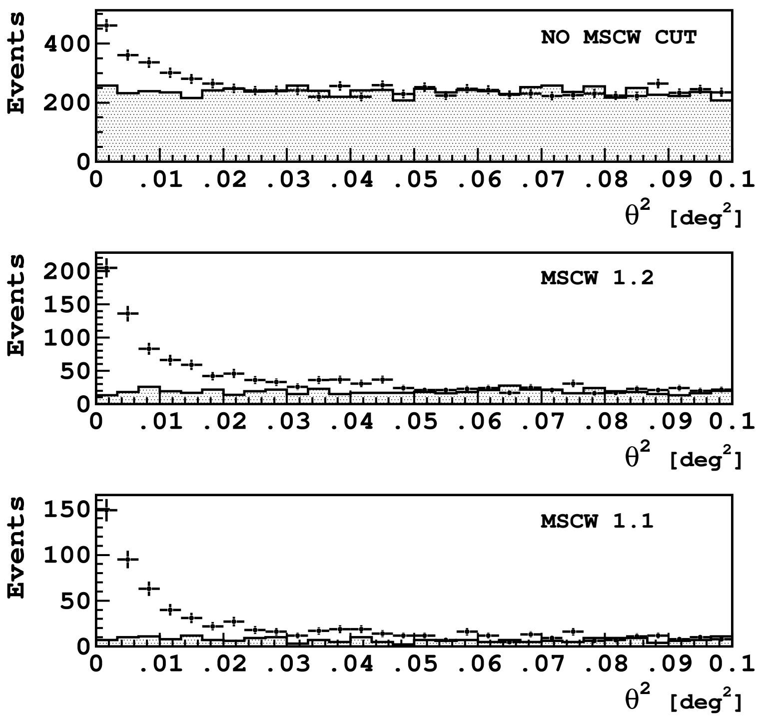

Figure 4.9: *Squared distance of the HEGRA stereo-reconstructed events from the direction of the Crab Nebula (filled dot points) and the region chosen for the CR background determination (hatched histogram) placed* 1° *away from the source position (wobble mode of observation). Different mean scaled WIDTH cuts (mscw) have been applied in order to separate* γ*-rays from hadrons. Trigger multiplicity:* $n_{tel} \geq 3/5$.

$$\langle \tilde{w} \rangle = \frac{1}{N} \sum_{k=1}^{N} \frac{w^k}{\langle w \rangle_{ij}^k} \tag{4.2}$$

where $\langle w \rangle_{ij}^k$ is the expected mean image WIDTH produced by a γ-ray for the $k-$th telescope calculated beforehand out of the MC simulations for the $i-$th bin of reconstructed impact distance and the $j-$th bin of the measured amplitude.

The distribution of the *mscw* parameter for γ-rays is very narrow and has a peak around 1.0 (see Fig. 4.8) because, after the scaling procedure, the RMS of the image distributions do not depend anymore on the image size and shower impact distance but only on the image fluctuations.

Figure 4.9 shows the squared distance of the stereo-reconstructed events from the

Table 4.4: *γ- and cosmic-rays acceptances for different mean scaled WIDTH cuts and for the trigger multiplicities $n_{tel} \geq 3/5$ and $n_{tel} \geq 5/5$. Also the Q-factors for the image shape cuts are shown. The ON and OFF events are calculated from around 32 hrs of Crab data taken in wobble mode.*

Shape cut	*ON*	*OFF*	*Excess*	κ_γ	κ_{CR}	Q_F^{sh}
– $n_{tel} \geq 3/5$ –						
no cut	3879	2345	1534	–	–	–
$\langle \tilde{w} \rangle < 1.2$	1582	196	1386	0.90	0.08	3.2
$\langle \tilde{w} \rangle < 1.1$	1135	96	1039	0.68	0.04	3.4
$\langle \tilde{w} \rangle < 1.0$	508	36	472	0.31	0.015	2.5
– $n_{tel} = 5/5$ –						
no cut	1291	736	555	–	–	–
$\langle \tilde{w} \rangle < 1.2$	549	46	503	0.91	0.06	3.7
$\langle \tilde{w} \rangle < 1.1$	410	19	391	0.70	0.03	4.0
$\langle \tilde{w} \rangle < 1.0$	155	7	148	0.27	0.01	2.7

direction of the Crab Nebula, observed in *wobble mode*, for two different *mscw* cuts: $\langle w \rangle < 1.2$ and $\langle w \rangle < 1.1$. Note that, thanks to the very good angular resolution of the HEGRA IACTs system, the Crab Nebula is already visible without any image shape cut (upper panel of Fig. 4.9).

The *mscw* cut allows a very effective γ/hadron separation. For events with a trigger multiplicity of at least 3 out of 5 telescopes (or higher), a cut on $\langle \tilde{w} \rangle < 1.1$ keeps up to 70% of the γ-rays while reducing the CR background contamination down to 10^{-2}.

Table 4.4 shows the γ-rays and cosmic ray acceptances and the correspondent Q-factors for the image shape cuts, Q_F^{sh}, calculated from a Crab data sample for different *mscw* cuts and two different trigger multiplicities.

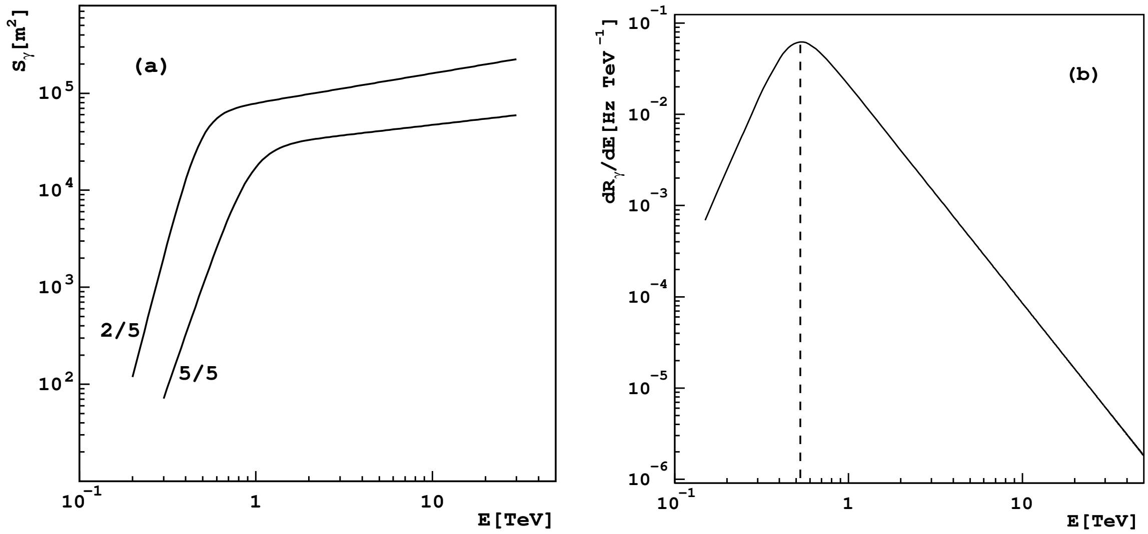

Figure 4.10: *(a): Effective areas for the HEGRA IACTs system calculated from MC simulated vertical showers and for the trigger multiplicities $n_{tel} = 2/5$ and $n_{tel} = 5/5$; (b) Differential trigger rates calculated from the Crab differential spectrum reported in [60] using the effective area shown on the left. The peak of the curve is assumed as the energy threshold of the HEGRA IACTs system ($E_{th} \simeq 500$ GeV).*

4.7 The effective area and the energy threshold of the HEGRA IACTs system

In § 3.3 and § 3.4 we have introduced the concept of effective area and energy threshold of a Čerenkov telescope. Figure 4.10 (a) shows the effective areas calculated from MC simulated vertical γ-rays showers and for two different trigger multiplicities (trigger threshold 8 ph.e). The behaviour of the effective area depends on the lateral distribution of the Čerenkov light at the observational level. As it is possible to see in Fig. 4.10 (a), the effective area shows a rapid increase up to 1 TeV followed by a logarithmic growth for higher energies. That is due to the fact that showers with great energies can be detected at great impact distances, given their larger Čerenkov light pool.

The highest trigger multiplicity $n_{tel} = 5/5$ shows a lower effective area than the lowest multiplicity $n_{tel} = 2/5$ [2]. That is because, in order to have all the five telescopes

[2]In general, that is true also for trigger multiplicities greater than 2 out 5 telescopes.

triggered, the core of the shower cannot be too far, otherwise the light pool will not be able to cover all the system; thus, the ability to detected showers with larger impact distances and, consequently, the effective area, is reduced.

For higher zenith angles ($ZA > 30°$), the collection areas are lower for energies $E \leq 3$ TeV than the areas provided for observations at the zenith, but are higher at energies above 3 TeV. This is due to the fact that at higher ZA the showers develop much higher in the atmosphere and, though the same amount of Čerenkov light is produced, the photon density at the ground is lower since the Čerenkov light pool is more extended. That means that only very high energy showers (that is, with a higher photon density on the ground) are able to trigger the telescopes and the effective area becomes much larger because of the larger size of the Čerenkov pool at the ground.

At the beginning of this chapter, we have said that including more than one IAC telescope in the extended air showers observation allows to reduce the trigger threshold for each telescope of the system, hence to reduce the energy threshold of the detector. Here, we define as energy threshold of the system the peak of the differential trigger rates. Giving a γ-rays source with a energy spectrum following a power law with spectral index α_γ:

$$dJ_\gamma/dE = A \cdot E^{-\alpha_\gamma}$$

the differential trigger rates is defined as:

$$\frac{dR_\gamma}{dE} = \left(\frac{dJ_\gamma}{dE}\right) A_\gamma(E) \qquad [\text{Hz TeV}^{-1}] \tag{4.3}$$

where $A_\gamma(E)$ is the effective area of the system. Integrating between 0 and ∞ we get the γ-rays detection rate R_γ.

Figure 4.10 (b) shows the differential trigger rates calculated using the Crab Nebula spectrum measured by the HEGRA IACTs system (see [60] and Fig. 4.7) and the effective area for $n_{tel} = 2/5$ shown in Figure 4.10 (a). The curve peaks at around 500 GeV which is assumed as the energy threshold E_{th} of the HEGRA system.

In the next chapter, we will show the technique used to lower the energy threshold of the HEGRA IACTs system down to around 300-350 GeV [52].

4.8 Sensitivity to γ-ray fluxes

The observation of the standard candle in γ-ray astronomy, the Crab Nebula, allows to quantify the sensitivity of the HEGRA IACTs to the observation of point-like sources[3] [4].

The Crab Nebula is detected by the HEGRA IACTs system at the level of $\sim 5.6\sigma$ after one hour of observation, after application of the optimum angular cut calculated beforehand, $\Delta\Theta^2 < 0.0169$ [deg^2], and a *mscw* cut $\langle\tilde{w}\rangle < 1.2$, which keeps up to 82% of the γ-rays events for the trigger multiplicities $n_{tel} \geq 2/5$.

The well measured Crab Nebula energy spectrum permits to calculate the integral Crab flux for energies above the threshold:

$$\Phi_{Crab}\,(E > 500\ GeV) = 1.6 \times 10^{-11}\ \mathrm{ph\ cm^{-2}s^{-1}}\ .$$

The detections of very weak sources like Cas A [18] and the unidentified source close to the Cygnus OB2 association [33], have shown the capability of the HEGRA system to detect sources at the centi-Crab level (for example, the integral γ-rays flux measured from Cas A amounts to 3% of the Crab flux) after more than 100 observation hours.

In general, the signal-to-noise ratio, S/N, in observations with the HEGRA system of IACTs can be estimated as:

$$S/N = \frac{\tilde{R}_\gamma}{\sqrt{\tilde{R}_{CR}}}\sqrt{T_{obs}} = \frac{R_\gamma}{\sqrt{R_{CR}}} Q_F^{dir} Q_F^{sh} \sqrt{T_{obs}} \tag{4.4}$$

where $\tilde{R}_\gamma$, $\tilde{R}_{CR}$ are the detection rates of γ-rays and cosmic rays, respectively, after applying the angular and image shape cuts defined through the quality factors calculated previously.

Giving the CR rates as measured by the HEGRA IACTs system (see Table 4.4) and the acceptances calculated beforehand, using Eqn. 4.4 it is possible to estimate what is the time needed to detected a source at the level of, for example, 10% of the Crab Flux level and at a 5σ level above the background[5]. Such a detection is possible in 20 hours of observation.

[3] In Chapter § 6 we will calculate the sensitivity to the observation of extended sources.

[4] Alternatively, MC simulations can be used to determine such sensitivity [53].

[5] This is generally assumed as the minimum excess significance needed to claim a detection of a new VHE γ-rays source.

Chapter 5

A technique to lower the energy threshold of IAC telescopes: the topological trigger.

5.1 Physical motivations

The observations of the Crab Nebula for a total of about 250 hrs performed with the HEGRA stereoscopic system of 5 IACTs in the standard operational mode, have proven the energy threshold of the system to be 500 GeV for small zenith angles (ZA$\leq 20^{\circ}$) (see § 4.7).

Ground-based TeV γ-ray astronomy has effectively exploited the stereoscopic technique using a system of IACT in the study of γ-ray emission arising from a few well established sources and for a general search amongst large numbers of γ-ray source candidates [70]. Given the rather steep energy spectra measured for the discovered γ-ray sources and for those predicted as potential candidates, a substantial advancement in the sensitivity of IACT techniques can be reached if considerable lowering of the energy threshold of the instrument is achieved. For such spectra, a low energy threshold can provide a high γ-ray rate and, correspondingly, a high sensitivity of the instrument. Nowadays a number of instruments perform observations at the effective energy threshold as low as 250 GeV [70].

Further reduction of the energy threshold could be achieved by using of *(i)* larger optical reflectors (10-20 m in diameter) to increase the photon collection efficiency for the low energy γ-ray showers; *(ii)* imaging cameras equipped with pixels of a relatively small angular size ($0.1^{\circ} - 0.15^{\circ}$), to reduce the background night sky light per pixel; and finally, *(iii)* by operating a number of telescopes simultaneously in the *stereoscopic* observational mode, which allows to reduce the trigger threshold by requiring coincidences in a number of telescopes, as in the HEGRA IACTs system.

Lowering the energy threshold of the Čerenkov telescopes is not only motivated by the enhancement of the instrument sensitivity but it is also physically important in order to extend the spectral studies of the γ-ray emission to lower energies. For example, the Inverse Compton (IC) modeling of the γ-ray spectrum of the Crab Nebula, taken along with the EGRET detection at GeV energies [71, 24], predicts a substantial spectral flattening down to energies of 200-300 GeV, whereas above 1 TeV the spectrum is well described by a power-law of spectral index -2.6. The measurement of such change in the spectrum slope would favor the IC model of γ-ray emission. First evidence for deviation from a straightforward power law was suggested by the WHIPPLE group (see [25, 72]) and, subsequently, it was confirmed by other measurements made within that energy range by STACEE [73], CELESTE[74], and CAT [75].

In what follows, we shall discuss a new approach to detect low energy γ-rays with the system of IACTs HEGRA by use of a *topological trigger* system along with the so-called *convergent* observational mode [52]. That allows to reduce considerably the local trigger threshold and, correspondingly, the energy threshold of the instrument down to 300-350 GeV. Relevant Monte Carlo simulations (§ 5.3) and trigger tests (§ 5.4) have been done in order to prove the efficiency of such observational technique. Finally, we have performed observations of the Crab Nebula for a total amount of 15 hours using the topological trigger technique using the convergent observational mode (§ 5.5). Analysis of these data has shown an excess attributed to γ-ray showers at energies well below 500 GeV (§ 5.6). Assuming the shape of the energy spectrum as measured by the HEGRA system of telescopes [60], we finally estimated the integral flux of γ-rays from the Crab Nebula above the new energy threshold of 350 GeV (§ 5.7), which is roughly a factor 1.4 lower than the nominal value.

5.2 Trigger modes

For most of its operational time the HEGRA IACT system was running using a *standard two-level* trigger, requiring for at least two-next-neighbour PMTs of each camera to exceed the trigger threshold of 7-8 ph.e. and at least two telescopes to be triggered by the same shower within a given coincidence time window (see § 4.3).

A trigger threshold of 7-8 ph.e. is high enough to suppress accidental triggers due to illumination of the camera PMTs (pixels) by the night sky light background. At first, the choice of the trigger is determined by the average amount of night sky light photons hitting the camera pixel within a trigger gate, which is of 20-30 ns. This value is equivalent to 1 ph.e. for the HEGRA telescopes and it is set by the size of the optical reflector, the angular size of the camera pixels, and the efficiency of the light detectors (the PMTs). Secondly, the choice of the trigger threshold depends on the designed trigger logics and finally on the total number of camera pixels included into the trigger zone. Selecting a smaller number of pixels as active trigger zone, a reduced number of accidental coincidences is possible and, consequently, lower trigger thresholds can be chosen.

The trigger threshold limits the energy of the atmospheric showers, which should be sufficiently powerful to generate a certain number of Čerenkov photons and trigger the camera. Note that low energy γ-ray-induced atmospheric showers can produce a sufficient amount of Čerenkov light photons only at rather small distances from the shower core ($r \leq 50$ m). Using only 4-telescope coincidence events for the HEGRA system of IACTs, these low energy γ-ray showers appear to be concentrated within the geometrical area of the array. In addition, the Čerenkov light images of such showers occur in specific parts of the camera for each of the system telescopes, which are determined by the location of the telescopes within the array. By intention, to force the system to detect only low energy γ-ray showers, one can restrict the active trigger zone to those specific parts of the camera which are sensitive to these events. A reduction of the trigger zone by a factor of about 7 allows to decrease the value of the trigger threshold down to 4 ph.e. and, therefore, to achieve a considerable enhancement in the trigger rate of low energy γ-ray showers. This so-called *topological trigger* mode is effective for detection of low energy γ-rays, whereas the rate of γ

photons with energies well above the energy threshold of the system, will be drastically reduced due to the rather narrow trigger zone.

In order to achieve very high detection rates at low energies, one could try as well to operate the HEGRA telescopes in the standard trigger mode at the very low trigger threshold of 4 ph.e. However, that would imply a drastic increase in the accidental trigger rate of up to 100 Hz and an increase of up to a 30% in the dead time (against a rate of 15 Hz and 5% dead time for the nominal trigger threshold of 7 ph.e. (see [66])). Moreover, the current data acquisition system would not support such rate. It would be possible then, to increase the trigger multiplicity and ask for at least 4 telescopes out of 5 to be triggered, but in this case, as we already mentioned previously and we will show below through the Monte Carlo simulations, we do not need to use the whole camera as active trigger zone, since only certain parts of the camera will be covered by the Čerenkov images produced by the low energy events.

In the next sections, we will discuss in detail the implications of using a *topological trigger* mode.

5.3 Simulations

Based on the HEGRA Monte Carlo simulations, we have estimated the detection rates of cosmic rays and γ-rays as well as the energy threshold for the HEGRA IACTs array using the *topological* trigger mode. For such trigger mode one has to use restricted trigger zones within the camera field of view (FoV) for each of the system telescopes. These zones are adjusted to the regions of most frequent appearance of the γ-ray images. For instance, a restriction on the impact distance from the center of the IACT system at 50 m. yields a specific distribution of γ-ray events in the telescope camera focal plane (see Figure 5.1)[1]. As it is seen from Figure 5.1 all events are localized within an angular area roughly corresponding to 19-37 camera pixels. The location of the active trigger zone in the camera field of view differs from one telescope to another and is determined by the geometrical layout of the telescopes in the array. In the simulations, we have assumed that the optical axes of all system telescopes are parallel, which represents the conventional mode of telescope tracking. One can see

[1] The maximum impact distance for the simulated γ-ray showers was 500 m.

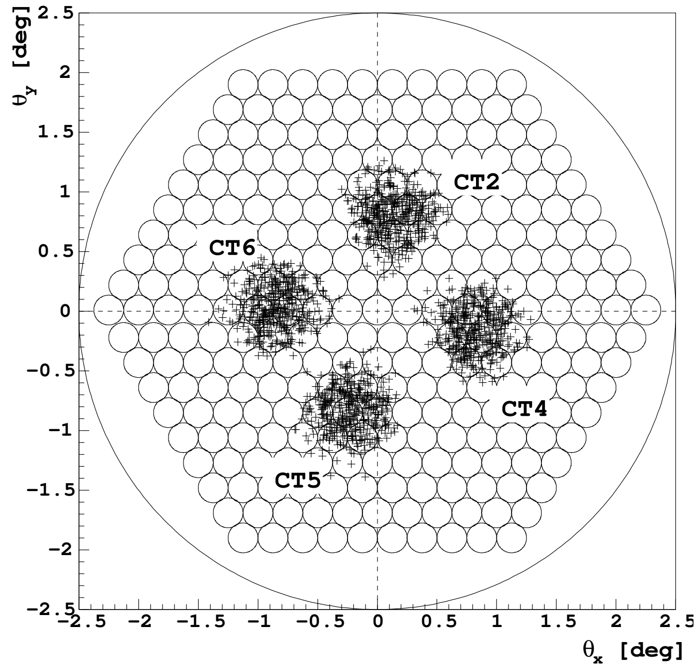

Figure 5.1: *Two-dimensional distribution of the centroid positions in camera coordinates for γ-ray images, triggering at least 4 telescopes of the HEGRA IACT array and passing the selection of the impact distance from the center of the system less than 50 m. (black points). Simulations have been done for showers at zenith. CT3 is not shown.*

in Figure 5.1 that the corresponding cluster of triggered events is shifted by about 0.6° from the camera center, which roughly corresponds to 3 camera pixels.

Using MC simulations, we have made calculations of the cosmic and γ-ray detection rates using two different trigger modes: a *standard* local trigger mode of $2NN/271 > q_0$, where q_0 is the trigger threshold measured in photoelectrons, and a *topological* trigger mode of $2NN/19 > q_0$, where only 19 pixels were selected for each telescope according to the specifically established trigger zone. In both cases, a global trigger of at least 4 telescopes out of 5 to be triggered by a shower was applied. The detection rates of cosmic rays and γ-rays calculated for different values of trigger thresholds q_0 are shown in Figure 5.2.

The HEGRA system of IACTs runs in the *standard* trigger mode with the trigger threshold set to $\simeq 8$ ph.e. That yields a corresponding detection rate of about 4 Hz for the 4-fold coincidences, which is in a good agreement with the measurements (see Table 4.4). Note that the detection rates of cosmic rays differ by a factor of about 10 between the two different trigger modes (see Figure 5.2), roughly agreeing with the simple estimate based on the number of the pixels included in the trigger ($271/19 = 14$).

In reality, in the experimental data we have found a non uniform rate over the whole camera field of view, which is due to several reasons: a non equal optical smearing of the reflector mirrors (broader at larger angular distances from the center of FoV), a restricted number of trigger patterns for the images being close to the camera edge (e.g., images with two pixels on the ring), etc. All these effects reduce the number of possible combinations for the $2NN/M$ trigger logic (which is roughly $3 \times M$, where M is the total number of pixels in the camera, for HEGRA telescopes $M = 271$) and, consequently, the total rate in the standard trigger mode. Using the *topological* trigger mode with the local trigger threshold set at 4 ph.e.,

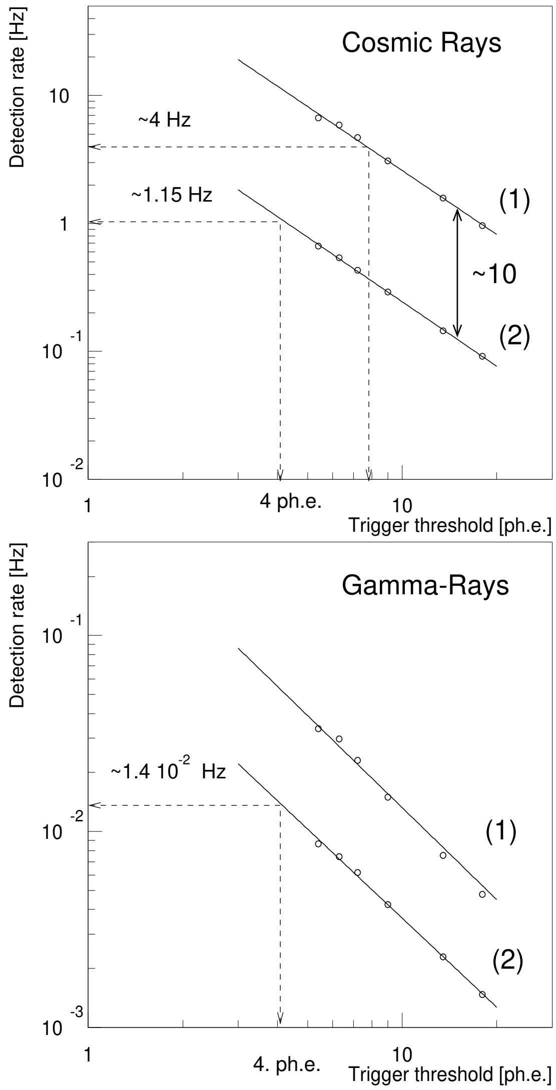

Figure 5.2: *Detection rates of cosmic rays and γ-rays calculated from MC simulations for different values of trigger thresholds (q_0) and for two different trigger modes, (1) standard: 4 telescopes out of 5, $2NN/271 > q_0$, and (2) topological: 4 telescopes out of 5, $2NN/19 > q_0$. Also the rates for $q_0 = 4$ ph.e. and the correspondent fits are shown. Simulations have been done for showers at the zenith using parallel tracking in both cases.*

the cosmic ray detection rate is about 1.15 Hz. That is somewhat higher than the measured rate for a configuration with 19 pixels in trigger (see paragraph 5.4). However, given the imperfect adjustment of the trigger window for the rate measurements in the topological trigger mode (due to telescope pointing error) as well as slight differences between Monte Carlo assumed trigger thresholds and those actually used in observations (e.g., due to a real mirror reflectivity a 20% lower than that one assumed in the MC), one can conclude a rather good agreement between measured and calculated rates.

For the *topological* trigger mode the calculated γ-ray rate is $1.4 \cdot 10^{-2}$ Hz (50 γ's per hr) (see Fig. 5.2). In the calculations, we have assumed the γ-ray energy spectrum of the Crab Nebula as measured by the HEGRA collaboration [60]. The dependence of the evaluated energy threshold with the value of the trigger threshold q_0 [ph.e.] can be well fitted by

$$log(E\ [\mathrm{TeV}]) = -1.0 + 0.9 \cdot \log(\mathrm{q_0}) \tag{5.1}$$

Thus for the *topological* trigger mode and the conventional trigger threshold $q_0 =$ 8 ph.e., the energy threshold is about 500 GeV, whereas for the reduced trigger threshold, $q_0 = 4$ ph.e., the energy threshold is of $\simeq 350$ GeV. Such substantial lowering of the energy threshold by a factor 1.4 with respect to the *standard* trigger mode could only be achieved by implementing a corresponding upgrade of the telescope hardware, e.g. towards much larger effective collection area of the optical reflector.

For the event classification, both the reconstructed shower direction and the averaged angular size of the Čerenkov light images were used in the present analysis. Images recorded at such low energy threshold contain a rather small number of photoelectrons, and the image orientation for those events is poorly determined. However, using four images per each individual event it is possible to substantially improve the angular resolution. Thus, for a rather loose angular cut of $\theta^2 \leq 0.05$ [deg^2], the Monte Carlo simulations predict, for the *topological* trigger mode and an active trigger zone of 19 PMTs, a γ-rays and a cosmic ray acceptances of $\kappa_\gamma^{dir} \simeq 0.7$ and $\kappa_{CR}^{dir} \simeq 0.05$, respectively, and a quality factor $Q_F^{dir} = \kappa_\gamma^{dir}/\sqrt{\kappa_{CR}^{dir}} \simeq 3.2$.

As we have seen in the previous chapter, further improvement of the signal-to-noise ratio is achieved by using the differences in the image shape between the cosmic ray- and γ-ray-induced showers which, for a stereoscopic system of IACTs, are defined through the *mean scaled WIDTH* parameter (see § 3.2). Nevertheless, when the observation is carried on using the *topological trigger* mode, the selected showers are concentrated within the telescope array, and therefore occur at small impact distances from the center of the array. The dynamic energy range of these events is also very limited, from 100 GeV up to few TeV. In such a case, the *scaling* of the angular image size (the WIDTH) is not necessary anymore, and one can simply use the initial WIDTH parameter for an effective image classification. Thus, all triggered cosmic ray and γ-ray events can be plotted versus *mean WIDTH* $\langle W \rangle$, defined as:

$$\langle W \rangle = \sum_i^N A_i W_i / \sum_i^N A_i \tag{5.2}$$

where W_i and A_i are the WIDTH and SIZE parameter, respectively, measured for each of the N triggered telescope (N=4 or 5). The mean image SIZE is given by

$$\langle A \rangle = \frac{1}{N} \sum_i^N A_i \tag{5.3}$$

The *mean WIDTH* distributions for MC simulated events induced by cosmic rays and γ-ray are shown in Figure 5.3. One can see from Figure 5.3 that the parameter $\langle W \rangle$ enables a rather good rejection of cosmic ray showers. The post-cut γ-ray and cosmic ray acceptances calculated for the *topological* trigger with 19 active PMTs and after applying an image shape cut of $\langle W \rangle < 0.12$ are $\kappa_\gamma^{sh} \simeq 0.72$ and $\kappa_{CR}^{sh} \simeq 0.082$, respectively, with a corresponding signal enhancement factor of $Q_F^{sh} \simeq 2.5$.

The signal-to-noise ratio in observations with the HEGRA system of IACTs running with the topological trigger for the reduced trigger threshold can be finally estimated using Eqn. 4.4. For 1 observation hour of the Crab Nebula, we expect a significance S/N $\simeq 6\sigma$ for a 19 PMT trigger zone. Nevertheless, for the trigger zone of 37 pixels actually used in the observations of the Crab Nebula[2] (see § 5.5), the integral γ-ray rate from a point-like source remains nearly the same, whereas the rate of cosmic rays, which are randomly distributed over the solid angle, increases due to the substantially broader trigger region. Therefore, we may expect a lower significance of around $4\sigma/\sqrt{hr}$.

[2] The choice of a 37 pixel trigger zone was forced by the uncertainties in the orientational tilt of the telescopes.

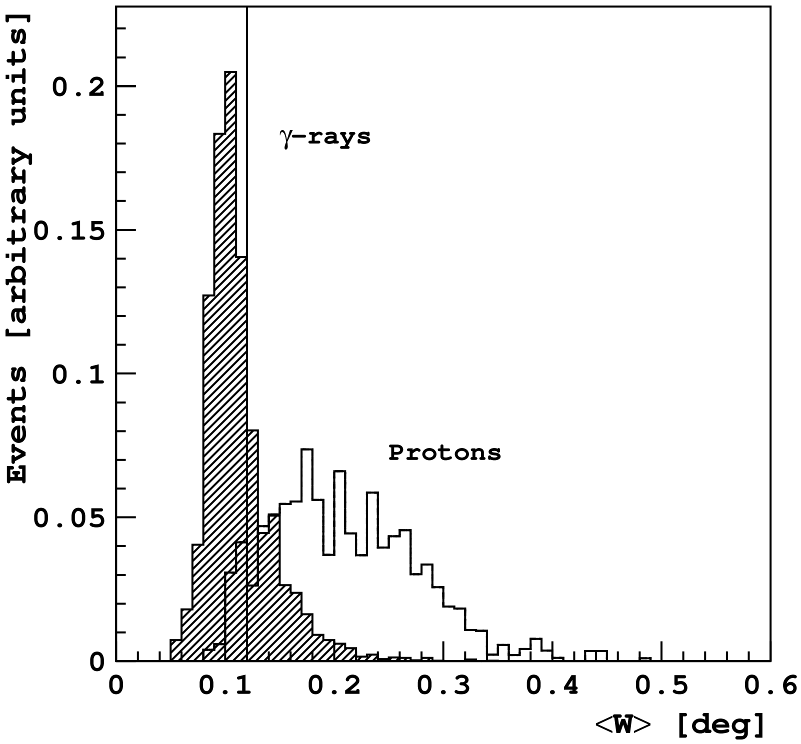

Figure 5.3: *Distributions of the parameter $\langle W \rangle$ for atmospheric cosmic ray- and γ-ray-induced showers. The vertical solid line indicates the cut applied in the analysis, $\langle W \rangle \leq 0.12°$.*

The expected γ-ray rate was calculated assuming the Crab Nebula spectrum at energies above 100 GeV as a power-law with a spectral index of 2.6 and the flux normalization taken from [60]. Actually, as measured by the HEGRA IACTs system [60], the Crab Nebula spectrum shows a slight flattening in the spectrum slope towards low energies, which is consistent with the theoretical expectations (see [71, 24]), and which results in a roughly 30% lower γ-ray rate. Thus, the estimate of the trigger performance is finally $\simeq 3\sigma/\sqrt{hr}$ for an active trigger zone of 37 pixels. Therefore, 9 hours of observations (37 pixels trigger mode) will provide a detection of the Crab Nebula above $\simeq$ 350 GeV with a confidence level of $\sim 9\sigma$.

Table 5.1: *Summary of the test runs taken with the HEGRA system of IACTs in the topological trigger mode. Shown in bold is the most stable configuration found.*

G/G_0	q_0^{DMC} [mV]	q_0 [ph.e]	System rate [Hz]	Telescope rate [Hz]	Pixel rate [Hz]
1.0	8	6.7	0.41	1-7	$3 \cdot 10^2$
1.53	8	4.38	0.64	5-92	$2 \cdot 10^3$
1.45	**7**	**4.04**	**0.89**	**8-320**	$\mathbf{4 \cdot 10^3}$
1.43	6	3.51	0.94	37-$1.8{\cdot}10^3$	10^4
2.07	8	3.24	0.19	$2.2{\cdot}10^2 - 7.7 \cdot 10^3$	$1.5 \cdot 10^4$
1.89	7	3.10	0.02	$1.4{\cdot}10^3 - 8.5 \cdot 10^4$	$3 \cdot 10^4$
2.40	8	2.79	0.00	$15 - 3.7 \cdot 10^3$	$4 \cdot 10^4$

5.4 Tests of trigger threshold

In order to find the lowest possible threshold to use in the *topological* trigger mode, different trigger configurations as well as the stability for alternating ON and OFF viewing modes[3] were tested in detail for the HEGRA system of IACTs. The local trigger threshold was lowered both by decreasing the threshold of the Discriminator-Monitor-Cards (DMC)[4] and by increasing the high voltage (HV) of the PMTs. 19 pixels were included into the active trigger zones for each camera and their localization was calculated using the altitude and azimuth of the viewing angle and the actual position of the telescopes in the array. The system was running in the 4-telescope coincidence mode and data runs were taken at 20 degrees of zenith angle. Table 5.1 gives a summary of the tested configurations.

Listed are the gains of the PMTs with respect to the nominal gain G_0, which

[3]In the ON and OFF viewing mode, the data are taken while tracking alternatively the source position (ON) and the sky region chosen for estimate of the background (OFF), which is usually placed at $\pm 5°$ away in right ascension from the nominal source position.

[4]The DMC are used to verify whether a signal in a single PMT exceeds a certain limit in ph.e. (with a maximum of 80 mV equivalent to a range of roughly 0 to 70 ph.e.) and, in the positive case, to generate a 17 ns pulse supplied into the majority unit (see for detailed discussion [66])

is calculated from the mean anode currents. The DMC threshold q_0^{DMC} is given in mV, whereas the threshold q_0 is measured in photoelectrons[5]. The typical system event rate, the event rate for an individual telescope and the single pixel rate are summarized in Table 5.1. The ratio G/G_0 indicates the change of the gain after decreasing the threshold.

The lowest stable trigger threshold before the single pixel rates exploded was found to be 4.0 ph.e., which corresponds to a PMT gain of 1.45 times the nominal and a threshold of 7 mV. The corresponding system trigger rate was about of 0.89 Hz. The nominal threshold was 6.7 ph.e., with a DMC threshold of 8 mV, and 1.2 mV/ph.e. The stability of this configuration was tested by changing night sky background conditions, using a number of 10-minute runs taken with the telescopes positioned at an altitude of 80° and azimuth 0° and brought back to this position at the end of every run. Within given statistics, for different nights and different night sky backgrounds, the system trigger rate was always the same for all runs[6].

5.5 Summary of Crab Nebula data taken in convergent mode

The observations of the Crab Nebula using the *topological* trigger were performed in the so called *convergent* data taking mode (see [76]) instead of the usual parallel mode. In the convergent observational mode, the optical axes of the telescopes intersect at the typical height of the maximum shower development (6-8 km above the sea), instead of being parallel as they are in the standard parallel mode. The *intersection area* in the atmosphere, which is called the active area (see Figure 5.4), is substantially larger in the case of convergent mode. The convergent mode observations permit to have on average more triggered telescopes per event for the recorded data than the parallel mode. Moreover, in the convergent mode, the centers of gravity of the images in the peripheral telescopes are shifted towards the camera center. That gives

[5] q_0^{DMC} corresponds to the actual setting of the threshold for the DMC, while q_0 is the value of the threshold converted from mV to ph.e..

[6] Note that, if a PMT current is relatively high due to a presence of a bright star in the field of view, this PMT is automatically switched off.

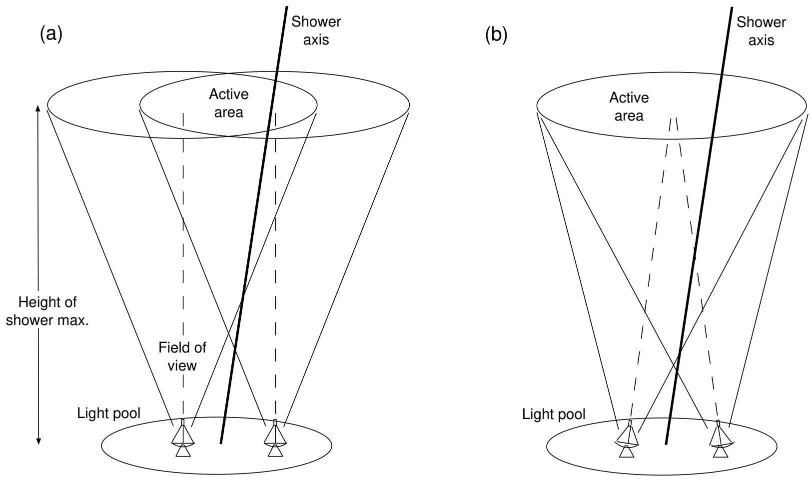

Figure 5.4: *Schematic view of the parallel (a) and convergent (b) modes for two telescopes. In the convergent observation mode the optical axes of the telescopes intersect at the height of the maximum atmospheric shower development.*

Table 5.2: *Summary of the Crab Nebula data taken with the HEGRA system of IACTs in the topological trigger mode and in convergent mode.*

Mode:	No. of runs	T_{OBS} [hrs]	Z.A.	System rate [Hz]
ON	27	8.7	$6° \div 30°$	~ 1.5
OFF	20	6.1	$6° \div 30°$	~ 1.5

significantly fewer events with truncated images at the edge of the camera and permits an easier selection of the active trigger areas (see Figure 5.5).

The Crab Nebula was observed with the topological trigger mode as described above for a total of 8.7 hours in ON viewing mode and for about 6.1 in OFF viewing mode. Finally, a central area of 37 pixels was selected for each telescope camera, with the trigger condition of *2NN/37*. The use of 37 pixels instead of the optimal number of 19 derived through the MC simulations was motivated by the uncertainty in the tilting angle of the system telescopes in the convergent mode. Indeed, even a small displacement of a narrow trigger zone composed of 19 pixels with respect to the anticipated angular area of the γ-rays images for a certain tilting angle of $0.6°$, will

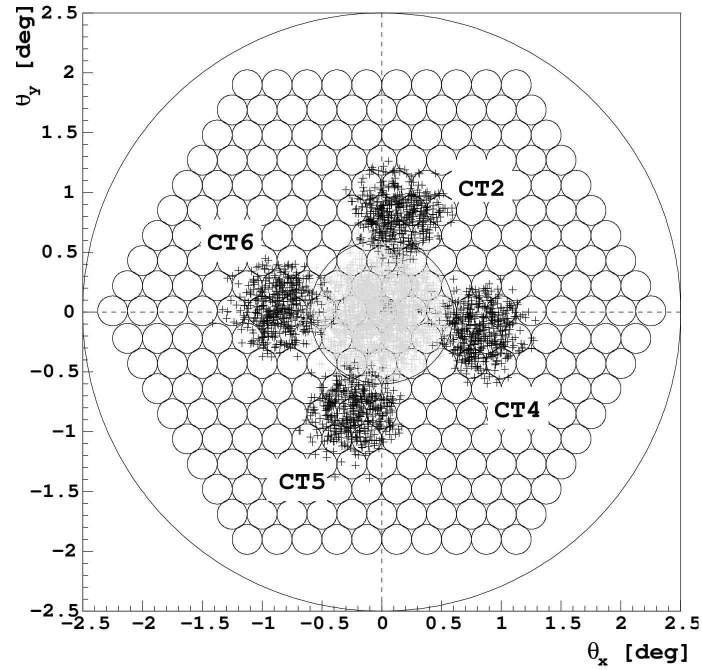

Figure 5.5: *Two-dimensional distribution of the centroid positions for γ-ray images, triggering at least 4 telescopes of the HEGRA IACTs array and passing the selection of the impact distance from the center of the system less than 50 m (black points). Events from MC simulations of vertical showers. CT3 is not shown. In convergent mode the centers of gravity shift towards the camera center (grey points).*

lead to a drastic drop in the γ-ray rate. That becomes less important for a broader trigger zone of 37 pixels. Table 5.2 summarizes the data and the corresponding rates.

5.6 Data analysis

A number of checks have been performed in order to verify the γ-ray signal from the Crab Nebula observed with the HEGRA system of IACTs using the *topological* trigger mode. First, to demonstrate the effectiveness of the trigger, we have compared the distributions of the measured image SIZE parameter for the standard data taking mode and the topological trigger mode. As it possible to see from Fig. 5.6 (a), the content of low energy events (i.e., with lower SIZE) is more prominent for the topological trigger. We also have compared the SIZE parameter distributions for data

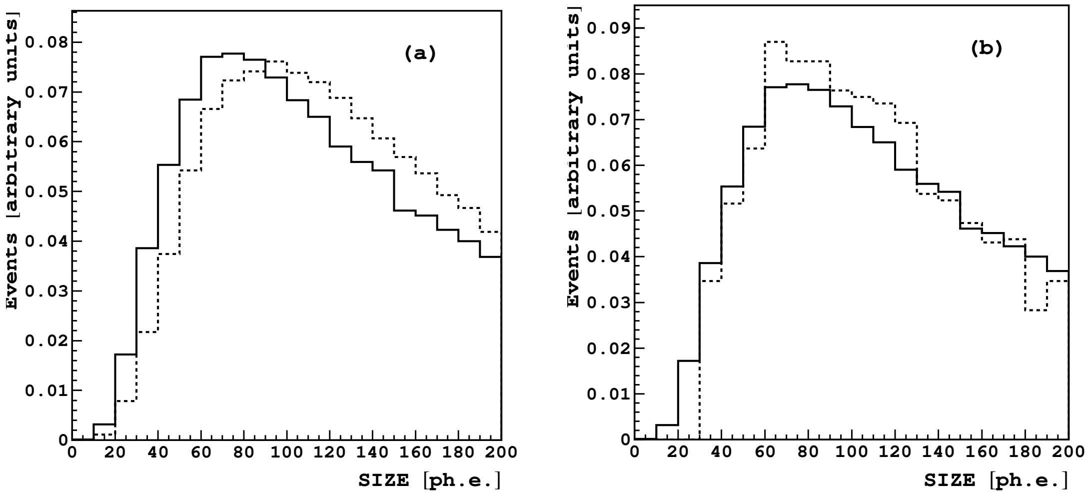

Figure 5.6: *(a): Distribution of the image SIZE parameter for data taken using the topological trigger (solid line) and normal mode (dashed line). (b): Distribution of the image SIZE parameter from data (solid line) and MC simulations (dashed line).*

and Monte Carlo events (see Figure 5.6 (b)), finding a good agreement between the two distributions.

Figure 5.7 shows the distribution of the parameter $\langle W \rangle$ for all recorded excess events, after applying the directional cut $\theta^2 < 0.05\,[\mathrm{deg}^2]$. The distribution of excess events peaks at $\langle W \rangle = 0.12°$ and well reproduces the γ-rays distribution derived from the Monte Carlo simulations (see for comparison Figure 5.3).

Table 5.3 summarizes the event statistics after applying the directional and image shape cuts. The cut on $\langle W \rangle < 0.12°$ corresponds to the optimal cut (where the maximum significance is achieved) as predicted by the Monte Carlo simulations. Note that the signal-to-noise ratio (S/N) given in Table 5.3 was calculated by using the formula of Eqn.(17) from [77], which takes into account a difference in the exposure times between ON and OFF, whereas the final estimate of the system signal-to-noise ratio, derived from Monte Carlo simulations (Eqn. 4.4), was obtained assuming the same observational time in ON and OFF modes. For the data presented here, the OFF observational time is by a factor of 1.4 less than the corresponding time for the ON data sample. That explains why the signal-to-noise ratio derived from the real data is slightly lower than that one estimate using Eqn. 4.4. The γ-ray acceptance, κ_γ, reported in Table 5.3 was calculated from the real data comparing the number

Table 5.3: *Acceptances and corresponding significances after applying the directional and image shape cuts to the Crab Nebula data sample taken in the topological trigger mode.*

Cuts:	ON	OFF	S/N	S/N/$\sqrt{hr}$	κ_γ
$\theta^2 < 0.1$; $\langle W \rangle < 0.15$	752	430	3.24	1.1	0.9
$\theta^2 < 0.05$; $\langle W \rangle < 0.12$	226	72	6.1	2.1	0.53

of excess events before the angular cut (or a very loose angular cut) with the excess events after the application of the orientational cut $\theta^2 < 0.05$ [deg^2].

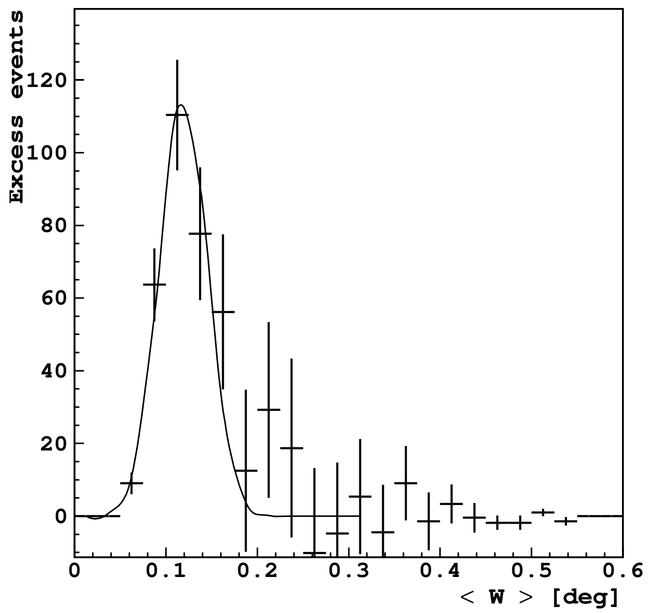

Figure 5.7: *Distribution of the excess events, detected from the direction of the Crab Nebula using the topological trigger, over the mean WIDTH parameter.*

5.7 Energy threshold and flux estimation

As we have seen in the previous chapter (§ 4), the stereoscopic system permits a straightforward measurement of the shower energy, based on the reconstructed impact distance and the measured SIZE of an image. For the spectrum studies it is advisable to use a maximal γ-ray acceptance and, consequently, minimize the systematic error related to the cut efficiency. Here the following cuts were used: $\langle W \rangle < 0.15°$ and $\theta^2 < 0.05\,[\mathrm{deg}^2]$. The distribution of the γ-rays-candidate excess events detected from the Crab Nebula direction using the topological trigger over the reconstructed energy is shown in Figure 5.8. The same energy reconstruction routine was used for the Crab Nebula data taken in the standard trigger mode. It is clear that there is a substantial

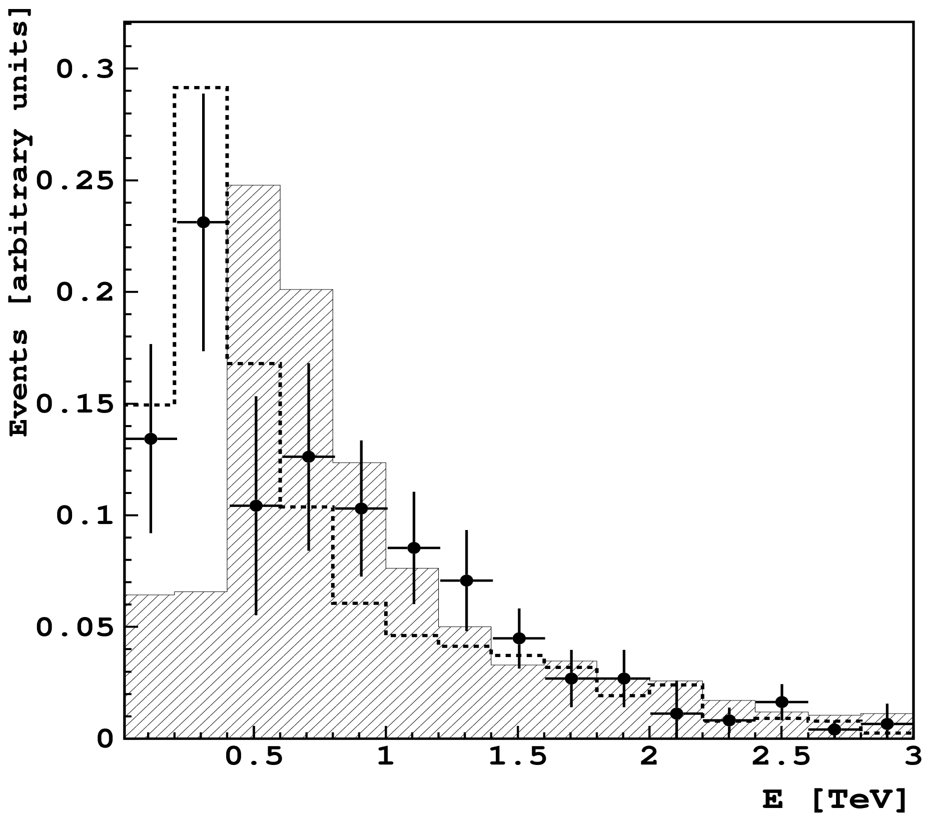

Figure 5.8: *The energy distribution for the γ-ray events detected from the Crab Nebula, from the data taken in topological trigger mode (black dots) and standard data taking mode (fill hatched histogram). Also superimposed is the MC prediction (dashed line) for the topological trigger mode.*

Table 5.4: *Energy resolution for the data taken towards the direction of the Crab Nebula using the topological trigger.*

Energy [TeV]	0.3	0.5	1.
$\Delta E/E$	$\sim 40\%$	$\sim 31\%$	$\sim 20\%$

shift of around 40% in the peak of the energy distribution (which corresponds to the maximum γ-ray rate) derived from the topological trigger with respect to that one obtained with the standard observational mode. Both data samples correspond to similar range of zenith angles. For the *topological* trigger mode, the position of the peak is between 200-400 GeV. As it is seen in Figure 5.8, half of the excess events are below the actual HEGRA energy threshold ($\sim$ 500 GeV).

The energy resolutions estimated from the data taken towards the direction of the Crab Nebula using the topological trigger are shown in Table 5.4.

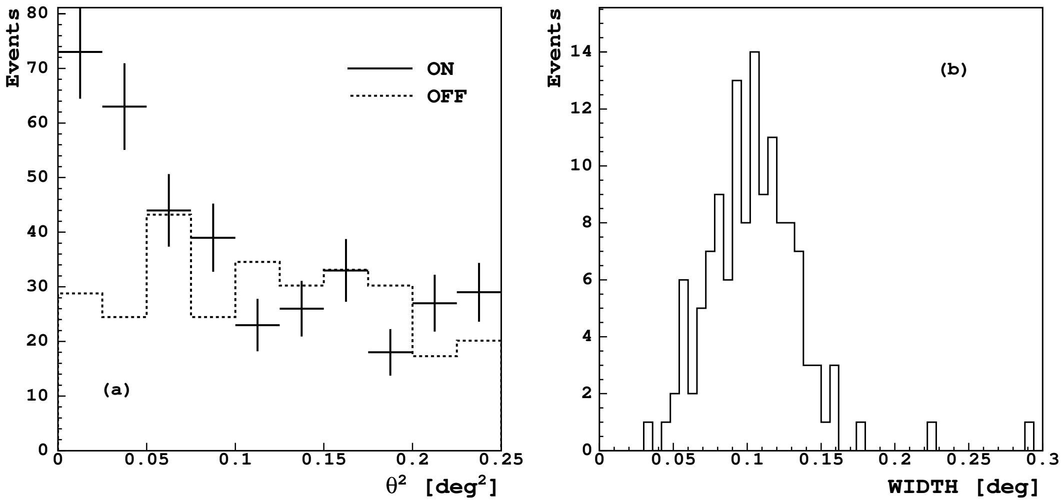

Figure 5.9: *(a): Squared angular distance θ^2 of the reconstructed event directions from the Crab direction with reconstructed energies below 500 GeV (image shape cut: $\langle W \rangle < 0.12°$). The OFF data have been scaled by a factor* $\mathrm{T_{ON}/T_{OFF}} = 1.4$ *(b): WIDTH distribution for events detected by CT3 with estimated energies $E <$* 500 *GeV.*

Fig. 5.9 (a) and (b) show, respectively, the distribution of the squared angu-

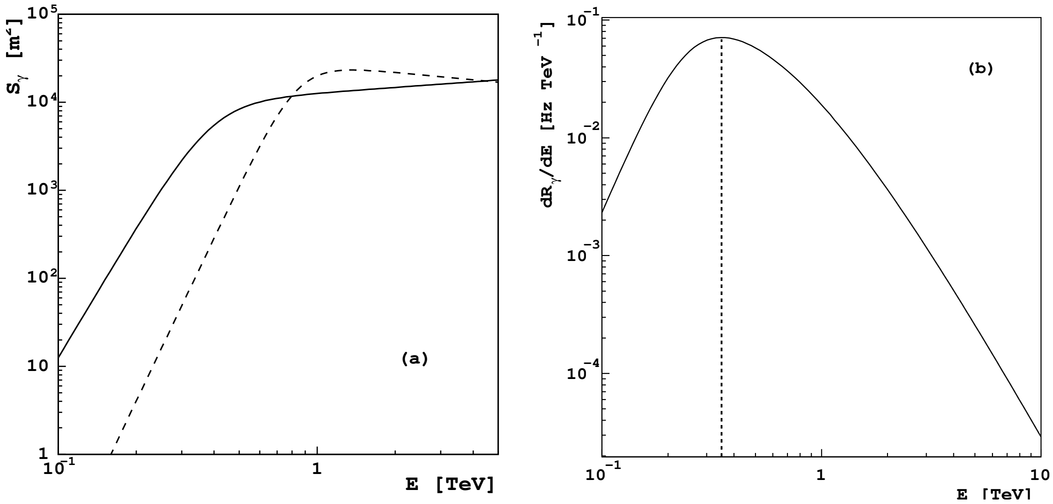

Figure 5.10: *(a) Detection areas calculated for a trigger threshold of 8 ph.e. (dashed line) and 4 ph.e. (solid line). Simulations are for ZA=20° and for the topological trigger, with >= 4/5 telescopes triggered in convergent mode. (b) Differential trigger rates for the HEGRA IACTs system in the topological trigger mode: the corresponding energy threshold (peak of the curve) is* $E_{th} \simeq 350\ GeV$.

lar distance of the reconstructed events from the source direction and the WIDTH parameter, for those events with reconstructed energies below the nominal energy threshold of the detector.

In order to calculate the new energy threshold as the peak of the differential trigger rates (§ 4.7), we make use of the collection area calculated through the MC simulations for the system in *topological* trigger configuration, with a trigger multiplicity of $n_{tel} \geq 4/5$ and a local trigger threshold of $q_0 = 4$ ph.e.. We also have made use of the Crab Nebula spectrum as measured by the HEGRA system of IACTs above 500 GeV [60].

Figure 5.10 (a) shows the effective areas determined in the *topological* observation mode for the same trigger multiplicity but for two different local trigger threshold: $q_0 = 8$ ph.e. and $q_0 = 4$ ph.e. As we expect, the collection area for the lower local trigger threshold is shifted towards lower energies.

Figure 5.10 (b) shows the differential trigger rates for the HEGRA IACTs system in the topological trigger mode calculated using the effective area for $q_0 = 4$ ph.e. The energy threshold for this observation mode (the peak of the curve of Fig. 5.10 (b)) occurs at $E_{th} \simeq 350$ GeV, about a 30% lower than the nominal value (see § 3.3).

In order to estimate the integral γ-ray flux above the energy threshold obtained using the *topological trigger*, we will make use of the spectral index of the Crab Nebula power law spectrum as measured by the HEGRA system of IACTs above 500 GeV [60], which also takes into account the flattening towards low energies, leaving the flux normalization factor free:

$$dJ_\gamma/dE = C(E/1\ \mathrm{TeV})^{-2.47-0.11\log(\mathrm{E})}\ \mathrm{ph\ cm^{-2}s^{-1}TeV^{-1}} \tag{5.4}$$

From such spectrum, it is possible to derive the total number of expected low energy γ-rays:

$$\tilde{N}_\gamma = \int_{E_o}^{E_1} (dJ_\gamma/dE) S_\gamma(E) k_\gamma(E) dE \tag{5.5}$$

where S_γ and k_γ are the collection area and the γ-ray acceptance after the cuts, respectively.

In the calculation of the integral flux, we have assumed the boundaries of the integration as $E_0 = 0$ TeV and $E_1 = \infty$. By comparing the actual number of recorded γ-ray events, N_γ, with the expected number, $\tilde{N}_\gamma$, one can estimate the integral Crab Nebula γ-ray flux as:

$$J_\gamma(> E_{th}) = (N_\gamma/\tilde{N}_\gamma) \int_{E_{th}}^{E_1} (dJ_\gamma/dE) dE\ , \tag{5.6}$$

where $E_{th} = 350$ GeV. For the loose analysis cuts used here, the total number of registered γ-ray events amounts to N_γ=260. Thus, the estimated γ-ray flux from the Crab Nebula is

$$J_\gamma(E > 350\ GeV) = (8.1 \pm 0.1 \pm 0.2) \times 10^{-11}\ \mathrm{ph\ cm^{-2}\ s^{-1}} \tag{5.7}$$

where the estimated statistical and systematic errors are also shown. The relative variation $\Delta J/J$ of the integral flux due to possible changes in the spectral index is of about 6%, while the relative error on the energy estimation is 15%.

The estimate γ-ray integral flux above 350 GeV derived here is consistent with the measurements made by the STACEE, CELESTE, WHIPPLE and CAT groups (see Figure 5.11). As it is shown in Figure 5.11, this estimate is also consistent with an Inverse Compton model of the TeV γ-ray emission.

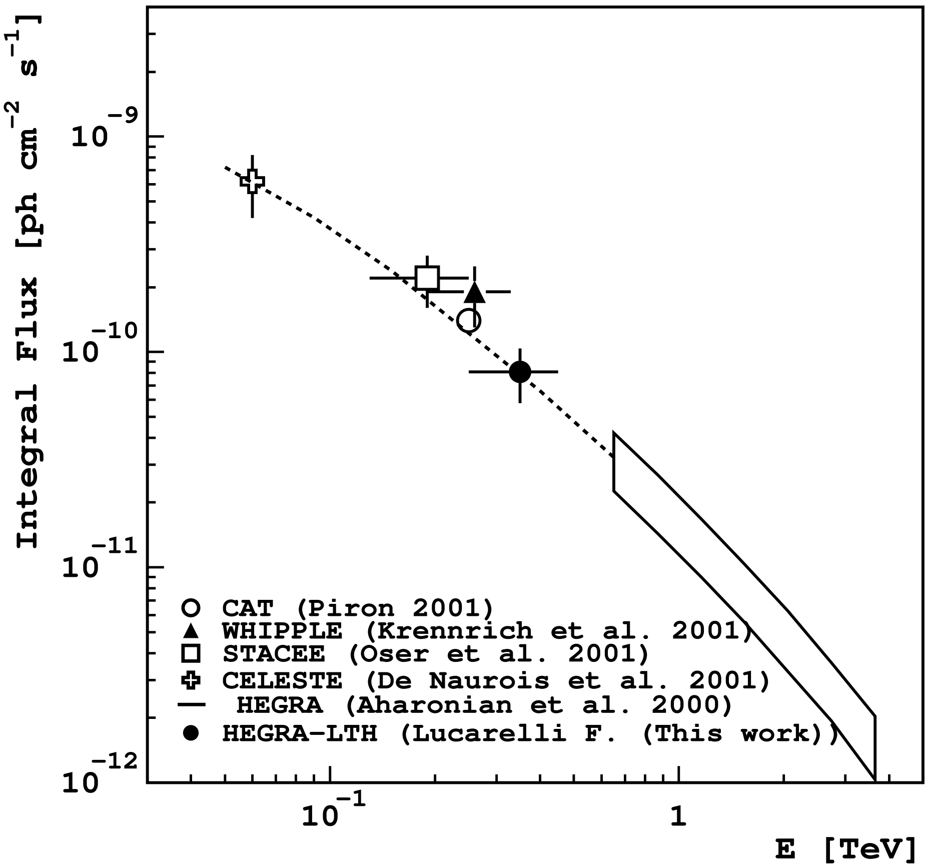

Figure 5.11: *The integral flux of γ-rays with $E > 350$ GeV from the Crab Nebula measured with the HEGRA IACTs array using the topological trigger (black dot). For comparison, are also shown the measurements from other experiments and the upper and lower limits of the systematic error estimated for the HEGRA data taken in the standard configuration (at energies $E > 500$ GeV). The Whipple data point at 260 GeV was derived by integrating the spectrum give in [72] for $E > 260$ GeV, assuming a 30% systematic error. Dashed curve shows an extrapolation at low energies of the Crab Nebula spectrum as measured by HEGRA which also takes into account the flattening in the spectrum slope towards low energies (see Eq. 5.4 and [60]).*

5.8 Possible applications of the topological trigger

The observations of the Crab Nebula with the HEGRA system of IACTs in the *topological trigger* mode have demonstrated for the first time that it is possible to lower the actual energy threshold of the system by a 30% without major hardware changes allowing, at the same time, to keep the event rate at a sustainable level for the currently used DAQ.

In order to check the performance of the system in such an observational mode we have taken 15 hrs of Crab data with the HEGRA IACTs system applying the *topological trigger* and reducing the local telescope trigger threshold to 4 ph.e. (requiring as well at least 4/5 telescopes in coincidence). The estimate γ-ray integral flux from the Crab Nebula above 350 GeV is consistent with previous measurements made by the STACEE, CELESTE, WHIPPLE and CAT groups, and may be further interpreted as Inverse Compton TeV emission coming from the plerion in the Crab Nebula.

This technique could be applied in the near future in the observations with the forthcoming stereoscopic systems (HESS [48], VERITAS [50] and CANGAROO [51]), particularly to search for sub-TeV γ-ray emission from pulsars [78]. By means of a topological trigger, it is possible to achieve a significant reduction of the energy threshold and that gives a considerable advantage in such observations, due to the very steep energy spectrum of the GeV-TeV pulsed emission, which was confirmed by the EGRET observations in the GeV energy range from a number of such objects.

It might be also valuable to apply such technique in search for *BL Lac objects at rather large red shifts*, which are expected to have a very steep energy spectrum due to the IR absorption of VHE γ-rays onto the extra-galactic background light (see § 1.4).

Chapter 6

Monte Carlo studies on the sensitivity of the HEGRA IACTs system in observations of extended γ-ray sources

6.1 Introduction

As the main goal of this thesis is the observation of a potential extended source of γ-rays, we have investigated by means of Monte Carlo simulations the sensitivity of the HEGRA system of five IACTs in observations of extended γ-ray emission over the entire field of view of the instrument [52].

For γ-ray point sources, the sensitivity of the imaging atmospheric Čerenkov technique substantially relies on the angular resolution of the instrument. A good angular resolution significantly reduces the background contamination induced by the isotropic cosmic rays. Nevertheless, the present methods of cosmic ray rejection based on the image shape analysis are still not sufficiently effective to reduce entirely the background of hadronic air showers.

As we said previously (§ 4), the observations of γ-ray showers with a single IAC telescope do not allow a complete geometrical reconstruction of the shower axis in space, bringing to a low angular resolution unless a very fine pixellation camera is used. A substantial improvement of the angular resolution was achieved by the HEGRA collaboration using the stereoscopic system of five IACTs with a rather coarse camera pixellation. The stereoscopic observations with such a system allow to reach (for good quality data) an angular resolution for an individual γ-ray as good as $0.06°$ [85].

The HEGRA system of IACTs has proved to be a very effective tool to search for TeV γ-ray emission and to study the energy spectra of point-like sources which are well established in observations at other wavelengths. The rich HEGRA data sample of γ-rays from the Crab Nebula [60], Mkn 501 [61] and Mkn 421 [62] allowed to measure with great precision this angular resolution, which is in a good agreement with the predictions based on the Monte Carlo simulations (see for details [53]). Such angular resolution allowed to perform a systematic search for point-like γ-ray sources at the flux level of 10^{-11} erg cm^{-2} s^{-1}. This high sensitivity was confirmed by the detection of a very faint γ-ray source, the SNR Cas A, which steadily emits γ-rays at the flux level of about $5.9 \cdot 10^{-13}$ ph cm^{-2} s^{-1} above 1 TeV [18].

However, for a certain number of important tasks, e.g. *(i)* to search for γ-ray emitters with poorly known position (like the EGRET unidentified sources), *(ii)* to perform sky surveys, *(iii)* to study extended γ-ray emission from SNRs, *(iv)* to investigate diffuse emission from the Galactic plane, and finally, *(v)* to detect the primordial γ-ray bursts, the potential γ-ray source may appear anywhere within the entire field of view (FoV) of the instrument, or may have a rather large angular size as compared to the angular resolution of the instrument. In the following, we will investigate the sensitivity in detecting γ-ray emission with the HEGRA system of IACTs in observations of this type.

6.2 Simulations

In order to study the sensitivity of the HEGRA IACTs system in observation of extended γ-rays sources (i.e., for γ-rays coming off the telescope optical axis), we have performed Monte Carlo simulations of diffuse γ-rays as well as isotropic cosmic rays. The simulations have been done using a two-step procedure, which was described in detail in [53]. In the first step, the showers of primary γ-rays and protons were gene-

Table 6.1: *Summary of the sample of Monte Carlo simulated showers.*

Primary:	Z.A. [deg]	No. events	Energy [TeV]
γ	0	33239	0.1 - 30
	20	106810	0.4 - 30
	30	96729	0.4 - 30
	45	74641	0.4 - 30
p	0	21119	0.2 - 50
	20	30153	0.2 - 50
	30	41717	0.3 - 100
	45	29028	0.3 - 100

rated in the atmosphere using the ALTAI Monte Carlo code [41]. The showers were randomized over a maximum impact distance of 250 m. with respect to the center of the telescope array. The major parameters of the samples of simulated showers are summarized in Table 6.1. The simulations have been done for different zenith angles, covering the range of angles usually used in observations of extended sources with the HEGRA IACTs system. In the second step, the response of the telescope camera was simulated for all previously generated showers, taking into account all the typical efficiencies characterizing a Čerenkov light detector (see for details [86]). Furthermore, an additional randomization of the images within a solid angle around the telescope axis with half opening angle of 4.0° was introduced in order to simulate the isotropic flux of proton showers and diffuse γ-rays.

Different parameters of the simulated cosmic ray- as well as γ-ray-induced atmospheric showers were compared to the data in order to check the consistency of the MC simulations (see [53, 87, 88, 89]).

6.3 Analysis

6.3.1 Detection rate over the FoV

The counting rate of isotropically distributed cosmic rays and diffuse γ-rays after application of image shape cuts, $\tilde{R}_{(\gamma,cr)}$ [Hz sr^{-1}], is defined as

$$\tilde{R}_{(\gamma,cr)}(\Theta) = R_{(\gamma,cr)}(\Theta)\kappa_{(\gamma,cr)}(\Theta) \ , \tag{6.1}$$

where $R_{(\gamma,cr)}$ is the counting rate of cosmic rays or γ-rays before the cuts, $\kappa_{(\gamma,cr)}$ is the acceptance after applying the shape cuts and Θ is the angular distance from the center of the FoV. The initial event counting rate $R_{(\gamma,cr)}$ can be calculated as

$$R_{(\gamma,cr)}(\Theta) = N_{(\gamma,cr)}\Delta t^{-1}\Delta\Omega^{-1}, \tag{6.2}$$

where $N_{(\gamma,cr)}$ is the number of registered events during a time interval Δt within the solid angle $\Delta\Omega$, which is usually chosen to reflect the angular resolution of the instrument. In the calculations we have used the CR energy spectrum as given in [91].

For diffuse and extended γ-ray sources there is no direct correlation between the core distance of a shower and the location of the image center of gravity (centroid) position in the FoV. Showers detected at the same impact distance but of different inclinations with respect to the telescope axis could produce an image positioned anywhere in the FoV, which is limited by the angular size of the telescope imaging camera.

The calculated γ-ray detection rate, R_γ, as a function of the angular distance from the telescope axis is shown in Figure 6.1 for different trigger multiplicities. As it possible to see, the detection rate is approximately constant up to $\Theta \simeq 1^\circ$ (within 10%) from the center of FoV and decreases rather sharply beyond that region. For higher trigger multiplicities the fall-off in the detection rate starts at smaller angular distance from the telescope axis.

This rather sharp decrease can be explained as follows. In a *toy model*, we can assume that most of the detected γ-ray showers have an impact distance around $R_o \simeq 120$ m (e.g. see [93]). The γ-ray-induced atmospheric showers, with a primary energy above the energy threshold of the instrument ($E > 500$ GeV) and shower axes

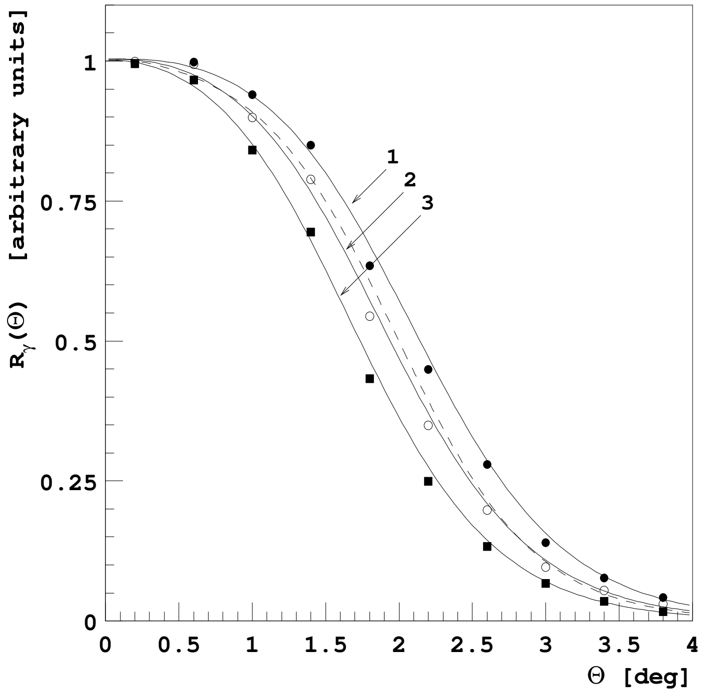

Figure 6.1: *Detection rate of the isotropically distributed γ-rays and cosmic rays calculated for the HEGRA system of IACTs. Solid curves are for the γ-rays. Curves 1, 2, and 3 correspond to the trigger multiplicity $n_{tel} \geq 2/5$, $n_{tel} \geq 3/5$, and $n_{tel} \geq 4/5$, respectively. The symbols correspond to the Monte Carlo data points used in the fits. Dashed curve shows the rate of the cosmic ray showers for the trigger multiplicity of 2. Detection rates are normalized to 1 at the center of FoV. The rates were calculated after applying the quality cuts DIST $< 1.8^\circ$ and image SIZE >40 photoelectrons.*

directed along the joint optical axis of the system telescopes, will produce Čerenkov light images with centroid positions shifted from the camera center by approximately $\Theta_o \simeq 1^\circ$. Those images are well within the effective radius of the HEGRA cameras of 2.15° (see Fig. 6.2 (a)). Instead, the diffuse γ-rays coming at an inclination angle of about $\Theta_s \geq 1.1^\circ$ with respect to the telescope axis, will be often truncated by the camera edge (see Fig. 6.2 (b)) and they can distort the stereo reconstruction. However, these images can be removed from the analysis applying a cut on the angular distance (the image parameter DIST (see § 3.2)) of the image centroid to the camera center[1].

[1]Hereafter, we will use a cut on DIST$< 1.8^\circ$.

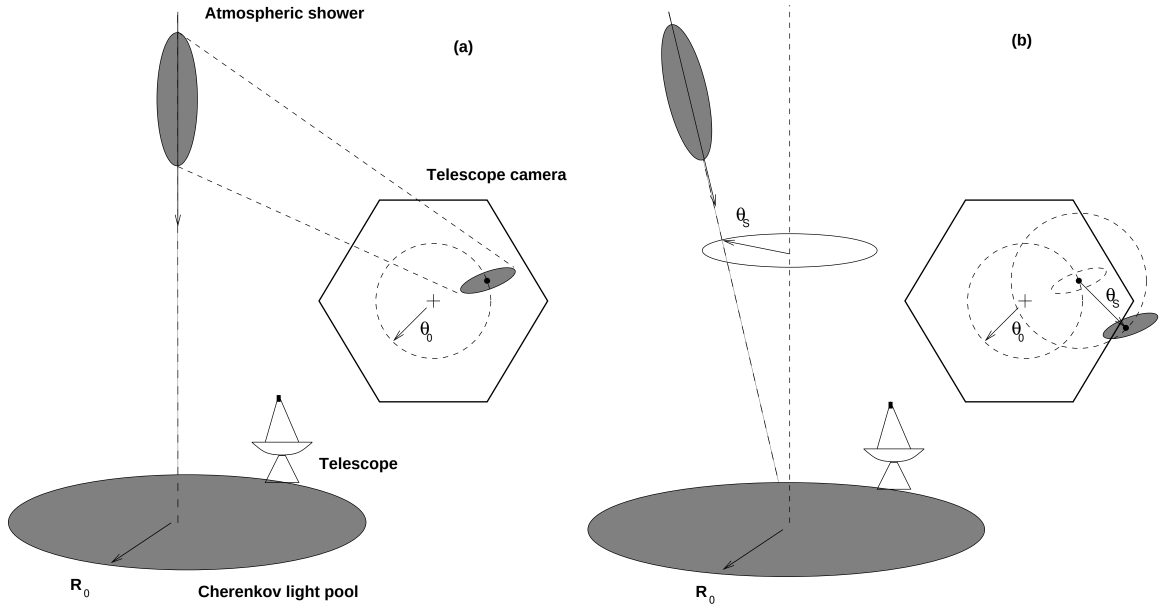

Figure 6.2: *Scheme of the image displacement in the camera focal plane.*

Indeed, as it is shown in Fig. 6.3, it is the application of this cut which creates the effect of the fall-off in the detection rate within the physical dimensions of the PMTs camera.

On cutting on DIST< $1.7^\circ - 1.8^\circ$, we can expect a rather stable γ-ray rate, $R_{(\gamma,cr)}(\Theta)$, up to $\Theta \simeq 1^\circ - 1.1^\circ$. Note that by increasing the energy of the detected γ-ray showers the effective impact distance increases as well and consequently the effect of the camera edge shows up at smaller shower inclinations.

The detection rate as a function of the angular distance from the center of FoV can be well fitted by the function

$$R_{(\gamma,cr)}(\Theta) = \mathrm{a}_0 \cdot (1+\Theta)^{\mathrm{a}_1}[1+\exp(\mathrm{a}_2 \cdot (\Theta - \mathrm{a}_3))]^{-1}. \tag{6.3}$$

which has been used for the fit of the MC points showed in Fig. 6.1.

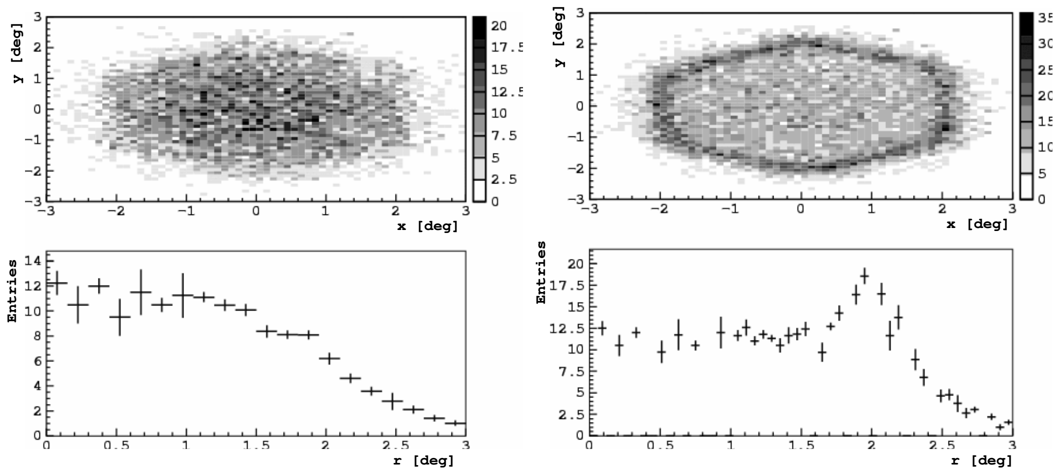

Figure 6.3: *Reconstructed events of the HEGRA IACTs system calculated from a sample of real data vs distance from camera center, after applying a cut on DIST* < 1.8 *(left panel) and without applying any cut on DIST (right panel). In the right panel it is clearly visible the accumulation of images at the camera border. Trigger multiplicity: ntel ≥2/5.*

Table 6.2: *Angular resolutions for individual off-axis γ-ray-induced atmospheric showers ($\Delta\theta$ defines a 68% error circle around the actual source position). Trigger multiplicity:* $n_{tel} \geq 3/5$.

Θ [deg]	0.5	1.0	1.5	2.0	2.5	3.0
$\Delta\theta$ [deg]	0.12	0.12	0.14	0.16	0.17	0.31

6.3.2 Angular resolution over the FoV

We have seen in Chapter 4.5.2 that the angular resolution of the IACTs array heavily relies on the accuracy in the reconstruction of the image major axis (only for central point-like sources), which in turn depends mainly on the image size and the distance of the shower axis to the center of the array (core distance), and it improves noticeably with the increasing shower energy and with higher trigger multiplicities [53].

The angular resolutions for a γ-ray point-like source placed at different angular distances from the center of FoV are illustrated in Figure 6.4 and Table 6.2. As it possible to see, the geometrical reconstruction of the shower arrival direction works

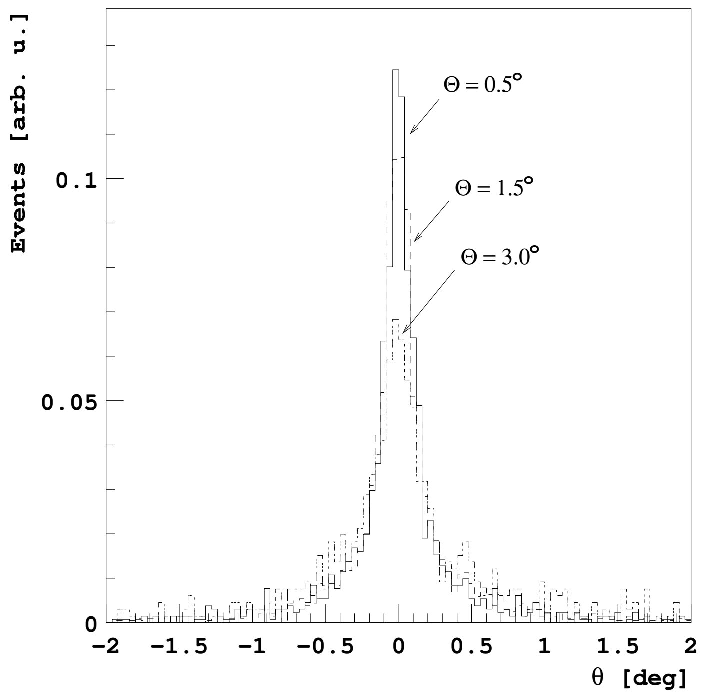

Figure 6.4: *The angular resolutions of off-axis γ-ray showers detected with the HEGRA system of IACTs for three angular distances from the center of FoV. At least three Čerenkov images were used for the reconstruction of the shower arriving direction.*

very well also for slightly inclined γ-ray showers, and the angular resolution almost does not depend on the angle Θ within the range of $\Theta \leq 1.5^\circ$. Beyond that region the images detected with the telescope system are often truncated by the camera edge, which worsens the angular reconstruction. For a precise measurements of the angular extension of an extended γ-ray source, one should take into account the actual angular resolution at a certain angular distance from the center of FoV and perform a deconvolution to obtain the measured angular extension of the source.

6.3.3 Rejection of cosmic rays over the FoV

Apart from the excellent angular resolution, the system of IACTs offers the ability to reject cosmic ray showers using the shape of the Čerenkov light images registered in a number of telescopes (see § 4.6).

Table 6.3: *Acceptances of γ-ray- and cosmic ray-induced atmospheric showers after applying a mean scaled WIDTH cut of 1.1 for different angular distances from the center of FoV and trigger multiplicities.*

Trigger:	Θ [deg]	0.5	1.0	1.5	2.0	2.5	3.0
2/5	k_γ	0.67	0.68	0.69	0.62	0.58	0.41
3/5	k_γ	0.66	0.67	0.68	0.62	0.55	0.34
4/5	k_γ	0.65	0.65	0.66	0.60	0.50	0.21
2/5	k_{CR}	0.06	0.06	0.06	0.06	0.07	0.08
3/5	k_{CR}	0.04	0.04	0.04	0.04	0.05	0.07
4/5	k_{CR}	0.03	0.03	0.03	0.04	0.06	0.08

The *mean scaled WIDTH (mscw)* parameter, $\langle \tilde{w} \rangle$ (§ 4.6), has proven to be a very effective tool in rejection of a substantial fraction of CR showers. As we have seen in § 4.6, for central point-like γ-ray sources applying a cut on $\langle \tilde{w} \rangle < 1.1$ provides, for a system trigger multiplicity of at least 3 out of 5 telescopes, a 68% acceptance of γ-rays while reducing the CR contamination by a factor of 25, corresponding to an enhancement of the γ-ray sample (Q-factor $= k_\gamma k_{CR}^{-1/2}$) of 3.4.

Here we study how the cut on *mscw* works for off-axis γ-rays. The calculations have been done for six bands of 0.2° size each, placed at the angular distances of 0.5°, 1°, 1.5°, 2.0°, 2.5° and 3.0° from the center of the FoV. The *mscw* distributions for γ-ray showers within three of those angular bands are compared in Figure 6.5. When increasing the inclination angle of the shower relative to the telescope axis, the distributions remain peaked at 1 but develop a tail towards larger *mscw* values. The acceptances of γ-rays after applying the cut on *mscw* are almost identical for those bands (see Table 6.3). Thus, we may conclude that the shape of the images for inclined γ-ray showers coming off the telescope optical axis at angles less than $\simeq 1.5°$ are still not noticeable affected by the telescope camera edge. From Table 6.3 it is possible to note a slight decrease in the γ-ray acceptance, k_γ, towards larger displacements from the center of FoV, which can be related to the effect of the camera edge. For CR showers with isotropically distributed arrival directions, the acceptance after applying the image shape cut (k_{cr}) also does not depend on the angular distance within the

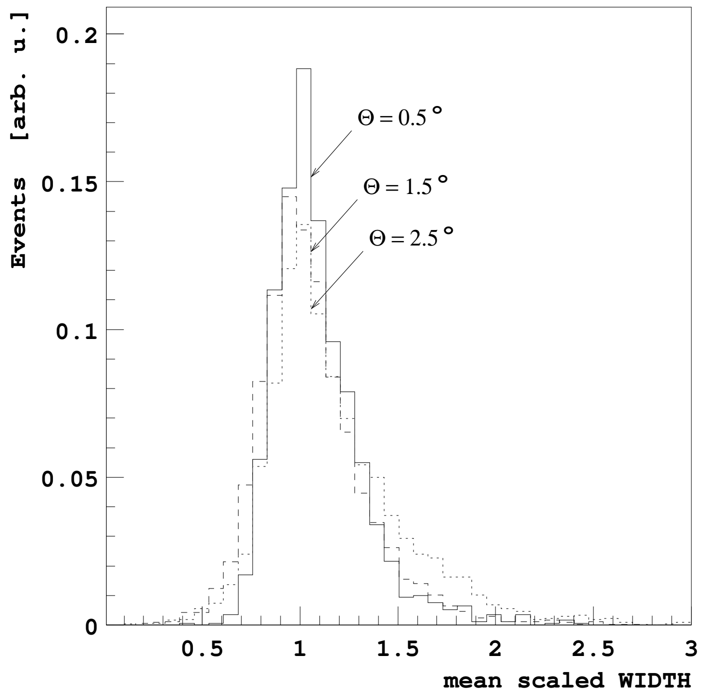

Figure 6.5: *The distribution of the mscw parameter for samples of γ-rays at three inclination angles with respect to the telescope optical axis. Events with at least 2 images were used in analysis.*

range of $\Theta \leq 2^{\circ}$, whereas it slightly increases towards larger angular distances.

6.4 Simulations vs Data

The MC simulations of diffuse γ-rays can be verified by the observations of the Crab Nebula, which has been extensively observed in *wobble mode* (see § 4.6). Assuming in the simulations the Crab Nebula flux and spectrum as it was measured by the HEGRA collaboration [60], it is possible to calculate the corresponding γ-ray rate at the angular distance of $\pm 0.5^{\circ}$ from the center of FoV. The results for different trigger multiplicities are summarized in Table 6.4 [92]. The Monte Carlo simulations well reproduce the relative rates for the 2, 3, and 4 telescope coincidences. Note that a possible systematic error in the Monte Carlo simulated rates is estimated to be less than 10%.

Table 6.4: *The calculated and measured Crab Nebula detection rate,* R_γ [ph Hz^{-1}]*, at* $0.5°$ *distance from the center of the FoV.*

Trigger:	2/4	3/4	4/4
Data	18±2	21±3	19±3
Monte Carlo	20	20	22

In Figure 6.6 we compare the distributions of the *mscw* parameter for the γ-ray- and cosmic ray-induced simulated showers with real data. The *mscw* distribution of the real γ-rays was produced using a Crab Nebula data sample. The Monte Carlo distributions fit very well the data. Here, the same Monte Carlo tables reporting the mean *WIDTH* as function of impact distance and image SIZE have been used both for the simulated and the recorded events (see § 4.6). For each individual event, the Monte Carlo tables are interpolated according to the reconstructed impact distance and the measured image size both in the simulations and in the data. The simulations are in very good agreement with the data. The position of the peak of the simulated γ-ray showers agrees with the data within a 3%.

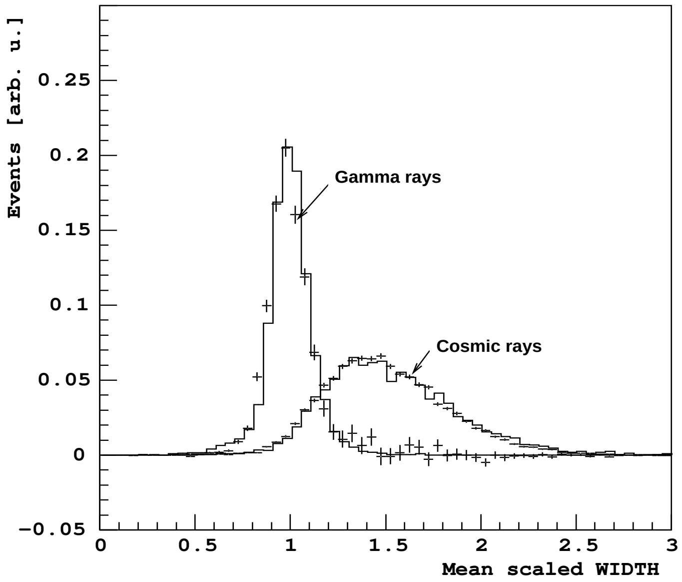

Figure 6.6: *The distributions of the mean scaled WIDTH parameter for MC simulated and real γ-rays and cosmic rays events. Histograms show the Monte Carlo simulations. Crosses represent the HEGRA data taken with a system trigger multiplicity of at least 2 telescopes out of 5. The distributions are normalized to 1 particle. The content of the histogram bins is given in arbitrary units.*

6.5 Sensitivity over FoV

The sensitivity of the HEGRA system over the whole field of view can be estimated using the detection rates and acceptances previously calculated. To parameterize the sensitivity of the instrument one can use the Q-factor $Q_F(\Theta)$ (see § 4.5.2), defined as:

$$Q_F(\Theta) = k_\gamma R_\gamma \cdot [k_{CR} R_{CR}]^{-1/2} \tag{6.4}$$

where the rates of γ-rays and cosmic rays are normalized to 1 at $\Theta = 0$. The results of such calculations are shown in Figure 6.7. One can see that the value of Q-factor is constant up to $\Theta = 1°$. Even though the γ-ray detection rate decreases noticeably beyond that region, the Q-factor at $\Theta = 1.5°$ is only by 5% less than in the central part of the FoV.

Higher telescope multiplicities provide better Q-factors. That is due to the fact that for higher multiplicities the CR rejection substantially increases, even though the

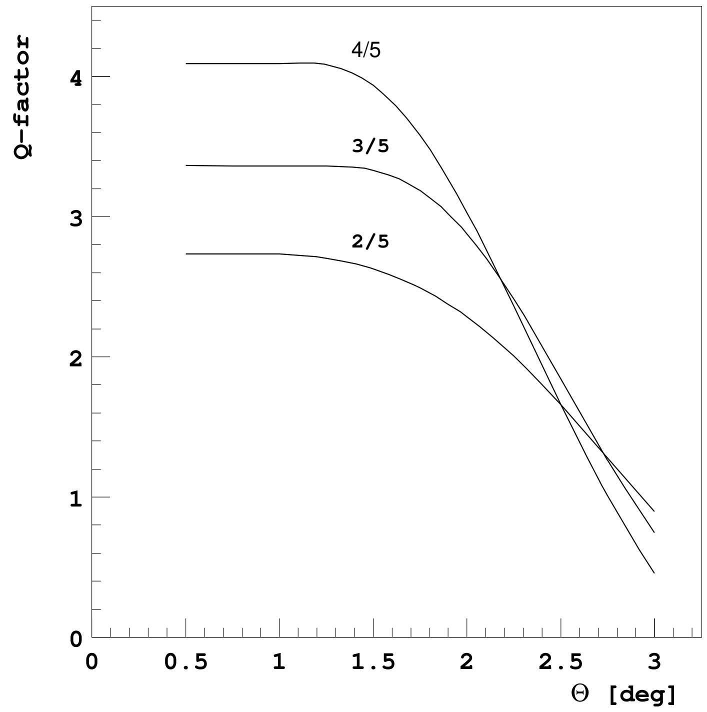

Figure 6.7: *Q-factor (Eq.6.4) calculated at different angular distances from the center of FoV. The corresponding trigger multiplicities are shown.*

detection rate of γ-rays sharply decreases at larger angular distances from the center of the camera. This sharp decrease ultimately makes less effective the observations with higher telescope multiplicities. Remind that the angular resolution is almost constant up to the angular distance of 1° from the camera center.

6.6 Sensitivity to extended γ-ray sources

Based on the detailed Monte Carlo simulations for the HEGRA system we have estimated the sensitivity of the instrument in observations of extended γ-ray sources. The results of the simulations could be interpreted using the established sensitivity for a point-like γ-ray source. The resulting signal-to-noise ratio for a γ-ray source of an arbitrary angular size θ, can be calculated as:

$$S/N = \tilde{R}_\gamma/[\tilde{R}_{CR} \cdot (\theta/\theta_0)^2]^{1/2} T_{obs}^{1/2} = \tilde{R}_\gamma/[\tilde{R}_{CR}]^{1/2} \cdot (\theta/\theta_0)^{-1} T_{obs}^{1/2} \qquad (6.5)$$

where $\tilde{R}_\gamma$, $\tilde{R}_{CR}$ are the detection rates of γ-rays and cosmic rays, respectively, after applying the analysis cuts. The values θ_0 and θ correspond to the orientational cuts for a point-like source ($\theta_0 = 0.1° - 0.13°$) and an extended γ-ray source (where θ is the source extension), respectively. $\tilde{R}_{CR}$ is the CR rate for a standard orientational cut applied for a point-like source search. Given the isotropic CR background, the total number of background counts for an extended γ-ray source is proportional to the angular area covered by the source ($R_{CR} \propto \theta^2$). For a 5σ detection and a fixed observational time (t=100 hrs)[2], it is possible to calculate the minimum detectable flux from a point-like γ-ray source. For the HEGRA array of 5 IACTs such minimum detectable flux is $F_\gamma^{pt}(\geq 1\ TeV) = 1.1 \cdot 10^{-12}$ ph cm^{-2} s^{-1}. Finally, the minimum detectable flux for an extended γ-ray source is given by

$$F_\gamma^{ext} = F_\gamma^{pt} \cdot (\theta/\theta_0), \tag{6.6}$$

where θ is the angular radius of the source region. Note that for extended γ-ray source of large extension ($\theta > 0.5°$), the integral rates $\tilde{R}_\gamma$, $\tilde{R}_{CR}$ need to be corrected for the fall-off in the camera response function (see Fig. 6.1). For γ-ray sources of large extension ($\theta > 1°$) one has to perform observations preferably in ON/OFF mode, i.e. taking the same amount of OFF and ON data, because almost the entire sensitive area of the detector is covered by the source region. Results of the detailed Monte Carlo simulations may deviate from the estimates given by Eq.(6.6) for γ-ray sources of angular extension substantially larger than 1°.

6.7 Estimation of an extended excess

In search for extended γ-ray sources or diffuse γ-ray emission one can divide the field of view into square bins (or pixels) of size approximately equal to the angular resolution of the system, accumulate ON-source and OFF-source events in those bins according to the stereo-reconstructed shower directions and calculate the significance of the possible excess for each bin. Events are pre-selected according to their image shapes, to reduce the CR background (see § 7.4.3).

[2] For instance, SNR Cas A was observed with the HEGRA system of IACTs for a total exposure time of 250 hrs [18].

An alternative analysis technique make use of a grid with a bin size much smaller than the angular resolution, accumulating for each grid point the ON-source and OFF-source events with directions consistent with a point-like source localized at that grid point [90] (see § 7.4.4); this technique is suitable to search for isolated point-like sources of unknown location all over the available FoV, but has the disadvantage that the significances determined for adjacent grid points are highly correlated, which makes difficult to estimate the overall significance for an extended source. In case when an appropriate model of diffuse γ-ray emission can be easily constructed, one can use likelihood ratio methods to test the hypotheses (see § 6.6). If the expected emission region is relatively small, i.e. less than $0.5°$ in radius, one can use in observations of such sources a *wobble mode* approach (§ 6.4) using the same angular area, taken symmetrically across the center of FoV, for the background estimate (§ 7.4.4).

A further alternative approach to estimate the significance for an extended sources would be to make some assumptions, based on physical arguments, about the position and the extension of the γ-ray source and taken as ON the correspondent sky region and, as OFF, several sky regions of the same shape (if possible) (see § 7.5).

We will apply these techniques in the next chapter, when we analyze the data taken towards the direction of a possible extended source of γ-rays, the Monoceros Loop SNR.

In most of the cases, it is necessary to calculate the detection efficiency versus the radial distance from the center of FoV directly from the data, and, afterwards, apply a flat-fielding in order to compensate for the non-uniform response of the camera at different angular distances. To do that, one can fit the detection rate of the cosmic rays versus the angular shift from the center of FoV and then apply that fit to all angular bins over the entire FoV. Such fit can vary accordingly to the source zenith angle and the night sky background, and can have as well an azimuthal dependency.

Let us now examine two cases separately. If both ON-source and OFF-source data are available [3], after applying the *mscw* cut for the γ/hadron separation, the mean number of counts per each angular bin in ON-source and OFF-source data samples

[3] OFF-source data are usually taken in a sky region sufficiently away from the source and where no γ sources are known to be present.

can be calculated as:

$$\langle N_{(on,off)}\rangle = \frac{1}{M}\sum_{i=1}^{M} N_{(on,off)}(i,\Theta) f^{-1}(\Theta) \tag{6.7}$$

where $N_{(on,off)}(i,\Theta)$ is the number of counts in the i-th bin at a certain distance Θ from the center of the FoV. The function $f(\Theta)$ accounts for the non-constant event rate at different radial distances. M is the total number of bins in the grid. $\langle N_{off}\rangle$ is the mean number of counts per bin placed at the center of the camera FoV in the OFF-source sample. Given this number, one can estimate the background content for each pixel (i) in the ON-source data as

$$N_{off}^{(1)}(i) = \alpha f(\Theta)\langle N_{off}\rangle \tag{6.8}$$

The scaling factor α, which equalizes differences in observational time for ON- and OFF-source samples, as well as possible differences in corresponding zenith angle distributions, can be determined as

$$\alpha = \langle N_{on}\rangle(\langle N_{off}\rangle)^{-1} \ . \tag{6.9}$$

In case only ON-source data are available (more likely), one can use the mean number of counts per bin averaged over all bins in the ON-source data sample, $\langle N_{on}\rangle$[4]. It is assumed here that the γ-rays expected rate is very low and negligible compared with the CR rate. Thus, the mean number of predicted background counts in each angular bin will be given by:

$$N_{off}^{(2)}(i) = \alpha f(\Theta)\langle N_{on}\rangle. \tag{6.10}$$

Here, the scaling factor α is calculated as $\alpha \simeq 1/M$, where M is the total number of bins used in Eqn.6.7.

Finally, the significance for each individual angular bin can be estimated using the Li&Ma's formula [77]:

[4]Note that in observations of extended γ-ray sources with well defined location and extension one can exclude from the averaging loop (Eqn.6.7) those angular bins which are *a priori* covered by the source. However, the source extension has to be significantly smaller than the observational window used.

$$S=\sqrt{2}\left(N_{on}\ ln\left[\frac{1+\alpha}{\alpha}\left(\frac{N_{on}}{N_{on}+N_{off}}\right)\right]+\right.$$
$$\left.N_{off}\ ln\left[(1+\alpha)\left(\frac{N_{off}}{N_{on}+N_{off}}\right)\right]\right)^{1/2}\ . \quad (6.11)$$

If after this procedure some pixels show a significance $\simeq 3.5\sigma$, we can assume that they contain an excess of γ-rays and can exclude them from the calculation of the average number of background counts per bin and recalculate the significances again.

The background model constructed from the ON-source data itself can not be applied for observations of presumably diffuse γ-ray source of large angular size, comparable with the angular size of the entire FoV of the instrument. However, it might be effective in a *discovery* mode while scanning very extended sky regions.

For a positive detection of a quite extended γ-ray source (with size larger than $0.5°$), we can expect that a few contiguous pixels could show a high value of significance. Thus, it could be possible to calculate the confidence level of the excess using the approach suggested by Li&Ma [77] for such a particular case [107]. This approach takes into account that the confidence level of an excess in each bin depends in addition on the total number of bins (*number of trials*) M considered in the division of the FoV, which may be considered as M independent measurements.

After the average background calculation, we can calculate the standard deviation for each pixel from the average background. Naturally, only those pixels which show an excess in the ON data sample (for instance, with $S > 3.5\sigma$, where σ is one standard deviation for the Gaussian distributed background events) might be considered for statistical analysis. The probability p to achieve 3.5σ excess due to fluctuations in background for each individual pixel, can be simply calculated as

$$p=1-\frac{1}{\sqrt{2\pi}}\int_{-\infty}^{3.5}e^{-\frac{1}{2}t^2}dt \quad (6.12)$$

and, eventually, the probability to get k pixels at 3.5 standard deviations from the average within the field of view, will be given by

$$p_k=C_M^k p^k(1-p)^{M-k}\ , \quad (6.13)$$

where C_M^k is the binomial coefficient. The probabilities for different number of excess pixels and M=80 calculated using Eqn.(6.13), are provided in Table 6.5. The calcu-

Table 6.5: *Estimates of the confidence level for the excess events. k is the number of pixels showing a 3.5σ excess from the average background.*

k	p_k Eqn.(6.13)	p_k MC
1	$1.83{\cdot}10^{-2}$	$1.83{\cdot}10^{-2}$
2	$1.68{\cdot}10^{-4}$	$1.70{\cdot}10^{-4}$
3	$1.02{\cdot}10^{-6}$	$9.60{\cdot}10^{-7}$
4	$4.55{\cdot}10^{-9}$	$4.70{\cdot}10^{-9}$

lations show, for example, that a 4-pixel coincidence within an observational window composed of 80 pixels is an extremely rare case with a probability less than 10^{-8} (which, according to a standard Gaussian distribution, correspond to an estimate of confidence at 6σ level). But, in practice, one could observe one, two, three or even much more bins with a significant excess in the event rate. All those cases should be statistically tested taking into account the total number of selected angular bins within the FoV, which corresponds to the number of independent trials.

In order to prove the formula given by Eqn.(6.13), we also have made straightforward Monte Carlo simulations, randomizing the number of entries for M=80 pixels according to a Gaussian distribution with average value $\langle N_{ON}(i)\rangle = 300$. The results are summarized in Table 6.5 (see column p_k MC). One can see a rather good agreement between the direct Monte Carlo simulations and the values obtained from Eqn.(6.13), taking into account the limited statistics in the Monte Carlo simulations which limits the accuracy of the calculations.

Chapter 7

Observation of the Monoceros Loop SNR with the HEGRA system of IACTs

7.1 TeV emission of Galactic Cosmic Rays ejected from SNRs

As we discussed it in § 1.3.3, the origin of the cosmic rays with energies $E \leq 10^{15}$ eV, the so-called *galactic cosmic rays* (GCRs), is a long-standing problem which has not found a definitive solution yet. Supernova remnants (SNRs) are widely believed to be the sites of galactic cosmic ray acceleration, even though there is still no clear experimental evidence that the nuclear component of cosmic rays is really generated there. Observations of synchrotron radiation from SNRs, basically in the radio band, give an experimental confirmation of the presence of relativistic electrons within these objects. Recently, that was also confirmed by observations in optical, X-ray, and soft γ-ray wavelength bands [100].

There are two major arguments which favor SNRs as sources of GCRs. First, a great success of an advanced theory of diffusive shock acceleration in SNRs [101] was assured during last decade. Second, the very fact that the galactic supernova explosions are actually the only known objects providing the amount of energy necessary to accelerate particles up to $10^{14} - 10^{15}$ eV. The modern theory of cosmic ray acceleration at the shock front via the first order Fermi acceleration mechanism is well-elaborated. It predicts a considerably higher efficiency in the proton acceleration rather than in the electron acceleration. Indeed, up to a 10% of the kinetic energy of the particle flow invading into the shock region may be transformed into the energy of freshly accelerated CRs.

Detection of γ-rays in the GeV and TeV energy ranges, with satellite-borne and ground-based detectors, respectively, will deliver a direct evidence of the acceleration of protons and heavy nuclei at the SNR shock fronts. Indeed, if the nuclear component of cosmic rays is in fact strongly enhanced inside SNRs, then γ-rays have to be inevitably produced in nuclei collisions with the ambient medium through pion production and subsequent pion decay (see § 1.3.3).

Let us assume that a population of particles accelerated via Fermi mechanism has finally an energy spectrum approximately described by a power-law, which is a characteristic feature of a diffuse shock acceleration process in SNRs evolving into the Sedov phase of their expansion (i.e., at the age of $t \geq 10^3 - 10^4$ years and with the radius of the shock exceeding 10 pc). One can estimate the γ-ray flux above 300 MeV from the π^0-decay, which occurs in the interactions of the accelerated protons and nuclei with the ambient matter [14, 105]:

$$F_\gamma(\geq 300MeV) \approx 3 \times 10^{-7}\ A \text{ ph cm}^{-2}\text{ s}^{-1} \tag{7.1}$$

$$A = \theta \left(\frac{E_{SN}}{10^{51}\text{ erg}}\right) \left(\frac{d}{1\text{ kpc}}\right)^{-2} \left(\frac{n}{1\text{ cm}^{-2}}\right) \tag{7.2}$$

where A is a dimensionless scaling factor, n is the density of the ambient media, d is the distance to the source, and θ is the fraction of the total energy of supernova explosion, E_{SN}, which can be converted into energy of cosmic rays. This flux estimate is almost independent of the power-law spectral index, since the energy density of the accelerated particles is fixed.

For a typical SNR in the Sedov phase, the predicted values of θ are 0.1-0.2. Thus, for a power-law spectral index α ($2.1 \leq \alpha \leq 2.3$), the expected γ-ray flux above

100 MeV is given by

$$F_\gamma(\geq E) = 10^{-10}\, E_{TeV}^{-\alpha+1}\, A\, f_\alpha \text{ ph cm}^{-2} \text{ s}^{-1} \quad (7.3)$$

where $f_\alpha \approx 0.9$, 0.43, and 0.19 for a power-law proton spectrum of spectral index α =2.1, 2.2 and 2.3, respectively ($E_{\rm TeV} \equiv E/1$ TeV).

Given the sensitivities of the currently operating ground-based and satellite-borne instruments, detection of GeV and TeV γ-rays from a shell-type SNR becomes possible only if we assume scaling factors $A \geq 0.1$ and $A \geq 1$, respectively. That corresponds to γ-ray fluxes above 1 GeV and 1 TeV of about $10^{-11} - 10^{-10}$ ph cm^{-2} s^{-1} and $10^{-13} - 10^{-12}$ ph cm^{-2} s^{-1}, respectively. For a supernova explosion into an interstellar medium of conventional density ($n \sim 1$ cm^{-3}) and for typical values of $E_{SN} \approx 10^{51}$ erg and $\theta \approx 0.1$, the scaling factor A may exceed 0.1 only for SNRs at the distance $d \leq 1$ kpc. However, these SNRs seem to be hardly observable due to the large angular size of the γ-ray emitting region, which is of about few degrees. The angular size of the γ-ray emitting region is less than 1° only for distant SNRs, with $d \geq 1$ kpc. This conflict between the angular size and the absolute flux makes the detection of γ-rays, both in the GeV and TeV energy ranges, very difficult with currently operating γ-ray instruments.

Nevertheless, supernova explosions which come about in regions of enhanced matter density, like the giant molecular clouds, may be detectable if the density of the *target* material is at least by a factor of 10 or 100 higher than the typical matter density assumed for an uniformly distributed interstellar medium. The EGRET detection of rather high γ-ray fluxes at energies between 100 MeV and 10 GeV towards some radio bright SNRs seems to confirm this possibility [102] [103].

Amongst the 74 Galactic sources ($|b| < 10°$) listed in the 3rd EGRET catalogue [5] which have no established counterparts at other wavelengths, there are 22 of them which are positionally associated with known SNRs [104]. Some of these SNRs exhibit evidence of their strong interaction with nearby interstellar clouds (e.g. W28, W44, γ Cygni, IC 443). It is widely believed that the observed γ-ray emission comes from the interaction of protons accelerated by shock waves with the adjacent giant molecular clouds [105]. Such scenario may well be true for the interaction region of the Monoceros Loop SNR with the rather dense Rosette Nebula molecular cloud, which has been extensively observed using the system of 5 imaging atmospheric Čerenkov telescopes operated by the HEGRA collaboration [106, 107]. The main motivation to observe this region at TeV energies is given by the presence of the unidentified EGRET source, 3EG J0634+0521. The detected γ-ray emission appears to be close to the interaction region of the SNR with the nearby molecular cloud.

7.2 Angular morphology of SNRs in TeV Gamma-rays

The γ-ray emission from SNRs is expected to be extended although marginally high enough to be detectable by the currently operating IACTs [97, 98]. Here, we have modeled the angular shape of the γ-ray emission regions associated with SNRs.

The angular size of a shell-type SNR can be measured in the radio wavelength band. Following the arguments given in [98], in good approximation the γ-ray source can be characterized by a constant brightness all over the SNR radio extent. To simulate the extended emission from a typical shell-type SNR, we have assumed here an angular size of 0.25°, as it is for SN 1006, which has been firmly detected at TeV energies [16].

Three models of TeV γ-ray emission, and the corresponding γ-ray brightness profiles, have been taken from the detailed modeling described in [98], where a SNR shell was assumed to be expanding in an uniform interstellar medium of density $n = 0.3$ cm^{-3}. In one model the γ-ray emission is produced via inverse-Compton (IC) process from a population of accelerated electrons uniformly distributed all over the SNR extension (*circle model*). For two other models, which concern with the γ-ray production from π^0-decay via $p - p$ collisions, the source brightness might peak around the shock front, where the expanding shell collides with the gas of the interstellar medium (*ring model*), or can be concentrated around two emission poles (*double-pole model*), where the interstellar magnetic field becomes perpendicular to the shock front (see Figure 7.1).

We have modeled the response of the HEGRA system of 5 IACTs after 100 hrs of observations for a TeV γ-ray flux as measured from SN 1006 [99] and the brightness profiles given in [98]. The results of the simulations are shown in Fig 7.1. One can see that the morphology of the extended TeV emission could be well traced with the HEGRA system of IACTs. The minimal observing time for a 5σ detection depends on the morphology of the γ-ray emission from such a source. Thus, for the "circle", "ring", and "double-pole" models, the minimal detection time is 16 hrs, 5 hrs, and 2 hrs, respectively. Deep observation of such SNR could allow to study in great detail the morphology of the TeV γ-ray emission and finally distinguish between different models of γ-ray production. Furthermore, we expect the TeV emission to be enhanced by dense nearby giant molecular clouds, as it is the case of the Monoceros Loop SNR.

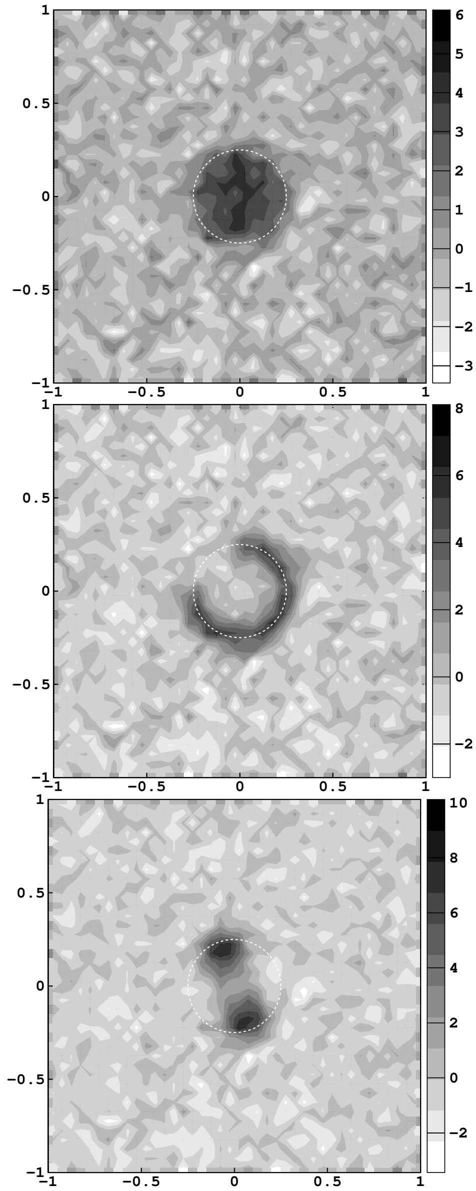

Figure 7.1: *Monte Carlo simulated response of the HEGRA system of 5 IACTs ($n_{tel} \geq 2/5$) after 100 hrs observations for three models of TeV γ-ray emission from shell-type SNRs: "circle" (upper panel), "ring" model for γ-rays simulated over 75% of the entire ring (central panel), "double-pole" model (lower panel). For details on the radial profiles of the TeV γ-ray emission see [98]. The angular size of SNR in radio wavelengths is indicated by the dashed circle. The color palette shows the significance of the simulated excess calculated using Eqn. 6.11.*

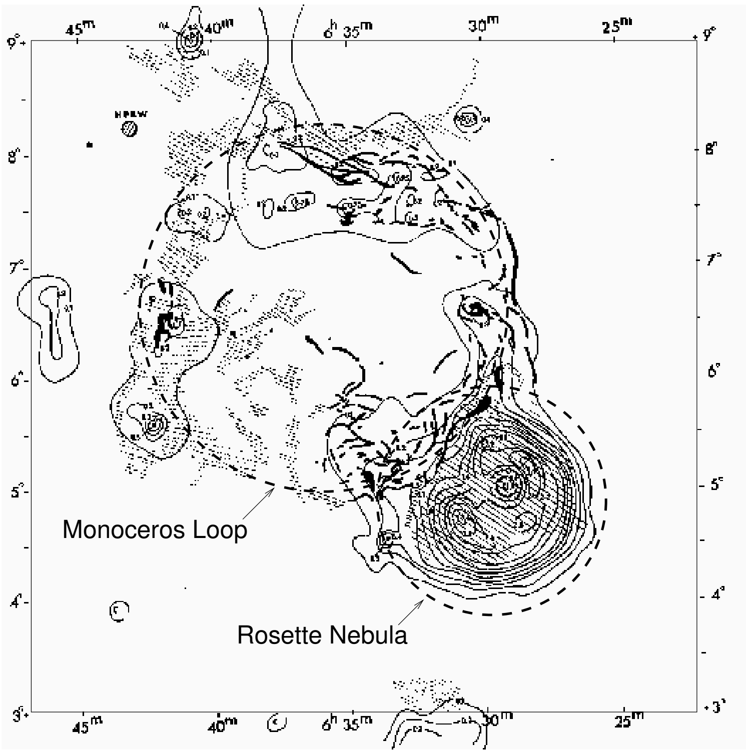

Figure 7.2: *Radio and optical map of the Monoceros Loop region taken from [109]. Contour levels show the radio observations at 2650 MHz. Thicker lines represent optical bright filaments while the shaded regions show the faint optical nebulosity. The Rosette nebula is visible in the south-east portion of the remnant and dominates the radio map. Coordinates refer to the 1950 epoch.*

7.3 The Monoceros Loop and its surroundings

The Monoceros Loop (SNR G205.5+0.5 [108], 220 arcmin in size) was recognized as SNR by Davies et al. [109] from 237 MHz radio observations. At optical wavelengths the Monoceros Loop is visible as an irregular faint ring of emission, around 3.5° in diameter, centered on RA= $6^h38^m43^s$ and DEC=+6°30.2′ (J2000). The very radio-bright Rosette Nebula, a dense molecular cloud where intense stars formation is going on, lays close to the southern-east part of the rim (see Figure 7.2) . The optical and radio properties of Monoceros SNR/Rosette Nebula have been studied in great detail by Davies et al. [109] and Graham et al. [110]. The distance to the Monoceros Loop estimated by Graham et al. [110] is of about 1.6 kpc. The radial extension of the

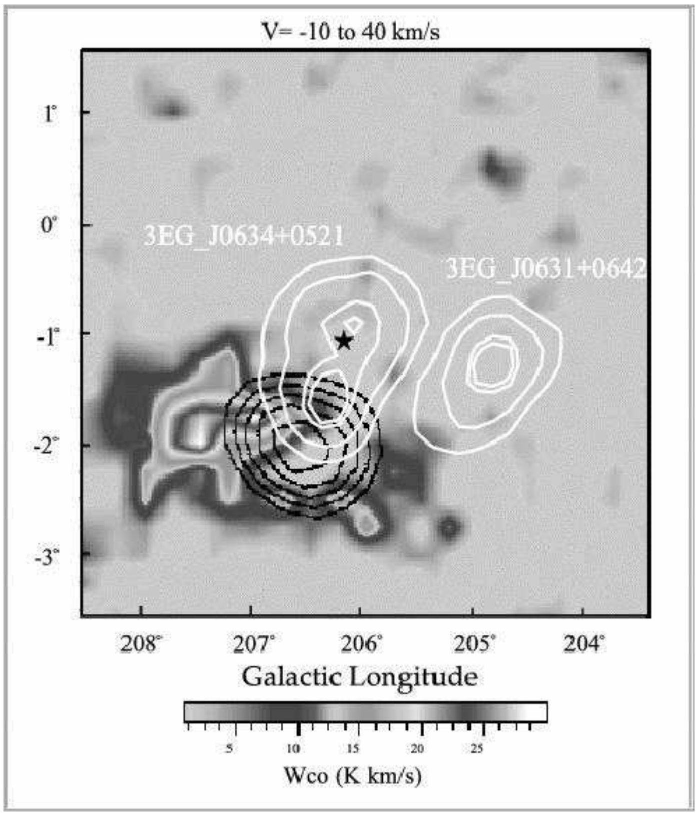

Figure 7.3: *CO emission from the Monoceros Loop region. Contours level mark the emission from the Rosette Nebula at 1.4 GHz. Superimposed are the statistical maps for the two unidentified EGRET sources 3EG J0634+0521 and 3EG J0631+0642 taken from [114].*

remnant is of 50-60 pc, which makes it to occur close by to the Rosette nebula, which has a distance of 1.39 ± 0.1 kpc [111]. The age of the remnant is not well determined, $3 - 15 \cdot 10^4$ yr, but it allows to conclude that the shock expands into the Sedov phase. It has been proposed by [109] [112] that the Monoceros Loop is interacting with the Rosette nebula. According to Davies et al. [109], the filamentary structure visible in the optical band in the southern part of the remnant is a proof of the possible interaction between the loop and the molecular cloud (see Figure 7.2). Detection of the de-excitation line at 1720.5 MHz of the hydroxical radical (OH) is a powerful diagnostic to search for interaction between expanding supernova shells and nearby molecular clouds. A search for OH emission has been performed by [113] for

66 galactic SNRs, and the 1720.5 MHz line has been detected from only 22 of them. This emission line can be explained by emission from masers excited by the SNR shell propagating inside the dense molecular cloud. Despite of no detection of maser emission from SNR G205.5+0.5 in the radio survey at 1720.5 MHz, an interaction with the Rosette Nebula cannot be excluded.

Another useful radio diagnostic tool is the observation of the J=1-0 rotational transition of the carbon monoxide (CO) at 115 GHz, which allows to trace the presence of molecular clouds hitting by expanding SNR shells. Figure 7.3 shows the CO emission intensity map of the Monoceros Loop region. One can clearly see the region of enhanced density coinciding with the Rosette Nebula. The approximate nucleons density of the Rosette Nebula is $40\,\mathrm{cm}^{-3}$ [115]. However there is a large uncertainty in the nucleonic density, which was in fact averaged over the highly inhomogeneous cloud. Such a cloud might have clumps with enhanced density up to $n_H \leqslant 500\,\mathrm{cm}^{-3}$ as it is in the case of IC443 [116].

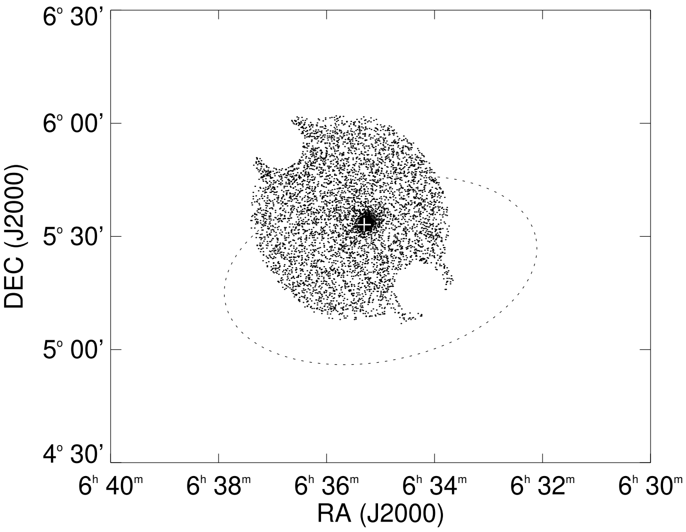

Figure 7.4: *X-ray image of SAX J0635+0533 in the 5-12 kev band taken with the BeppoSax satellite (from [119]). The dashed line shows the 95% confidence error ellipse for 3EG J0634+0521.*

If Monoceros Loop is still in the Sedov phase, rather high X-ray fluxes from this region can be generally expected. The EINSTEIN X-ray satellite has mapped the Monoceros Loop and detected indeed diffuse X-ray emission located straight on the rim of the remnant. Its position coincides with the densest region of the optical filaments [117]. These regions show a high hardness ratio $(> 0.3)^1$ of X-ray emission.

[1] The "Hardness ratio" gives a measurement of the spectral slope of the energy spectrum: Hardness ratio=(H-S)/(H+S) with H = X-ray counts with energies between 0.8 to 3.5 kev, S = X-ray counts between 0.2 to 0.8 kev.

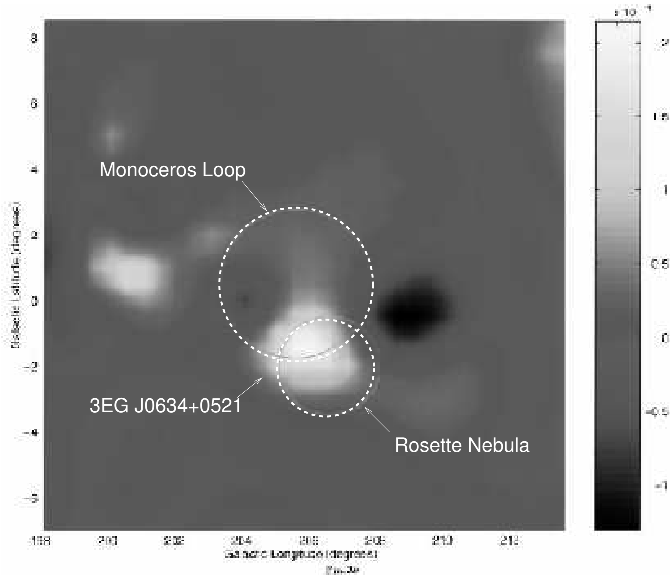

Figure 7.5: *Map of γ-ray emission detected by EGRET from the Monoceros Loop region. The approximate extension and position of the Monoceros Loop (big circle) and the Rosette nebula (small circle) are also shown (from [121]).*

The measured 0.5-3 keV X-ray flux is $1.5 \times 10^{-10}\,\mathrm{erg\,cm^{-2}s^{-1}}$ [118]. Further observations carried out with the BeppoSAX satellite revealed a hard X-ray spectrum of a point source (SAX J0635+533), which is within the 95% probability circle of the EGRET detection [119], and which was later identified as a binary pulsar [120]. The un-absorbed flux from the source is 1.2×10^{-11} ergs cm^{-2} s^{-1} in the 2-10 kev band. No detection of diffuse emission has been reported by BeppoSAX from these observations. However, the field of view of BeppoSAX is relatively small as compared with the EINSTEIN scan and the actual angular extension of the Monoceros SNR.

EGRET has detected from the region associated with the Monoceros Loop/Rosette Nebula an extended γ-ray emission in the energy range from 100 MeV up to 10 GeV at a 7σ confidence level [121] (see Figure 7.5). This emission was interpreted as a γ-ray emission generated in the decay of π^0's produced in the interactions of the protons accelerated by the SNR shock with the ambient matter. The γ-ray flux above 100 MeV is of $(2.55 \pm 0.51) \times 10^{-7}$ ph cm^{-2} s^{-1}. This source is listed in the 3rd EGRET catalog with the name 3EG J0634+0521 [122]. Note that there is another unidentified EGRET source (3EG J0631+0642) in the same region. This source emits photons with energy above 1 GeV and it is also listed in the catalog of GeV sources as GeV J0633+0645 [123].

The other IAC telescope in the northern hemisphere operated by the Whipple group reported an upper limit on γ-ray emission above 500 GeV from the Monoceros SNR/Rosette Nebula interaction region at the level of 1.41×10^{-11} ph cm^{-2} s^{-1} ($\simeq 0.3$ Crab flux) after 13 hrs of observations [124]. This upper limit severely constrains the current models of γ-ray emission. Nevertheless, this upper limit is still consistent with possibly very steep spectrum ($\alpha \simeq 2.4$) of cosmic rays accelerated in SNR.

Table 7.1: *Summary of observational data taken towards the Monoceros Loop region with the HEGRA system of IACTs.* T_{OBS} *is the total observing time.* T_{EFF} *is the effective observational time after data cleaning.* R_{CR} *is the detection rate of the cosmic rays.*

Obs. mode	T_{OBS} [hrs]	T_{EFF} [hrs]	R_{CR} [Hz]	$\langle ZA \rangle$ [deg]
ON	119	114	$\simeq$14	26.7
OFF	19	19	$\simeq$14	26.7

7.4 Data Analysis

The Monoceros SNR/Rosette Nebula interaction region was observed for more than 110 hours with the HEGRA system of IACTs. Observations were performed at most in ON-mode with a limited number of OFF runs taken at $\pm 5°$ away from the tracking point in right ascension. Table 7.4 summaries the observational times in ON- and OFF-modes, average rates, and the corresponding mean zenith angle (ZA). In ON-mode observations the BeppoSAX point source was set into the center of the joint field of view (FoV) of the telescopes (tracking point).

Search for extended γ-ray sources or diffuse γ-ray emission from a certain region of the sky is a none-trivial task. In order to calculate properly the significance of a possible excess of γ-rays one should follow a specific procedure, as we already discussed in § 6.7. Such procedure rely on the total event statistics in OFF-runs. Due to the limited number of OFF runs taken for the Monoceros Loop SNR observations ($\sim$ 20 hrs), we will consider here only the technique used to estimate the CR background directly from a large sample of ON data.

A preliminary analysis of a first data sample of about 40 hrs [106] revealed a positive excess at the level of 2.5σ within the 95% error circle of 3EG0634+0521. A further analysis of the whole data sample based on the technique discussed in § 6.7 demonstrated a positive excess at the level of about 5σ [107]. Here, we report the results of the ultimate analysis, where we used a more accurate reconstruction algorithm of the shower arrival direction and an elaborated background model.

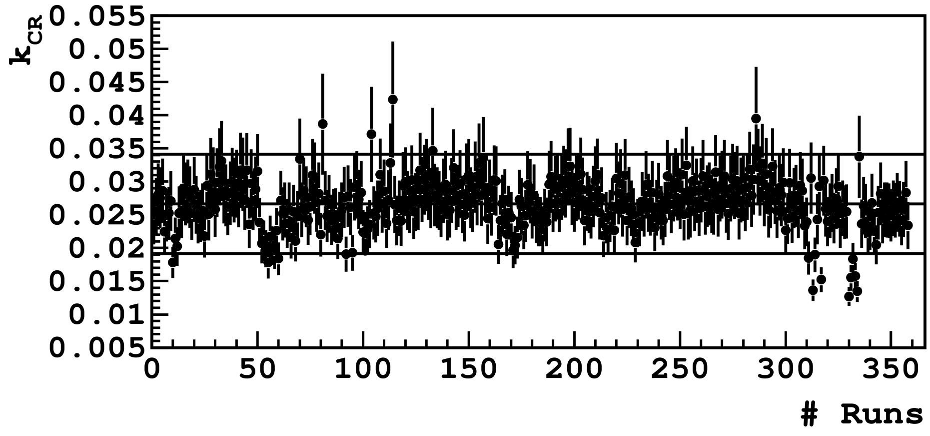

Figure 7.6: *The cosmic ray rejection factor, k_{CR}, versus number of runs after a mscw cut $\langle\tilde{w}\rangle$ <1.1 (Trigger multiplicity: $n_{tel} \geq 3/5$). The 2σ limits are also shown. The points outside the limits correspond to runs with very low trigger rate, close to 30% of the expected one.*

7.4.1 Control of Data Quality

A dedicated data selection procedure has been used here in order to remove the data runs[2] which are shorter than five minutes in duration and show rather low rate[3] as well as occasionally interrupted runs (e.g., by car passing by and hitting with their lights directly the camera *etc*). The easiest way to get rid of bad data runs is to check the run-book notes written by the shift crew. However, this is not the most reliable method since it is based on notes written during the night and sudden change of weather conditions can be often missed by the operators. A good method to exclude data runs of bad quality is to compute the expected rates at the corresponding zenith angle and compare them with the actual rate of recorded events. The runs with rate lower than 30% of the expected one were rejected. That accounted in total for about 5 hours of bad quality data.

Another useful method to check the data quality is to compute the cosmic ray rejection factor, k_{CR}, after applying the *mscw* cut for γ/hadron separation, on a run-by-run basis (see Figure 7.6). One can see that the hadron rejection factor, k_{CR},

[2]Each data acquisition run lasts usually for 20 minutes.

[3]Low rate is usually caused by cloudy sky or not transparent atmosphere, e.g. distorted by the sand flowing from the Sahara desert *etc*.

Table 7.2: *Requirements for selection of good quality γ-like events.*

Number of operating telescopes:	≥ 4
Zenith angle range:	$< 45^\circ$
Algorithm of stereo reconstruction:	#2
Number of triggered telescopes:	≥ 3
Minimum image size cut:	≥ 40 ph.e.
Cut on image center of gravity:	$\leq 1.7^\circ$
Cut on reconstructed impact distance:	< 500 m.
Mean scaled WIDTH cut:	$\langle \tilde{w} \rangle < 1.1$

calculated for the data sample used in the present analysis was rather stable (within $\pm 2\sigma$ variations) during the whole observational period. In addition, a number of other checks of data quality have been applied to the data, e.g. verification of the homogeneity in the camera response over the FoV, control of stability in the *mscw*-distribution of cosmic ray events on a run-by-run basis *etc.*

7.4.2 Selection of good stereo events

Table 7.2 summaries the criteria used for the selection of *good stereo events* in search for TeV γ-ray emission within the quite large EGRET 3EG 0634+0521 error circle ($\theta_{95\%} = 0.67^\circ$) and, serendipitously, over a large fraction of the entire FoV of the HEGRA telescope system. There are three basic algorithms of shower reconstruction yet available (see [68]). Even though we applied all of three algorithm to the data, and found out that the results are consistent, we finally selected Algorithm #2 for the analysis, which appears to be more appropriate for the signal search over broad sky regions. Furthermore, we used in the analysis only events with three triggered telescopes, which provide good angular resolution and efficient γ/hadron separation[4]. Only images with the center of gravity of less than 1.7° were used in the analysis

[4]The angular resolution and γ/hadron separation improve substantially for higher number of telescopes used in the shower reconstruction (see § 4.5.2).

in order to remove the images truncated by the camera edge, which can worsen the shower reconstruction (§ 6.3.1). Finally, applying a cut of 500 m on the reconstructed impact distance of the shower core to the center of telescope system allows to exclude those events which can cause an erroneous scaling of the image WIDTH parameter. A tight image cut on the basic parameter of image shape *mscw*, $\langle \tilde{w} \rangle$ <1.1, has been applied to the selected data in order to reject the events for the hadron-induced showers (see § 4.6). Apart from all these requirements, in the analysis all runs with less than 4 operative telescopes were rejected and, for each run, telescopes showing more than 15 damaged PMTs were also excluded from the analysis.

The average zenith angle of the Monoceros observations was around 26° (see Table 7.4). Using a Crab data sample taken during the same observational period and for the same zenith angle range, we estimated the corresponding energy threshold (defined as the peak of differential γ-ray detection rate) for the Monoceros data sample of about 800 GeV.

7.4.3 Reconstructed event maps from the Monoceros Loop SNR region

Since the stereoscopic reconstruction of atmospheric showers with the HEGRA system of IACTs allowed us to calculate the right ascension (RA) and declination (DEC) for each individual event, it was possible to produce a two-dimensional map of the reconstructed arrival directions for all recorded events which passed the cuts listed on Table 7.2 (see Figure 7.7 (a)).

The FoV was divided into square cells (pixels) of size of $0.2^\circ \times 0.2^\circ$, which is close to the optimum, given the angular resolution of the HEGRA IACTs system for the used trigger multiplicity ($\theta_{68\%} \simeq 0.13^\circ$ (Table 4.2)). At the same time, such bin size leads to a relatively large number of pixels over the FoV. One can compute the average number of cosmic ray events which hit the angular bin of such size and finally estimate the average background contamination as it was described previously in § 6.7. Figure 7.8 shows the fit to the radial dependence of the FoV response function of the HEGRA system of IACTs derived from the data after applying the stereo cuts (see Table 7.2). The fitting function is given by Eqn. 6.3.

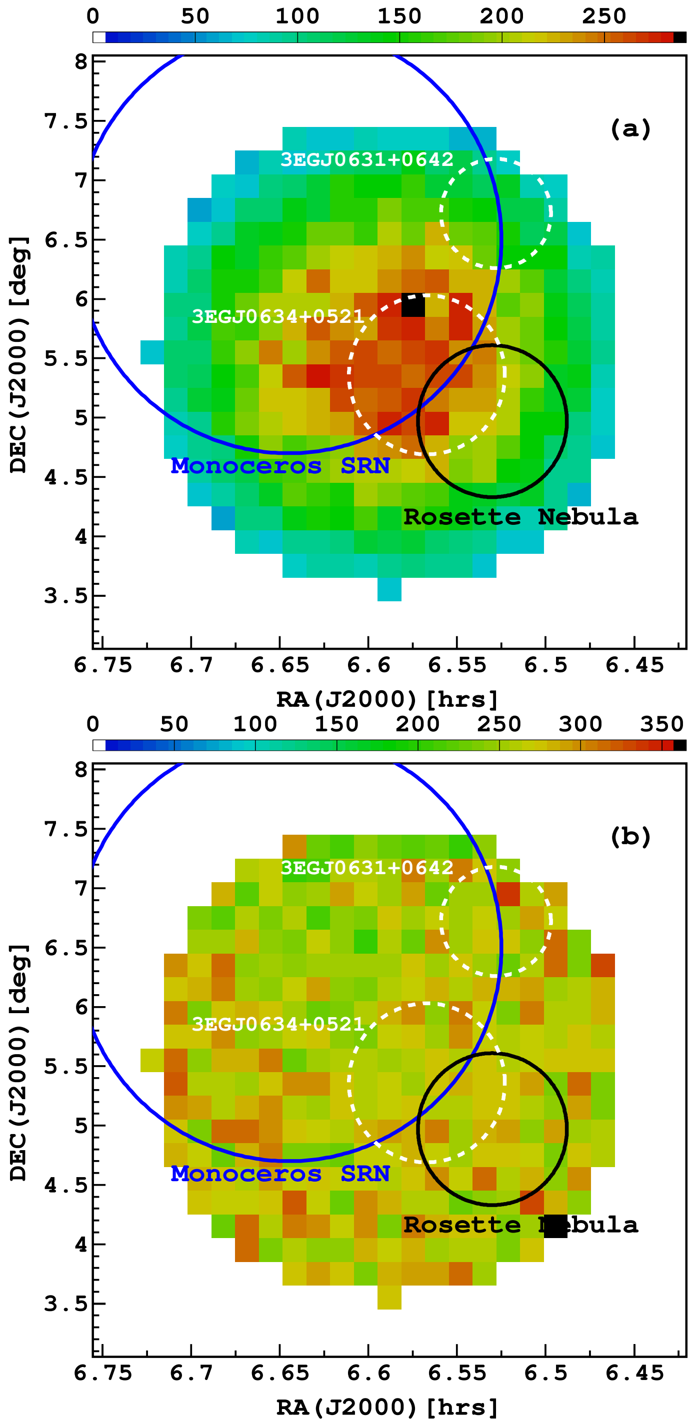

Figure 7.7: *Two-dimensional maps of the arrival positions of all recorded events from the Monoceros Loop SNR region after applying stereo cuts. (a): without flat-fielding; (b): with flat-fielding. Superimposed are the approximate extents of the Monoceros Loop and Rosette Nebula and the 95% error boxes of the EGRET sources 3EG J0634+0521 and 3EG J0631+0642. The color palette shows the number of reconstructed events per angular bin.*

The response function drops down by roughly 20% at 1° distance from the center of field of view. This function was used to correct the actual number of recorded events at different distances from the center of FoV in order to predict the number of counts in case of an absolutely flat response over the FoV. Figure 7.7 (b) shows the two-dimensional map of recorded events after applying such flat-fielding procedure based on the fit shown in Figure 7.8. Assuming that the number of counts per pixel due to cosmic rays has a Gaussian like distribution, one can calculate the mean number of registered events per pixel, which was assumed as the average cosmic ray content per pixel. Correspondingly, one standard deviation of this number is given by $\sigma_i = \sqrt{N_i - \langle N \rangle} \cdot 1/N$, where N_i is the number of reconstructed events in the i-th pixel.

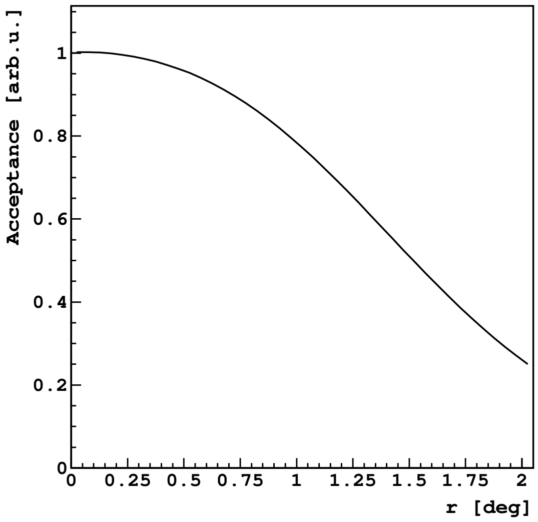

Figure 7.8: *The fraction of detected events (acceptance) from the HEGRA IACTs system as function of distance from the camera center, calculated from the data taken towards the direction of the Monoceros Loop SNR. The function is normalized at 1 at the FoV center.*

Note that at this stage we do not make any assumption about the position of the source: we just use such two-dimensional map (discovery map) for a search of hot spots, which may give a hint where an excess may occur. If any excess of relevant significance is in fact present somewhere in the FoV, it should show up already at this level of analysis, as it was proven by using a sample of γ-ray sources detected by HEGRA. Moreover, the average pixel content calculated over such large number of bins ($M = 100$ in our case, considering all pixels within 2° from the center of FoV) is actually not affected by a few pixels with a possibly high number of counts due to a γ-ray source. Figure 7.9 shows the distribution of the number of counts per pixel corrected for the radial profile in the response function.

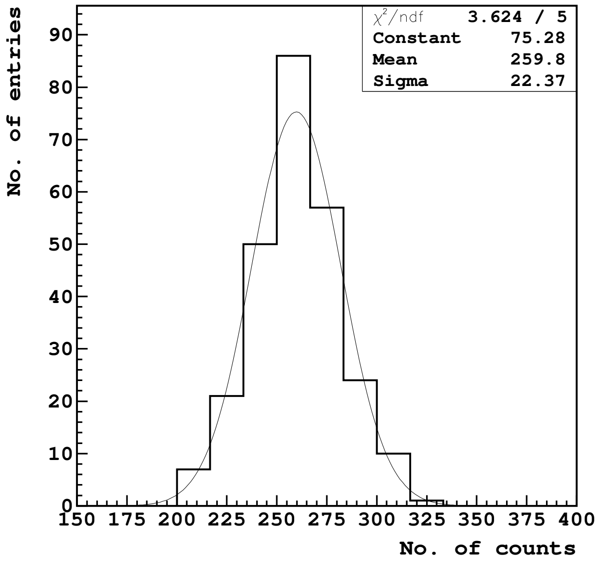

Figure 7.9: *Distribution of the bin content correspondent to the 2D-map of Figure 7.7 (b). Shown are the parameters of the Gaussian fit applied.*

Figure 7.10 shows the two-dimensional map of the stereo reconstructed event direction after flat-fielding (Fig. 7.7 (b)) where are also shown the values of standard deviations (only for $|\sigma_i| \geq 1.0$) from the average number of counts for each pixel. One can see from Figure 7.10 that there are no contiguous pixels with contents deviating significantly from the average. That was an essential condition to be fulfilled in order to perform the analysis described above in § 6.7[5].

Such technique has to be considered as a first preliminary approach to the search for point-like or extended sources over the FoV. In fact, the calculation of the average number of counts per bin might be strongly affected by possibly local inhomogeneities of the response in some parts of the camera, which could lead to artificial excesses in the FoV. An established gradient in count rate (see App. B) across the FoV, due to systematic differences in zenith angles on a scale of 2°, could lead to a noticeable azimuthal (angle ϕ) dependence of the response[6]. Thus, in order to achieve a response over the FoV as much uniform as possible, one has to introduce the corresponding corrections not only for the radial fall of the acceptance, but also for the azimuthal dependence of the response. To compute the function $f = f(r, \phi)$ becomes rather a difficult task and a model-dependent procedure. However, the analysis summarized in App. B has shown that the Monoceros data sample is not significantly affected by such zenith angle gradient.

So-called first-look two-dimensional maps are indeed very useful in those cases

[5]To search for an significant excess from a diffuse like γ-ray source, we asked for at least 3 or 4 contiguous pixels at the level of 3.5 standard deviations.

[6]In a polar coordinate system with an origin in the center of FoV.

where the position of the source is not known *a priori* and can give some hints about the excess position. In what follows, we will discuss a few alternative methods developed for search of point-like and extended sources with unknown position all over the HEGRA FoV.

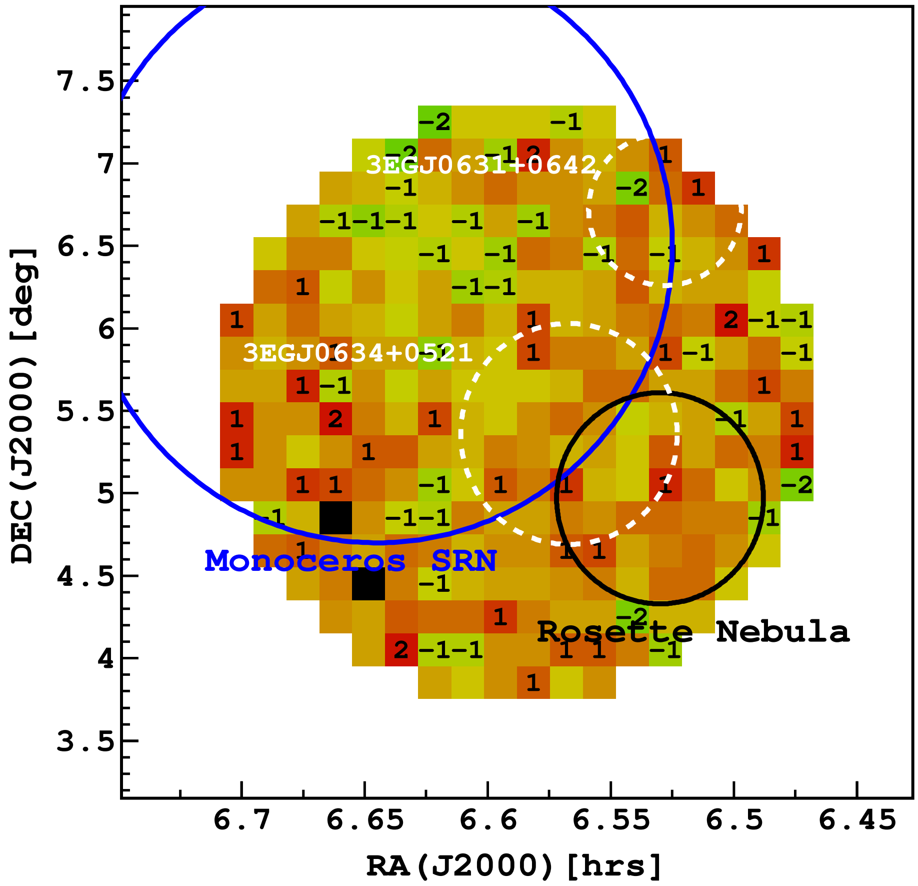

Figure 7.10: *Two-dimensional map of the reconstructed events from the Monoceros Loop SNR region (after application of $\langle \tilde{w} \rangle < 1.1$ cut and flat-fielding). The standard deviations for each pixel from the average number of counts are also indicated on the plot. The values of $|\sigma_i| < 1.0$ are not shown. The part of the FoV with radius great than 2° from the center is not shown because of a strong camera edge effect.*

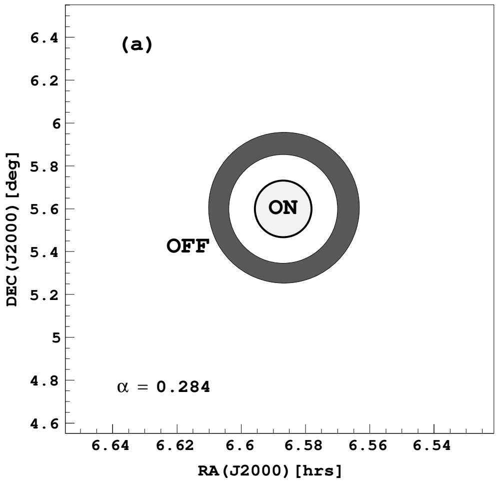

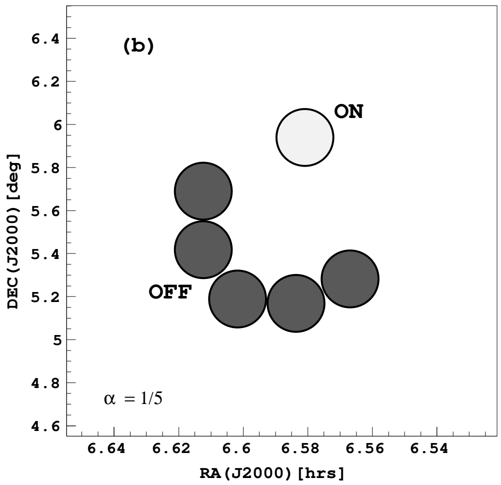

Figure 7.11: *Sketch of two analysis techniques applied for the CR background estimate: (a) Ring background model; (b) Wobble model with 5 OFF regions. The OFF regions are shown in gray color. In both cases, the ON-region (solid line) is placed at the bin center and is shifted from one bin to another.*

7.4.4 Background Models

Three alternative methods of CR background estimation have been applied to the data in order to predict the CR background contamination directly from the big sample of ON data. All those methods are based on a subdivision of the FoV into angular bins of size much smaller than the angular resolution of the instrument. That allows to look for statistical correlation between adjacent bins and search for point-like sources all over the FoV, particularly within the very large EGRET sources error boxes.

The three methods are as follows:

- *Ring background model (Model I)*: For each point of a dense grid with a lattice of 0.04°, all events within a circle of a radius approximately equals to the angular resolution are accumulated. The corresponding OFF-data region is taken from an annular ring centered at the same point (see Figure 7.11 (a)). The number of ON and OFF events is calculated for the same image shape cut: *mscw<1.1*. A ON/OFF scaling factor α has to be introduce:

  $\alpha = r^2_{\mathrm{ON}}/(r^2_{\mathrm{OFF\_EXT}} - r^2_{\mathrm{OFF\_INT}})$.

- *Wobble mode approach (Model II)*: for each grid point, the number of OFF events is computed for N circular regions of the same size, taken symmetrically with respect to the tracking point of the telescopes. Always the same image shape cut *mscw<1.1* is applied (see Figure 7.11 (b)). In this case the scaling factor is simply $\alpha = 1/N$.

- *Template model (Model III)*: Two different shape cuts on *mscw* are applied at the same time on the ON data sample: $\langle\tilde{w}\rangle < 1.1$ for a γ-ray search and $1.3 < \langle\tilde{w}\rangle < 1.5$ for the estimate of the cosmic ray background content[7] per each angular bin [33, 125].

Model I does not require application of any flat-fielding procedure (at least to search for point γ-ray sources within 1° from the center of FoV, where the radial response is stable at the 10% level) and it is not affected by possible systematic errors introduced by such procedure (e.g., for non-uniformity over the azimuth). In the Model II, if the ON and OFF regions are taken at the same distance from the tracking point, the radial dependence of the response is negligible, whereas the zenith angle gradient may introduce some systematic error. Finally, Model III requires the correction for the non-uniform radial acceptance for both regions of the *mscw*-parameter.

Figure 7.12 shows a $3^\circ \times 3^\circ$ sky map generated from the data taken with the HEGRA system of IACTs toward the Monoceros Loop region. The sky map is centered at the tracking point coinciding with the position of the X-ray source – SAX J0635+533. The bin size is of $0.04^\circ \times 0.04^\circ$. The number of excess counts (ON-OFF) for each bin was calculated using Model I, for the standard shape cut of $\langle\tilde{w}\rangle$ <1.1. The size of the search window for each point is of $\theta = 0.13^\circ$, and the OFF region is an annular ring with inner and outer radii of $r_{\rm OFF\_INT} = 0.25^\circ$ and $r_{\rm OFF\_EXT} = 0.35^\circ$, respectively (scaling factor: $\alpha = 0.28$). The size of the point-like search window is comparable to the angular resolution of the HEGRA system of IACTs, which was derived from a sample of Crab data taken at the same observational period and for the same zenith angle range (using the cuts listed in Table 7.2). The radii of the annular ring were optimized using HEGRA data samples from Cas-

[7] In this range of *mscw* values there is a negligible γ-ray contamination.

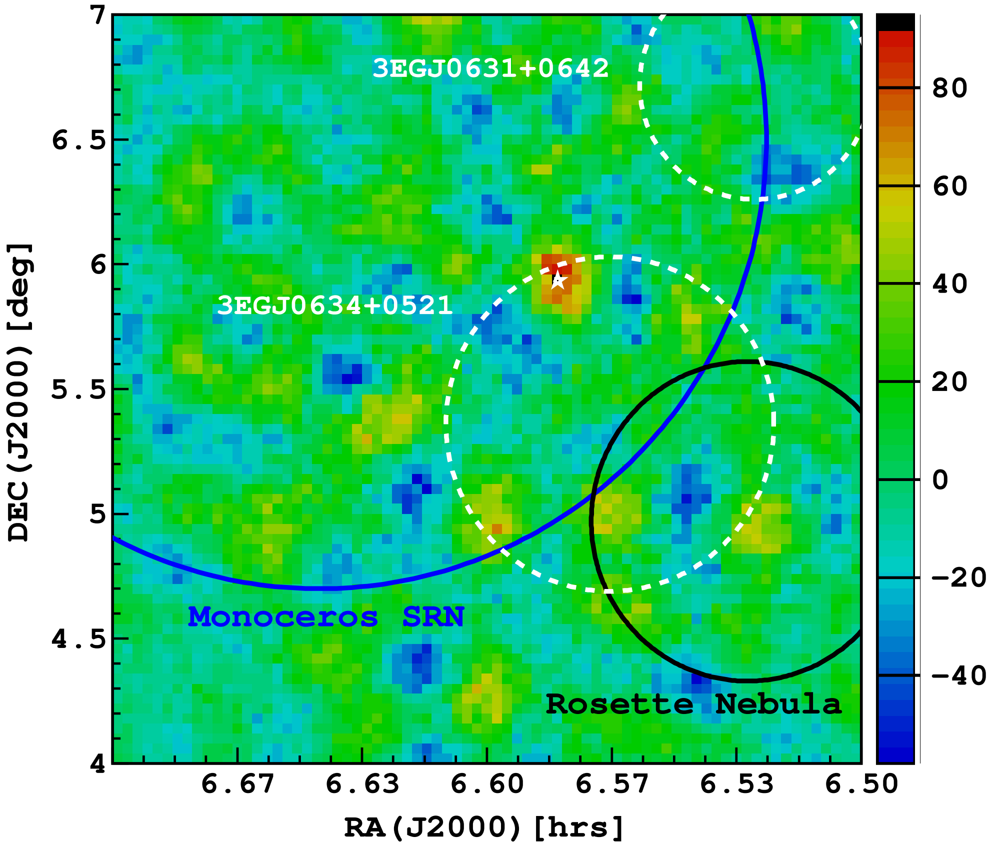

Figure 7.12: $3° \times 3°$ *smoothed sky map of the excess events coming from the direction of the Monoceros Loop (bin size:* $0.04° \times 0.04°$*). For each bin the excess (ON-OFF) is estimated using Model I, as described in the text, with a point-like source search window* $\theta = 0.13°$*. Superimposed are the approximate extents of the Monoceros Loop and Rosette nebula and the 95% error boxes of the EGRET sources 3EG J0634+0521 and 3EG J0631+0642. The white star indicates the COG position of the most prominent excess.*

siopeia A and the unidentified TeV γ-ray source close to the Cygnus OB2 association [18, 33]. It is important to mention that what is being applied here is a kind of *smoothing* of the reconstructed event map. That is useful to pinpoint the position of a possible γ-ray source.

The distribution of the excess significance of all bins, calculated according to Eqn. 6.11, is a good indicator of the accuracy of a background model applied. Any systematic shift of the maximum position or broadening of the distribution shows the erroneous of the method. For an appropriate background estimate the distribution is perfectly centered at zero and has a RMS of $\simeq$1 (see Figure 7.13).

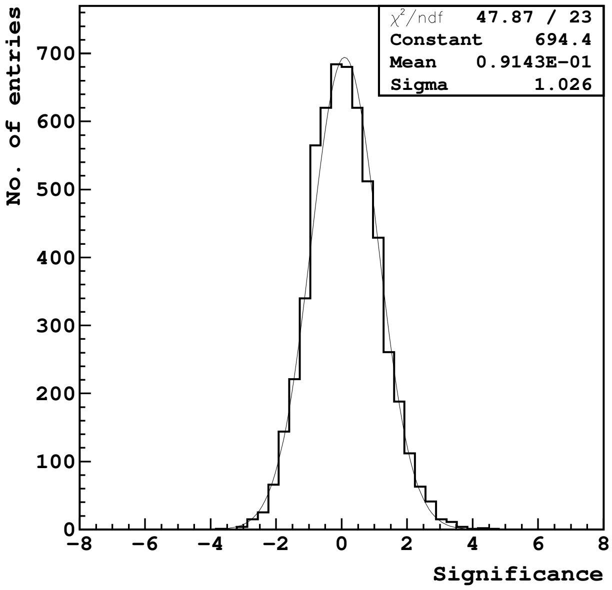

Figure 7.13: *Distribution of the significance per each bin calculated using the Li&Ma's formula (Eqn. 6.11) after applying Model I for the CR background estimation. Shown are the fit to the distribution and the relevant fit parameters.*

One can see from Figure 7.12 that the most significant excess appears within the EGRET error box of the 3EG 0634+521 source. This "hot spot" is also clearly visible in the HEGRA two-dimensional map of the reconstructed shower arrival directions before the flat-fielding procedure was applied (see Figure 7.7 (a)). However, that is partially smoothed over after the flat-fielding procedure (see Figure 7.10)[8]. The same

[8]As we discussed above, the calculation of the radial response function can be affected by disuniformities over azimuth, which could bring to a systematic error in estimation of the pixel back-

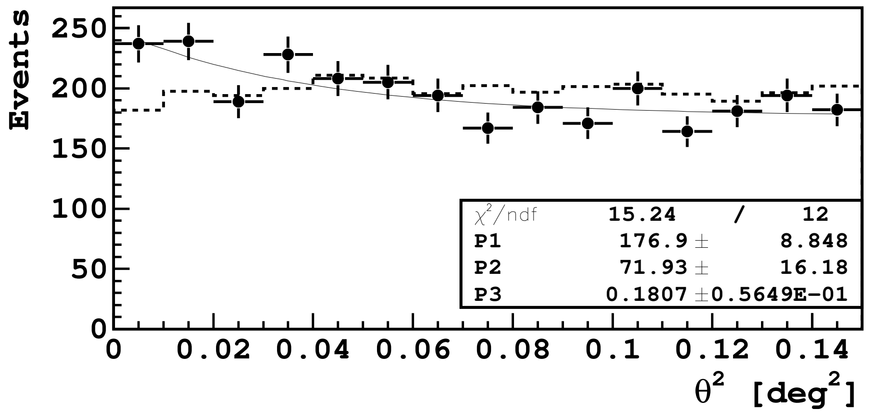

Figure 7.14: *Squared angular distance θ^2 of the arrival directions of the reconstructed event from the position of the COG of the most significant excess detected from the Monoceros Loop SNR region, after application of a cut on $\langle\tilde{w}\rangle$ <1.1 (filled dots). The dashed histogram represents the background estimation derived using Model III. An estimate of the intrinsic source size is derived applying a convolved radial Gaussian fit (see text) using a PSF function for point-like sources estimated from Crab data.*

"hot spot" also appears in the map produced using Model III. We have calculated the center of gravity (COG) of this "hot spot" and the significance of the excess assuming that the emission is possibly coming from a point-like source (angular cut: $\theta <$ 0.13°) using all three background methods mentioned above[9] (see Table 7.3 (a) (b)). The COG position ($\mathrm{RA_{COG}}$; $\mathrm{DEC_{COG}}$) was calculated using the bins composing and surrounding the hot spot (over 50 bins):

$$\mathrm{RA_{COG}} = \sum_i n_i \cdot \mathrm{RA}_i \quad \mathrm{DEC_{COG}} = \sum_i n_i \cdot \mathrm{DEC}_i$$

where n_i is the number of excess counts for the i-th bin of $0.04° \times 0.04°$ size and position (RA_i; DEC_i) included in the COG evaluation. The accuracy in the COG determination is limited by a systematic pointing error of $\sim 25''$ [126]. The statistical error in the COG position can be estimated as $1/\sqrt{\sum n_i}$.

In Figure 7.14 shows the number of reconstructed events as a function of the squared distance from the COG position. If we assume that this excess is really due

ground.

[9]For Model III, the radial profiles and the correspondent correction factor between the two *mscw* ranges have been calculated.

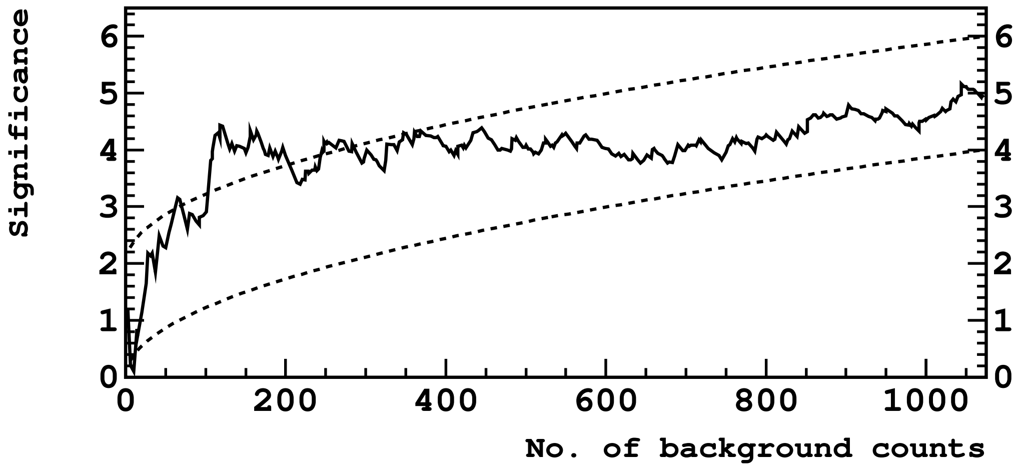

Figure 7.15: *Evolution of the significance of the excess versus the number of accumulated background events estimated using Model I. In case of a constant signal, the significance should develop as* $[\text{background}]^{-1/2}$ *within* $\pm 1\sigma$.

to γ-rays, we can give an estimate of the source size by convolving the radial profile of the squared distance from the COG position with the point-spread function (PSF) of a point-like source determined from Crab Nebula data taken during the same period of time:

$$F = P1 + P2\ \exp(-\theta^2/(P3^2 + \sigma_{pt}^2))$$

where $\sigma_{pt} = 0.08$ is the PSF width for a point-like source estimated from the Crab data. The fit to the data (Figure 7.14) gives an intrinsic source size at the level of 3σ of about $P_3 \equiv \sigma_{src} = 0.18^\circ \pm 0.06^\circ$. Figure 7.15 demonstrates the development of the excess $(N_{ON} - \alpha\ N_{OFF})$ as a function of the total number of accumulated background counts estimated using Model I. In Figure 7.16 the distribution of the excess events over the *mscw* parameter is shown. This plot verifies that the excess at the COG position is consistent with a *mscw* distribution of γ-rays. The Gaussian fit to the *mscw*-distribution shows that it peaks at 1.0 and it is indeed consistent with a population of γ-ray-like events.

The significance of the excess estimated using the three different background models I, II and III (see Table 7.3 (b)) are comparable with each other, even though Model II gives a 20% lower significance. Since the angular size of the "hot spot" indicates a possible source extension, we have also calculated the significance assuming

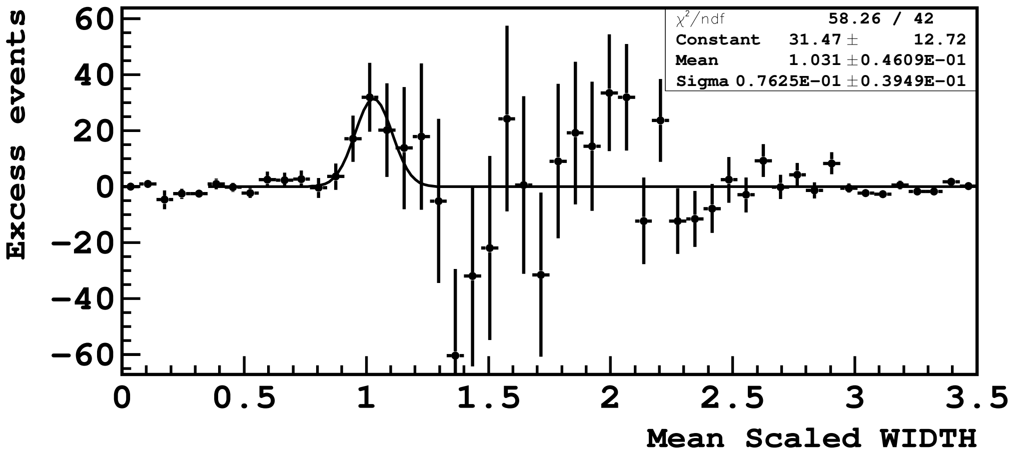

Figure 7.16: *Distribution of the excess calculated from the COG position as a function of mscw after the angular cut $\theta < 0.13°$ and using Model I to estimate the OFF content. Shown is the Gaussian fit to the distribution and the correspondent fit parameters. Note that the Gaussian fit reveals consistency with an excess centered at $\langle \tilde{w} \rangle \simeq 1.0$, as we expect from a population of γ-ray-like events.*

a search window equals to the estimated size of the source: $\sim 0.18°$. The results are summarized in Table 7.3 (c). For that, we did not apply Model II due to the fact that the search window is too large and increasing the radii of the OFF annular ring would change substantially the radial acceptance. For Model II, due to their larger size, only three none-overlapping circular regions have been used for the background estimation.

Table 7.4 summarizes the results for different telescope multiplicities, $n_{tel} = 3/5$, 4/5 or 5/5, considered separately in the analysis. The bulk of excess events is concentrated in the data with the trigger multiplicity $n_{tel} = 3/5$. It appears that for the tracking subset $n_{tel} = 5/5$ the excess position is shifted by about $0.13°$ in RA (see Table 7.5). Such shift is comparable with the angular resolution of the system and with the apparent extension of the excess measured from the COG position. To calculate the values given in Table 7.5, we have used a search window comparable with the angular resolution provided by events with 5 triggered telescopes ($\theta < 0.1°$). All three methods indicate a position excess at about 3σ standard deviations.

Table 7.3: *Results of the analysis for the COG position of the hot spot visible in Figure 7.12. The background content (OFF) has been calculated using the three methods I, II and III, mentioned in the text. The significance S of the excess is calculated using the Li&Ma's formula (Eqn. 6.11).*

(a) Coordinates of the Center of Gravity

$\mathrm{RA_{COG}}$ (J2000):	$6^{\mathrm{h}}\ 34^{\mathrm{m}}\ 51.6^{\mathrm{s}}$	$\pm 1.67^{\mathrm{s}}_{\mathrm{sys}}$	$\pm 7.2^{\mathrm{s}}_{\mathrm{stat}}$
$\mathrm{DEC_{COG}}$ (J2000):	$5^\circ\ 56'\ 5.2''$	$\pm 0.4'_{\mathrm{sys}}$	$\pm 1.8'_{\mathrm{stat}}$

(b) Point-like source analysis: $\theta < 0.13^\circ$, $\langle\tilde{w}\rangle < 1.1$

Background	*ON*	*OFF*	α	*Excess*	*S [σ]*
Annular Ring	403	1072	0.282	101	4.8
Circ. Regions	403	1679	0.2	67	3.3
Template	403	2149	0.145†	88	4.6

(c) Extended source analysis: $\theta < 0.18^\circ$, $\langle\tilde{w}\rangle < 1.1$

Background	*ON*	*OFF*	α	*Excess*	*S [σ]*
Circ. Regions	728	1991	0.33††	71	2.12
Template	728	4226	0.145†	128	4.2

†The scaling factor α contains the correction factor between the ON and OFF regimes according to the requirements of the template model.

††In this case, due to their larger size, only three OFF circular regions have been used.

Table 7.4: *Analysis results for the COG position using the data subsets* $n_{tel} = 3/5$, $n_{tel} = 4/5$ *and* $n_{tel} = 5/5$. *Analysis cuts:* $\theta < 0.13°$, $\langle \tilde{w} \rangle$ *<1.1*

Background model	*ON*	*OFF*	α	*Excess*	*S [σ]*
$n_{tel} = 3$					
Annular Ring	211	530	0.282	62	4.1
Circ. Regions	211	876	0.2	36	3.1
Template	211	700	0.22	57	3.9
$n_{tel} = 4$					
Annular Ring	80	232	0.282	16	1.5
Circ. Regions	80	359	0.2	16	0.9
Template	80	521	0.13	13	1.4
$n_{tel} = 5$					
Annular Ring	72	196	0.282	16	1.9
Circ. Regions	72	295	0.2	16	1.5
Template	72	660	0.09	13	1.5

Table 7.5: *Analysis results for the data subset* $n_{tel} = 5/5$ *with a search window shifted from the COG by* $-0.13°$ *in RA. Analysis cuts:* $\theta < 0.1°$, $\langle \tilde{w} \rangle$ *<1.1*

Background model	*ON*	*OFF*	α	*Excess*	*S [σ]*
Annular Ring	53	221	0.167	16	2.3
Circ. Regions	53	159	0.2	21	3.1
Template	53	389	0.08	22	3.4

7.4.5 Post-trial significance

A serendipitous search for a point-like source all over the FoV of the instrument is subject to statistical penalties or *trial factors*, due to the fact that the hypothesis (no source of γ-rays in any of the bins) has to be tested over a lot number of bins. The choice of the number of trials is indeed quite arbitrary. One can limit the number of trials deciding from where in the sky map is most likely to observe a TeV γ-ray emission, basing this assumption on the presence or not of MeV-GeV, X-ray or radio sources, exposure differences in the camera etc. As we will show in the next paragraph, we can base our region of interest as well on the theoretical expectations discussed at the beginning of the chapter.

The probability of an excess corrected for the trials, P_t, is simply given by

$$P_t = 1.0 - (1 - P)^{N_t} \ ,$$

where P is the one-sided probability correspondent to a significance of $n\sigma$ and N_t is the number of trials. The 4.8σ calculated for the excess in the "hot spot" position (by means of the background Model I) corresponds to a probability $P = 8 \times 10^{-7}$. As our main goal is to identify the extended emission reported by EGRET, it is straightforward to correct for the number of trials contained within the 3EG 0634+521 95% error circle. Nevertheless, we also have treated the most conservative case, where all the trials contained in the initial sky map have been taken into account.

To estimate the number of trials we have made use of the size of our search window, $\theta = 0.13°$. Thus, N_t can be obtained at first approximation dividing the area of the region of interest by the area of the search window. Table 7.6 gives the value of the post-trial significance in the three cases considered: no correction, 3EG 0634+521 region ($r_{95\%} = 0.67°$) and the whole initial discovery map (the "first-look" map, $r = 1.5°$). The oversampling factor between the bin size used in the correlation map (Figure 7.12) and the point-like source search window amounts to a factor of ~ 1.8 and has been calculated by means of a Monte Carlo simulation.

Table 7.6: *Post-trial significance S_t for the excess detected at the COG position calculated previously, for three different assumptions on the number of trials N_t.*

	N_t	S_t $[\sigma]$
no correction	1	4.8
3EG 0634+521 error circle	27	4.0
$r = 1.5°$ *sky map*	133	3.7

7.5 Significance of excess from the interaction region

Up to now, we have simply scanned the entire HEGRA FoV in search for a point-like source and, indeed, have found some hints of slightly extended emission from one point inside the large 3EG 0634+521 error circle. Now, based on the physical arguments and numerical computations summarized at the beginning of this chapter, we can formulate the hypothesis that the TeV γ-rays emission may occur within the interaction region between the SNR shock front and the molecular cloud. Moreover, this region appears to be inside the 3EG 0634+521 error circle. As we have seen previously (§ 7.2), the γ-ray emission is expected to follow the radio profile of the shell and can be substantially enhanced by the interaction with a dense molecular cloud, like the Rosette Nebula. Therefore, as ON region we have assumed here a circular sector placed just where the SNR shell and the molecular cloud supposedly collide (see Figure 7.17). Taking into account the uncertainties in the position and extension of the Monoceros Loop SNR shell as well as the angular dimension of the Rosette Nebula, we have assumed an angular size of the interaction region of 0.4° in the radial direction. In order to estimate the background contamination for this region and derive the corresponding significance, we have taken three sky regions of the same shape and size chosen from different parts of the FoV (see Figure 7.17). These regions have been selected in areas where neither we do *a priori* expect TeV

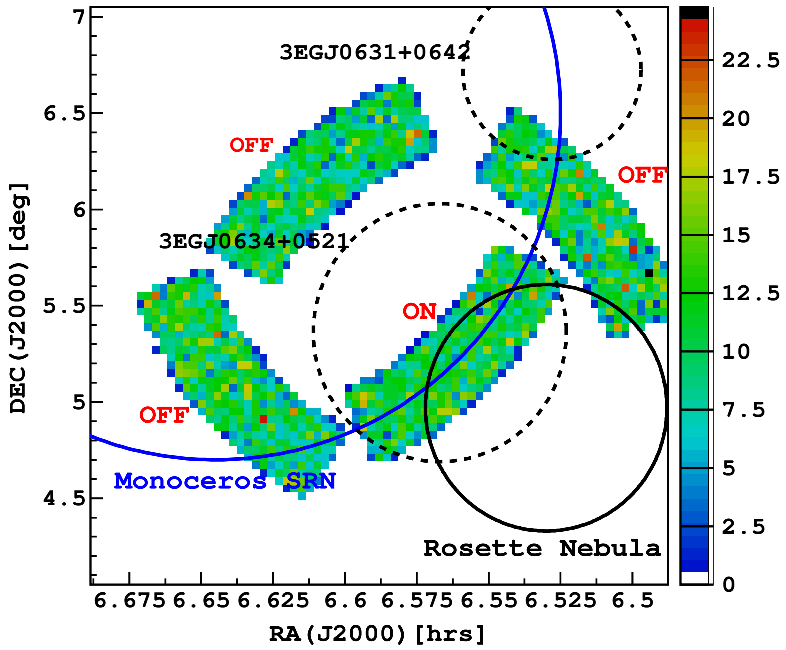

Figure 7.17: *Scheme of the search for TeV γ-ray emission from the interaction region between the Monoceros Loop SNR shock front and the Rosette Nebula (ON region). The three OFF regions are used for the estimation of the CR background contamination.*

γ-ray emission nor we have found it from the previous search[10]. The same "good stereo event selection" cuts summarized in Table 7.2 have been applied to the data and the number of ON and OFF counts have been determined after application of the usual image shape cut $\langle\tilde{w}\rangle$ <1.1.

The number of ON and OFF counts, the correspondent scaling factor α (which in this case is simply 1/3), the number of excess events and the corresponding significance calculated according to Eqn. 6.11, are given in Table 7.7. The numbers of events from the ON and OFF regions have been calculated after the correction of the radial acceptance by means of the function shown in Figure 7.8. Table 7.7 reports also the 99% CL confidence upper limit for the selected extended region, which was calculated using the procedure described in [127]. The upper limit is given in Crab units as well as in units of [10^{-12} ph cm^{-2}s^{-1}]. The integral flux from the Crab Nebula for $E >$ 800 GeV (Φ_{Crab} $(E > E_{th}) = 2.5 \times 10^{-11}$ ph cm^{-2}s^{-1} where E_{th} =800 GeV)

[10]The "hot spot" found before is outside of the three OFF regions.

Table 7.7: *Analysis results for the interaction region Monoceros Loop SNR/Rosette Nebula. The 99% CL upper limit is also reported, both in* [ph cm^{-2} s^{-1}] *and Crab Flux units.*

Background	*ON*	*OFF*	α	*Excess*	$S\,[\sigma]$	$\Phi_{\gamma,UL}$ [10^{-12} cm^{-2}s^{-1}]	$\frac{\Phi_{\gamma,UL}}{\Phi_{crab}}$
3 OFF reg.	3504	9930	0.333	194	2.9	1.1	0.044

was calculated using the differential spectrum taken from [60]. The Crab γ-ray rate needed for the upper limit estimation, was calculated from Crab data taken during the same period of time and for the same range of zenith angles (after applying the event selection cuts given in Table 7.2 and the image shape cut $\langle\tilde{w}\rangle$ <1.1). To estimate the upper limit for the extended region, we have included a geometrical factor of 10 which takes into account the ratio between the angular dimension of the search window region for a point-like source (from which the Crab flux has been integrated) and the angular extension of the extended region assumed as ON source.

7.6 Upper limits on 3EG J0631+0642

As we have mentioned previously, there is another unidentified EGRET source in the Monoceros Loop SNR region, numbered 3EG J0631+0642 (also listed as GeV source (GeV J0633+0645) in [123]), which is clearly visible on the sky maps shown before. It is centered at 1.47° from the tracking point of the observations of 3EG 0634+521, and it is within the FoV of the HEGRA system of IACTs. Interestingly, it also lies on the rim of the Monoceros SNR shell.

We have estimated the upper limit on γ-ray emission from the sky region coinciding with the 3EG J0631+0642 error circle ($\theta_{95\%} = 0.46°$) using two OFF regions of the same size and placed at the same distance from the center of FoV. Table 7.8 summarizes the significance and the 99% CL upper limits after applying two different shape cuts, $\langle \tilde{w} \rangle$ <1.1 and $\langle \tilde{w} \rangle$ <1.0. Figure 7.18 shows the smoothed sky map of the excess events for the very tight image shape cut $\langle \tilde{w} \rangle$ <1.0. The spot appearing on the sky map within the 3EG J0631+0642 error circle has a pre-trial significance of about 2.8σ, which is fully compatible with a background fluctuation after corrections for the number of trials.

Table 7.8: *Analysis results for 3EG J0631+0642 (GeV J0633+0645).*

Shape cut	*ON*	*OFF*	α	*Excess*	$S\,[\sigma]$	$\Phi_{\gamma,UL}$ $[10^{-12}$ $cm^{-2}s^{-1}]$	$\frac{\Phi_{\gamma,UL}}{\Phi_{crab}}$
$\langle\tilde{w}\rangle < 1.0$	880	1786	0.5	-13	-0.4	..	..
$\langle\tilde{w}\rangle < 1.1$	2034	4129	0.5	-30	-0.6	0.34	0.013

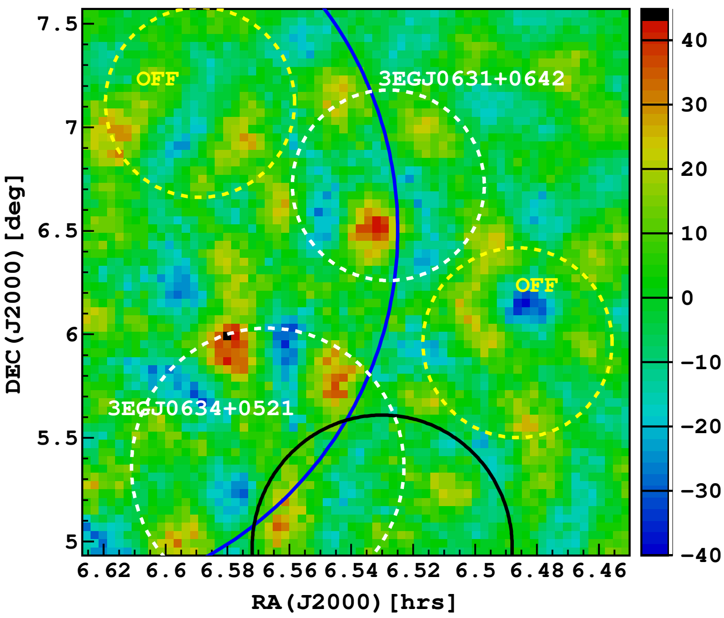

Figure 7.18: *Two-dimentional map of the reconstructed events from the direction of the unidentified EGRET source 3EG J0631+0642 (also GeV J0633+0645), placed at 1.47° from the tracking point. Data were analysed applying the shape cut $\langle\tilde{w}\rangle$ <1.0. Two OFF regions (yellow circles) at the same distance from the FoV center were used to estimate the CR background contamination.*

7.7 Discussion and Conclusions

The Monoceros Loop SNR region was observed with the HEGRA stereoscopic system of 5 IACTs for about 120 hrs in 1999/2001. The results obtained by using two different analysis techniques have indicated a slightly extended excess of events located within the 3EG 0634+521 error circle, with a post-trial significance of about 4σ.

If we assume that this excess of events (see Table 7.3 (b)), is caused by VHE γ-rays, we can make an estimation of the integral flux in Crab units simply dividing the observed γ-ray rate from this region by the well established γ-ray rate from the Crab Nebula. The excess detected here gives a total number of γ-rays of $N_\gamma = 101 \pm 28$[11]. The Crab rate for the same analysis cuts is of 38 ph/hr. Taking into account the observation time, the calculated integral γ-ray flux from this region is $(2.7 \pm 0.8)\%$ of the Crab flux. Using the HEGRA measured spectrum of the Crab Nebula [60], we can convert this value into absolute flux:

$$F_\gamma\,(E > 800\ GeV) = 2.7\%\ \Phi_{Crab}\,(E > 800\ GeV) = (0.68 \pm 0.20) \times 10^{-12}\ \mathrm{ph\ cm^{-2}\ s^{-1}}$$

where 800 GeV is the energy threshold for the Monoceros observations and $\Phi_{Crab}\,(E > E_{th}) = 2.5 \times 10^{-11}$ ph cm^{-2}s^{-1}.

Due to the limited event statistics, we are not able to perform any spectral study here. The main conclusion from our investigations is that the post-trial significance of the excess is not high enough to claim a firm detection of a new extended TeV γ-ray source although it provides evidence of possible detection. That is also the case for the interaction region between the expanding SNR shell and the Rosette Nebula, which shows an excess at the 3σ level. Torres et al. [114] postulated that the extended emission detected by EGRET from 3EG 0634+521 could be the result of a composite emission: a part of the γ-rays would come from the binary pulsar SAX J0635+533 and the other one from the interaction region between the expanding shell and the Rosette Nebula. Unfortunately, the COG of the most significant excess is not coincident with the position given by BeppoSAX, and we could not confirm such scenario.

The next-generation Čerenkov telescopes, like H.E.S.S. [48], MAGIC [49], and VERITAS [50], with sensitivity at least one order of magnitude better than the

[11] We considered here the excess calculated using the background Model I. The statistical error, calculated taking into account the error of the scaling factor α, is also reported.

HEGRA system of IACTs, will be able to prove unambiguously the evidences of detection reported here. Furthermore, they will finally solve the puzzle about the origin of the galactic cosmic rays, which the ground-based Čerenkov telescopes operated up to now have not been able to solve.

To conclude, we can estimate what is the expected γ-ray rate from the EGRET source 3EG 0634+521 in case the EGRET spectrum prolongs continuously up to TeV energies. The reported 3EG 0634+521 flux is $F_\gamma(> 100\ MeV) = (2.55 \pm 0.51) \times 10^{-7}$ ph cm^{-2} s^{-1}. Extrapolating this flux to TeV energies one can calculate the corresponding γ-ray rate over the interaction region we have selected (see § 7.5). That covers approximately 1/3 of the 95% EGRET error circle. Considering an effective area of 10^9 cm^2 at 1 TeV, the corresponding γ-rays rate would be:

$$R_\gamma \approx 9 \cdot 10^{-3} \text{ Hz} .$$

The average CR rate for the HEGRA system of IACTs is about 17 Hz (Table 4.4). The CR rate for a region with a point-like source extension will be given by:

$$R_{CR}^{pt} = 17 \cdot (\theta_0/R_{cam})^2 \approx 6 \times 10^{-2} \text{ Hz}$$

where $R_{cam} \simeq 2.3°$ is the angular size of the camera.

For an observing time of $T_{OBS} \approx 114$ hrs and after a cut on $\langle\tilde{w}\rangle$ <1.1, the resulting signal-to-noise ratio would be (see Eqn. 6.5):

$$S/N = R_\gamma\kappa_\gamma/[R_{CR}^{pt}\kappa_{CR} \cdot (\theta_{ext}/\theta_0)^2]^{1/2}t^{1/2} \approx 25$$

where $(\theta_{ext}/\theta_0)^2$ is the ratio between the extended and the point-like source areas (around 10) and the acceptances κ_γ and κ_{CR} are equal to 0.68 and 0.04, respectively (for a trigger multiplicity of $n_{tel} \geq 3/5$ (see § 4.6)). This value is clearly in contradiction with our observations and the upper limit previously reported by the WHIPPLE group [124]. Therefore, a noticeable steepening in the observed EGRET spectrum is plausible towards TeV energies.

Chapter 8

Conclusions

The HEGRA system of Čerenkov telescopes has proven to be one of the best instruments in the field of VHE γ-ray astronomy with ground-based detectors.

The HEGRA collaboration has been the first one to apply the stereoscopic technique to the observation of atmospheric showers induced by VHE γ-rays coming from astrophysical sources (see § 4). The noticeable angular resolution (up to 0.06°) and the high rejection power of the hadronic-induced cascades has permitted to reach very significant results which have shown the effectiveness of the stereoscopic technique.

The observations of the Crab nebula at energies above 500 GeV at $> 5\sigma$ level in 1 hour [60], the continuously monitoring of Mkn 501 [61] and Mkn 421 [62], the detection of the AGNs H1426+428 [38] and 1ES1959 [63], the SNR Cassiopeia A [18] and the unidentified TeV source close to the Cygnus OB2 association [33], represent very relevant results which confirm the theoretical expectations foreseen for the stereoscopic imaging technique.

The determination of the energy of the primary γ-ray inducing the air shower by the HEGRA system has proven to be one of the most accurate, thanks to the high accuracy in the reconstruction of the shower core position (with a precision within 10 to 20 m.), as it was shown in the spectral studies of the whole AGNs detected.

During my stay in the HEGRA collaboration as PhD student, I have been involved in the exploitation of new observational possibilities, specifically, the study of extended emission of VHE γ-rays with the system of Čerenkov telescopes. Using the very well calibrated MC simulations available within the collaboration [41], I have studied the possibilities to detect VHE photons from extended sources all over the available field of view of the instrument [84]. The results of my investigations (see § 6) showed that the γ-rays detection rate is almost constant up to $1°$ from the center of the field of view. Furthermore, the angular resolution and the gamma/hadron rejection factors are still very good well beyond $1°$ from the camera center. Since the main goal of the thesis is the study of extended emission, I have developed a special technique to deal with excesses due to γ-rays which cover more than $0.13°$.

As a practical case, we have observed the SNR remnant named "Monoceros Loop", which is supposedly being interacting with a very dense molecular cloud, the Rosette Nebula [128]. The EGRET experiment on board of the CGRO γ-rays satellite observed from this region an extended emission yet unidentified, (3EG J0634+0521 [121]), which, together with the theoretical expectations, makes of this object a very good candidate to be an extended source of VHE photons.

Based on theoretical assumptions, we expected that the extended emission would come from the sky region where the shock front of the expanding SNR meets the molecular cloud. Thus, we have estimated the significance for an extended region placed at this position, finding a positive excess of around 3σ (see § 7.5).

Due to the very badly determined position of the EGRET excess, we have also performed a serendipitous search of point-like γ-rays sources all over the available field of view of the HEGRA system. Interestingly, we have found an excess of VHE γ-rays (by means of two different background estimations) within the error circle of the EGRET detection, with a post-trial significance of around 4σ (see § 7.4.4). This excess shows also a slight indication of extension, with a size of around $0.2°$.

Unfortunately, the significance in both the above cases is not high enough to allows us to firmly claim a detection of a new TeV source.

Contrary to most of the theoretical expectations, only a few SNRs have been detected by the actual ground-based detectors, which leaves opened the solution of the long-standing problem about the origin of cosmic ray in our Galaxy. In general, the sensitivity of the HEGRA stereoscopic system is such that a source at the level of a few percent of the Crab flux ($\sim 10^{-12}$ ph cm^{-2} s^{-1}) is visible after very deep observations (> 100 hours, like Cas A). It is undoubted that, in order to increase the number of VHE photons sources, the sensitivity of the actual ground-based detectors has to be increased by at least one order of magnitude.

Moreover, due to the very steep spectra of the sources detected up to now, it is essential for a Čerenkov detector to have as a low threshold as possible (by means of larger light collector surfaces, higher photomultiplier quantum efficiency, etc.) in order to increase their differential detection rate towards the sub-TeV energy range. In my PhD work, we showed that it was possible to lower the energy threshold of the instrument without any major hardware changes, by applying an advanced *topological trigger* to the HEGRA telescope system (see § 5 and [52]). Limiting the active trigger zones in the cameras of photomultipliers, and selecting only events which trigger at least 4 out of 5 telescopes of the system, we were able to select those events with a reconstructed impact distance within the geometrical area of the array. These events are mainly induced by sub-TeV energy events. The restrictions cited above permitted to operate with a local photomultiplier trigger threshold of 4 photo-electrons. We tested and implemented the *topological trigger* observing the Crab Nebula for around 20 hours. The correspondent data have shown that the new energy threshold, around 350 GeV, is a factor 1.4 lower than the nominal value.

To conclude, we think that the next generation of Čerenkov telescopes, with larger reflectors, a sensitivity at least one order of magnitude better than the HEGRA system of Čerenkov telescopes and lower energy thresholds, will be able to detect a much higher number of VHE γ-rays sources, permitting to increase the importance of the ground-based γ-rays astronomy at the level of the observations in the other wavelength bands.

Bibliography

[1] Ong, R.A., *Physics Reports* **305** 93-202 (1998).

[2] Hoffman, C.M., et al., *Rev. Mod. Phys.* **Vol. 71, No. 4** 897-936 (1999).

[3] Weekes, T.C., *Physics Reports* **160** 1 1-121 (1988).

[4] Thompson, D.J., et al., *ApJ Suppl. Ser.* **86** 629 (1993).

[5] Hartman, R.C., et al., *ApJ Suppl. Ser.* **123** 79-202 (1999).

[6] Bell, A.B., *Mon. Not. R. Astron. Soc.* **182** 147 (1978).

[7] Blandford, R.D. & Ostriker, J.P., *ApJ* **221** L29 (1978).

[8] Fermi, E., *Phys. Rev.* **75** 1169 (1949).

[9] Kembhavi, A.K. & Narlikar, J.V., "*Quasars and Active Galactic Nuclei*", Cambridge Univ. Press (1999).

[10] Dermer, C.D. & Schlickeiser, R., *ApJ* **416** 458 (1993).

[11] Maraschi, L., Ghisellini, G., Celotti, A., *ApJ* **397** L5 (1992).

[12] Mannheim, K., *A&A* **269** 67 (1993).

[13] Szabo, A.P. & Protheroe, R.J., *Astropart. Phys.* **2** 375 (1994).

[14] Drury, L.O., Aharonian, F. and Völk, H.J., *A&A* **287** 959-971 (1994).

[15] Aharonian, F.A., *Nature* **Vol. 416 (6883)** 797 (2002).

[16] Tanimori, T., et al., (the CANGAROO collaboration), *ApJ* **497** L25-L28 (1998).

[17] Enomoto, R., et al., (the CANGAROO collaboration), *Nature* **416** 823-826 (2002).

[18] Aharonian F.A., et al., (the HEGRA collaboration), *A&A* **370** 112 (2001).

[19] Butt, Yousaf M., et al., *Nature* **418** 499 (2002).

[20] Daugherty, J.K. & Harding, A., *ApJ* **429** 325 (1994).

[21] Daugherty, J.K. & Harding, A., *ApJ* **458** 278 (1996).

[22] Cheng, K.S., Ho, C. & Ruderman, M., *ApJ* **300** 500 (1986).

[23] Hirotani, K., *ApJ* **549** 495 (2001).

[24] de Jager, O.C., et al., *ApJ* **457** 253 (1996)

[25] Hillas, A.M., et al. (the WHIPPLE collaboration), *ApJ* **503** 744 (1998).

[26] Yoshikoshi, T., et al. (the CANGAROO collaboration), *ApJ* **487** L65-L68 (1997).

[27] Kifune, T., et al. (the CANGAROO collaboration), *ApJ* **438** L91.

[28] Berezinskii, V.S., et al., *"Astrophysics of Cosmic Rays"*, North-Holland, Elsevier Science Publishers (1990).

[29] Cheng, K.S. & Ruderman, M., *ApJ* **373** 187 (1991).

[30] Romero, G.E., et al., *A&A* **376** 599 (2001).

[31] Paredes, J.M., et al., *Science*, **288**, 2340, (2000).

[32] Kaufman Bernado, M.M., Romero, G.E. & Mirabel, I.F., *A&A*, **385** L10 (2002).

[33] Aharonian, F.A., et al., (the HEGRA collaboration), *A&A* **393** L37 (2002).

[34] Piran, T., *Phys.Rept.* **314** 575 (1999).

[35] Tsygan, A.I., *Astr. Reports*, **Vol. 42, Issue 6**, 746 (1998).

[36] Padilla, L., et al., (the HEGRA collaboration) *A&A* **337** 43 (1998).

[37] Coppi, P.S. & Aharonian, F.A., *ApJ* **487** L9- (1997).

[38] Aharonian, F.A., et al., (the HEGRA collaboration), *A&A* **384** L23-L26 (2002).

[39] Longair M.S., "*High energy astrophysics. Volume 1: Particles, photons and their detection*", Cambridge Univ. Press (1992), pag. 120.

[40] Jelley, J.V., "*Čerenkov radiation and its application*", Pergamon Press (1958), pag. 3.

[41] Konopelko, A., Plyasheshnikov, A., *Nucl. Instr. Meth. A*, 450, 419 (2000).

[42] Fegan, D.J., *J. Phys. G* **23** 1013-1060 (1997).

[43] Knapp, J. & Heck, D., "*Extensive Air Shower Simulation with CORSIKA*", User's Guide, version 5.61, Apr. 1998.

[44] Weekes, T.C., *Space Sci. Rev.*, **75** 1-15 (1996).

[45] Cawley, M.F., Weekes, T.C., *Exp. Astron.* **6** 7 (1995).

[46] Mirzonian, R. and Lorenz, E., **MPI-PhE/94-35**, (Dec. 1994).

[47] Hillas, A.M., *Space Sci. Rev.*, **75**, 17 (1996).

[48] Hofmann, W., *"The H.E.S.S. Project"*, appeared in Proc. of the Int. Symp. "The Universe viewed in Gamma Rays", Tokyo (2002).

[49] Lorenz, E., *"The 17m MAGIC Telescope for gamma-ray astronomy above 15 to 30 GeV"*, appeared in the Proc. of the "TeV Gamma Ray Workshop", Snowbird, Utah, (1999).

[50] Ong, R.A., *"The VERITAS Project"*, appeared in Proc. of the Int. Symp. "The Universe viewed in Gamma Rays", Tokyo (2002).

[51] Enomoto, R., Hara, S., Asahara, A., et al. (the CANGAROO collaboration), *Astropart. Phys.* **16** 235-244 (2002).

[52] Lucarelli, F., et al., accepted for publication in *Astropart. Phys.* (astro-ph/0209447).

[53] Konopelko, A., et al., *Astropart. Phys.* **10** 275-289 (1999).

[54] Aharonian, F.A., et al., *Exp. Astron.* **Vol. 2, No. 6** 331-344 (1993).

[55] Aharonian, F.A., Hofmann, W., Konopelko, A. and Völk, H.J., *Astropart. Phys.* **6** I: 343-368; II: 369-377; (1997).

[56] Ulrich, M., Daum, A., Hermann, G., Hofmann, W., *J. Phys. G: Nucl. & Part. Phys.*, **24**, 883 (1998).

[57] Le Bohec, S., et al. *Nucl. Instr. Meth. A*, **416**, 425 (1998).

[58] Lessard, R., et al. *Astropart. Phys.*, **15**, 1 (2001).

[59] Daum, A., et al., *Astropart. Phys.* **8** 1-11 (1998).

[60] Aharonian, F.A., et al., (the HEGRA collaboration), *ApJ* **539** 317-324 (2000).

[61] Aharonian, F.A., et al., (the HEGRA collaboration), *ApJ* **546** 898-902 (2001).

[62] Aharonian, F.A., et al., (the HEGRA collaboration), *A&A* **350** 757-764 (1999).

[63] Horns, D. (for the HEGRA collaboration), *"Observations of 1ES1959 with the HEGRA IACTs system"*, in Proc. "The Universe viewed in γ-rays", Tokyo, Sep. 2002.

[64] Aharonian, F., in Proc. "Towards a Major Atmospheric Čerenkov Detector-II", Calgary, (1993), R.C. Lamb (Ed.), p. 81.

[65] Hermann, G., in Proc. "Towards a Major Atmospheric Čerenkov Detector-IV", Padova, (1995), M. Cresti (Ed.), p. 396.

[66] Bulian, N., et al., *Astropart. Phys.* **8, 4** 223 (1998).

[67] Konopelko, A., et al. (the HEGRA collaboration), *Astropart. Phys.*, **4**, 199 (1996).

[68] Hofmann, W., et al., *Astropart.Phys.* **Vol. 12, Issue 3** 135-143 (1999).

[69] Lessard, R. W., et al., *Astropart.Phys.* **15** 1-18 (2001).

[70] Catanese, M. and Weekes, T.C. *PASP*, **111, N 764**, 1193 (1999).

[71] Atoyan, A. and Aharonian, F., *MNRAS*, **278**, 525 (1996).

[72] Krennrich, F., et al. (the WHIPPLE collaboration), *ApJ*, **560**, L45 (2001).

[73] Oser, S., et al. (the STACEE collaboration), *ApJ*, **547**, 949 (2001).

[74] de Naurois, M., et al. (the CELESTE collaboration), *ApJ*, **566**, 343 (2002).

[75] Piron, F., (the CAT collaboration), "*Very high-energy gamma-ray sources as seen by the CAT imaging telescope*", appeared in Proc. of the 36th Rencontres de Moriond on "Very High-Energy Phenomena in the Universe", Les Arcs (France), (2001).

[76] Lampeitl, H., et al., "*Convergent observations with the stereoscopic HEGRA CT system*", Poster presented at the TeV Gamma Ray Workshop, Snowbird, (1999) (astro-ph/9910461).

[77] Li, T., and Ma, Y., *ApJ*, **272**, 317 (1983)

[78] de Jager, O.C., Konopelko, A., Raubenheimer, B.C. and Visser, B., "*Limits on Pulsar Parameters for Pulsed detections with H.E.S.S*", appeared in Proc. of the 27th ICRC, Hamburg (Germany), 07-15 August 2001, p. 164 (2001)

[79] A. K. Harding and O. C. de Jager, in Proc. "Towards a Major Atmospheric Čerenkov Detector V", Berg-en-Dal, South Africa, (1997) pg. 64.

[80] F. A. Aharonian, A. M. Atoyan and T. Kifune, *Mon. Not. R. Astron. Soc.* **291** (1997) 162.

[81] P. T. Reynolds et al., *Astrophys. J.* **404** (1993) 206.

[82] M. Takahashi et al., *IAU Circ.*, **7030** (1998) 3.

[83] J. M. Fierro, Ph.D. Thesis, Stanford University (1995) pg. 173.

[84] Konopelko, A., Lucarelli, F., Lampeitl, H. & Hofmann, W., *J. Phys. G: Nuclear and Particle Phys.* **28** 2755-2770 (2002).

[85] Hofmann, W., et al. *Astropart. Phys.*, **12**, 135 (1999).

[86] Hemberger, M., PhD thesis, MPIH-V19-98 (1998)

[87] Aharonian, F., et al. *Phys. Rev. D* **59**, 092003 (1999).

[88] Aharonian, F., et al., *A & A*, **361**, 1073 (2000).

[89] Aharonian, F., et al., *Astropart. Phys.*, **10**, 1 (1999).

[90] Aharonian, F., et al., *A & A*, **375**, 1008 (2001).

[91] Wiebel, B., *Univ. Wuppertal, Preprint* WUB-94-08 (1994).

[92] Lampeitl, H., *Private Communication.*

[93] Aharonian, F., et al. *Astropart. Phys.*, **6**, 343 (1997).

[94] Konopelko, A., in Proc. "Towards a Major Atmospheric Čerenkov Detector-IV", Padova, ed. M. Cresti, p. 373 (1995).

[95] Hofmann, W., in Proc. "Towards a Major Atmospheric Čerenkov Detector-V", Kruger Park, South Africa, ed. Okkie de Jager, p. 284 (1997).

[96] Li, T. Ma, Y. *ApJ*, **272**, 317 (1983).

[97] Berezhko, E.G., Völk, H.J. *Astropart. Phys.*, **7**, 183-202 (1997).

[98] Berezhko, E.G., Ksenofontov, L.T., Völk, H.J. *A & A*, **395**, 943-953 (2002).

[99] Tanimori, T., et al. *ApJ*, **497**, L25 (1998).

[100] Reynolds, S.P., *ApJ* **459** L13-L16 (1996).

[101] Blandford, R.D. and Eichler, D., *Phys. Rep.* **154** 1 (1987).

[102] Sturner, S.J. and Dermer, C.D., *A&A* **293** L17-L20 (1995).

[103] Esposito, J.A., et al., *ApJ* **461** 820-827 (1996).

[104] Romero, G.E., Benaglia, P. & Torres, D.F., *A&A* **348** 868-876 (1999).

[105] Aharonian, F., Drury, L.O. and Völk, H.J., *A&A* **285** 645-647 (1994).

[106] Lucarelli, F., et al., in "*High-energy Gamma-ray Astronomy*", edited by F. Aharonian and H. Völk, AIP Conference Proceedings (NY), p. 779 (2001).

[107] Lucarelli, F., Konopelko, A. & Fonseca, V., in Proc. of the 27th Inter. Cosmic Ray Conf., Hamburg, Session OG Vol. 6 p. 2461 (2001).

[108] Green, D.A., " A catalogue of Galactic Supernova Remnants (version 2001 Dec.)", Mullard Radio Astr. Obs., Cavendish Lab., Cambridge (UK) (2001) (http://www.mrao.com.ac.uk/surveys/snrs/).

[109] Davies, R.D., et al., *A&AS* **31** 271-284 (1978).

[110] Graham D.A., et al., *A&A* **109** 145-154 (1982).

[111] Hensberge, H., Pavloski, K., & Verschueren, W., *A&A* **258** 553 (2000).

[112] Odegard, N., *ApJ* **301** 813 (1986).

[113] Frail, D.A., et al., *Astronom. J.* **Vol. 111, N. 4** 1651 (1996).

[114] Torres, D. F., et al., (astro-ph/0209565).

[115] Williams, J.P., Blitz. L., Start, A. *ApJ* **451** 252 (1995).

[116] Dickman, R.L., Snell, R.L., Ziurys, L.M., Huang, Y.-L., *ApJ* **400** 203 (1992).

[117] Leahy, D.A., Naranan, S. & Singh, K.P., *MNRAS* **213** *Short Communication* 15p-19p (1985).

[118] Leahy, D.A., Naranan, S. & Singh, K.P., *MNRAS* **220** 501 (1986).

[119] Kaaret, P., et al., *ApJ* **523** 197-202 (1999).

[120] Cusumano, G., et al., *ApJ* **528** L25-L28 (2000).

[121] Jaffe, T., et al., *ApJ* **484** L129-L131 (1997).

[122] Hartman, R.C., et al. *ApJ Suppl.* **123** 79 (1999).

[123] Lamb, R. C. & Macomb, D. J., *ApJ* **488** 872 (1997).

[124] Lessard, R.W., *"Whipple Observations of Supernova Remnants"*, appeared in Proc. of "Heidelberg Gamma-Ray Symposium (2000)", Heidelberg (Germany), June 21-27 2000.

[125] Rowell, G.P., *"An Alternative Background Estimate in Hegra CT-system Data Analysis"*, in "*High-energy Gamma-ray Astronomy*", edited by F. Aharonian and H. Völk, AIP Conference Proceedings (NY), p. 609 (2001).

[126] Pühlhofer, G., Daum, A., Hermann, G., et al., *Astropart. Phys.* **8** 11 (1997).

[127] Helene, O., *Nucl. Instr. & Methods* **212** 319-322 (1983).

[128] Lucarelli, F., Konopelko, A., Fonseca, M.V. (the HEGRA collaboration). *In preparation.*

Appendix A

Mathematical derivation of the Image Hillas parameters of Čerenkov images

In § 3.2, we have introduced the parameterization of the Čerenkov images by means of the Hillas parameters. In what follows, we shall describe more accurately how the parameters are calculated using the second moment analysis of the recorded signal amplitudes for the triggered pixels.

The image parameters are reconstructed from the pixel information: moments are based on the ADC counts in each pixel, together with the corresponding "fired" pixel coordinate. Using moments, we can estimate the value of the image parameters and define the order moments in the following way. The *zero-order* moment is the sum of all the ADC counts in all the pixels which are non-zero, after image cleaning. The *first-order* moments describe the position of the image in the camera focal plane and the *second-order* moments describe the extent of the image. In general, only the first and second order moments are used in the parameterization of the images.

The moments are defined as follows:

$$
\begin{aligned}
\langle x\rangle &= \frac{\sum n_i \cdot x_i}{\sum n_i} & \langle y\rangle &= \frac{\sum n_i \cdot y_i}{\sum n_i} \\
\langle x^2\rangle &= \frac{\sum n_i \cdot x_i^2}{\sum n_i} & \langle y^2\rangle &= \frac{\sum n_i \cdot y_i^2}{\sum n_i} \\
\langle xy\rangle &= \frac{\sum n_i \cdot x_i \cdot y_i}{\sum n_i} & & \\
\langle x^2 y\rangle &= \frac{\sum n_i \cdot x_i^2 \cdot y_i}{\sum n_i} & \langle x y^2\rangle &= \frac{\sum n_i \cdot x_i \cdot y_i^2}{\sum n_i}
\end{aligned}
$$

where (x_i,y_i) and n_i are the i-th pixel coordinates (in a reference system centered at the camera center) and ADC counts, respectively. Spreads of the images in different directions are then defined in terms of the moments in this way:

$$
\begin{aligned}
\sigma_x^2 &= \langle x^2\rangle - \langle x\rangle^2 \\
\sigma_y^2 &= \langle y^2\rangle - \langle y\rangle^2 \\
\sigma_{xy} &= \langle xy\rangle - \langle x\rangle\langle y\rangle
\end{aligned}
$$

Finally, the various image parameters can be calculated from the previously defined moments and image spreads as follows:

$$
\begin{aligned}
length &= \sqrt{\frac{\sigma_x^2 + \sigma_y^2 + s}{2}} \\
width &= \sqrt{\frac{\sigma_x^2 + \sigma_y^2 - s}{2}} \\
distance &= \sqrt{\langle x\rangle^2 + \langle y\rangle^2} \\
alpha &= \arcsin\frac{miss}{distance} \\
miss &= \sqrt{\frac{1}{3}\cdot(u\langle x\rangle^2 + v\langle y\rangle^2) - (\frac{2\sigma_{xy}\langle x\rangle\langle y\rangle}{s})} \\
azwidth &= \sqrt{\frac{\langle x\rangle^2\langle y^2\rangle - 2\langle x\rangle\langle y\rangle\langle xy\rangle + \langle x^2\rangle\langle y\rangle}{distance^2}}
\end{aligned}
$$

where:

$$s = \sqrt{d^2 + 4(\sigma_{xy})^2}$$

$$d = \sigma_y^2 - \sigma_x^2$$

$$u = 1 + \frac{d}{s} \qquad v = 2 - u$$

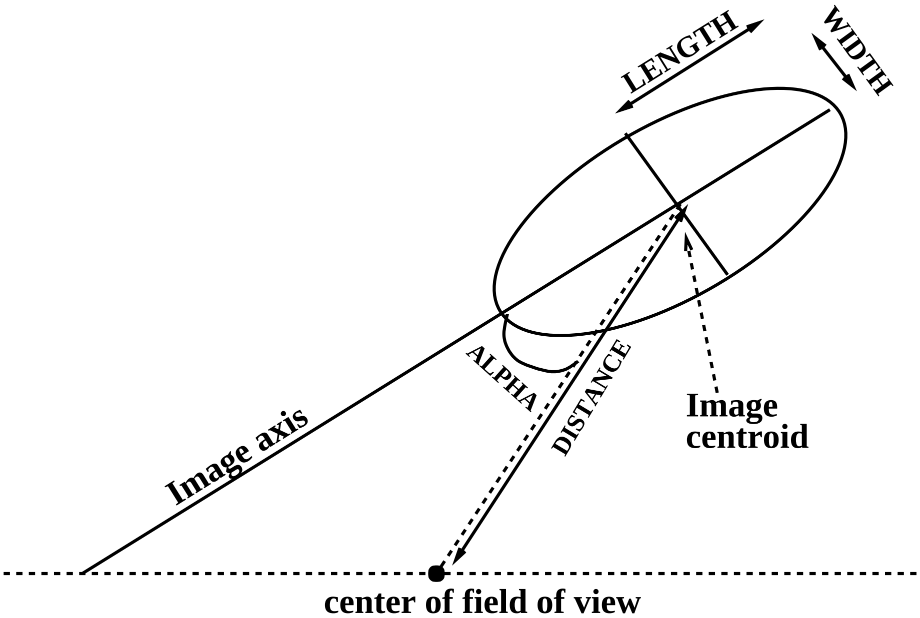

Figure 8.1: *Hillas parameters of the Čerenkov images.*

Appendix B

Systematics effect in a big sample of data

The Monoceros data set is one of the bigger data sample available in all the HEGRA CT-system database and is very useful in order to study systematic effects that can arise in such a long observation time and can noticeably affect the search for extended sources all over the field of view.

The main systematic effect that can arise after such a long observation time in ON mode is the *ZA effect*. The detection rate is a function of the zenith angle (it goes as $\sim cos(ZA)$) and it is lower at higher ZA. Thus, between different parts of the camera can appear a disuniformity which approximately runs along the zenith angle direction, giving "hotter" regions (that is, with more reconstructed events) at small zenith angles, and "colder" at higher ZA. This effect appears more prominent for values of $ZA > 30°$.

Such systematic appears clearly in the Cas A data sample [18] (with an average ZA of 32°) which amounts to more than 200 hours taken in *wobble mode*. If we split the Cas A data in the two subsets $\pm 0.5°$, the effect clearly appears in the 2D-map of the reconstructed events (after the correction for the fall-off radial acceptance) (see Fig.8.2) and amounts to a variation of around $\Delta_{ZA} \sim 10\%$/deg from the tracking point along the ZA direction (for a trigger multiplicity $n_{tel} \geq 3/5$ and a shape cut $\langle \tilde{w} \rangle$ <1.1).

The gradient effect can be corrected fitting the map of reconstructed events (already corrected for the radial acceptance) with a plane $F = a + b \cdot x + c \cdot y$ and subtracting the same to the data. Figure 8.3 shows how the 2D-map appears after the correction for the gradient effect.

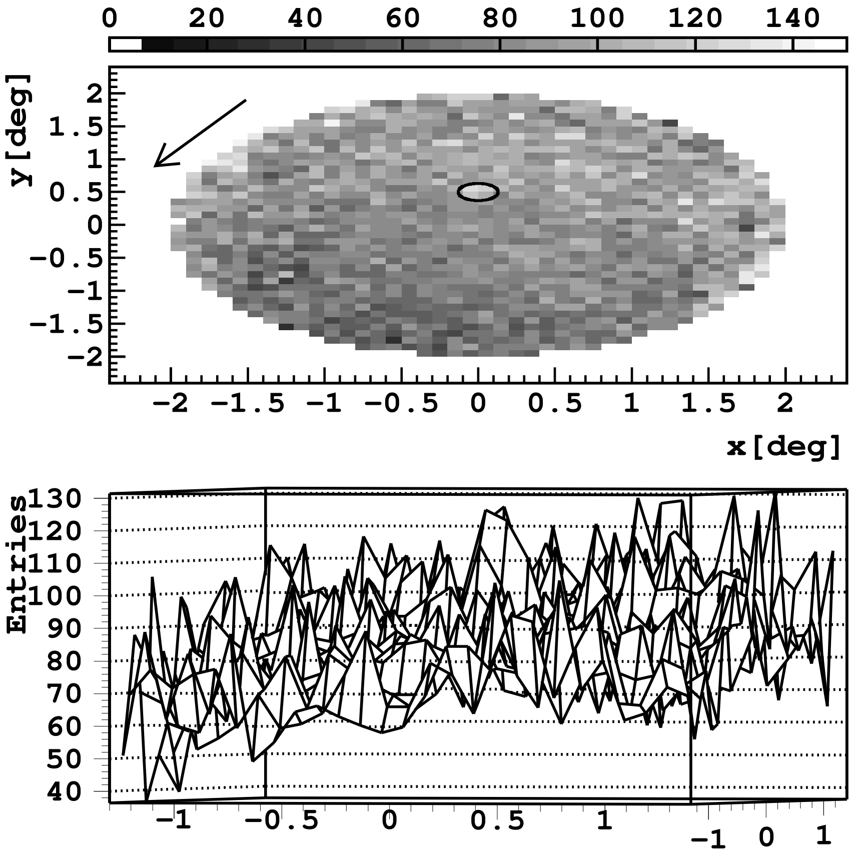

Figure 8.2: *Upper panel: Map of the stereo-reconstructed events detected from the direction of the Cas A SNR. The point-like source position is indicated by the black circle. The arrow shows the direction of increasing ZA. Lower panel: parallel view to the x-y plane where is clearly visible the gradient along the ZA direction.*

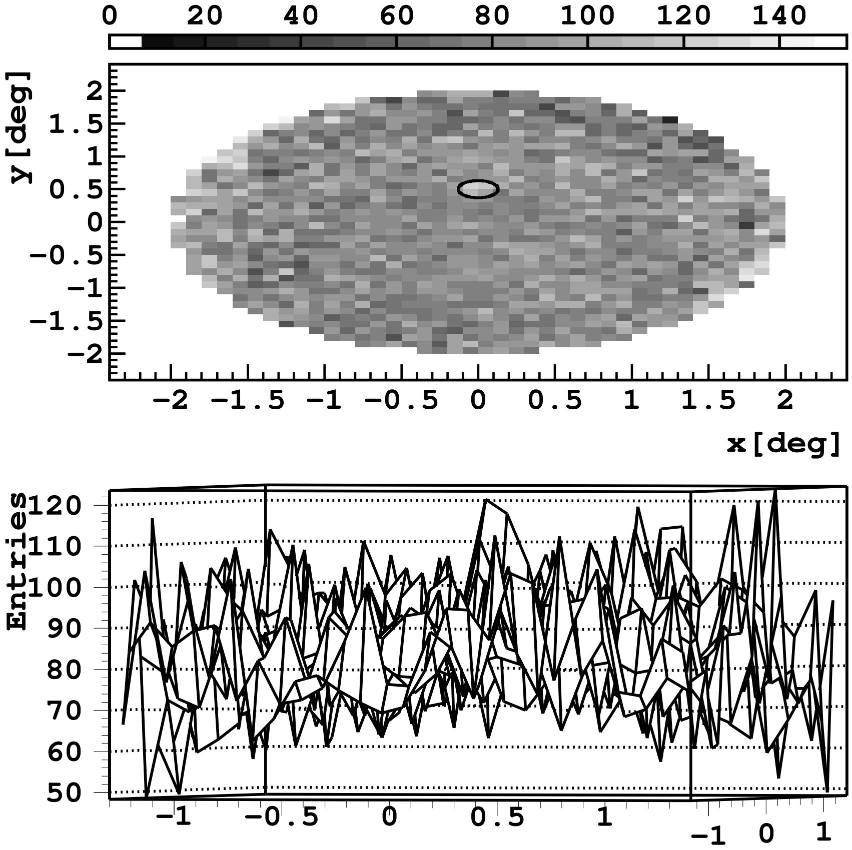

Figure 8.3: *Upper panel: Map of the stereo-reconstructed events from the direction of the Cas A SNR after the correction for the gradient effect. Lower panel: parallel view to the x-y plane.*

This problem obviously affects the determination of the CR background content directly from a sample of ON data, especially for the *template model* and the *wobble approach* using n symmetrical OFF regions. A gradient of 10%/deg translates on a difference in significance up to 1 sigmas.

In the Monoceros data sample (with an average ZA of 26°) this effect appears negligible (see Fig. 8.4), amounting just to a $\Delta_{ZA} \sim 1\%/deg$ which affects the estimate of the significance by just a few tenths of sigmas (0.1-0.2).

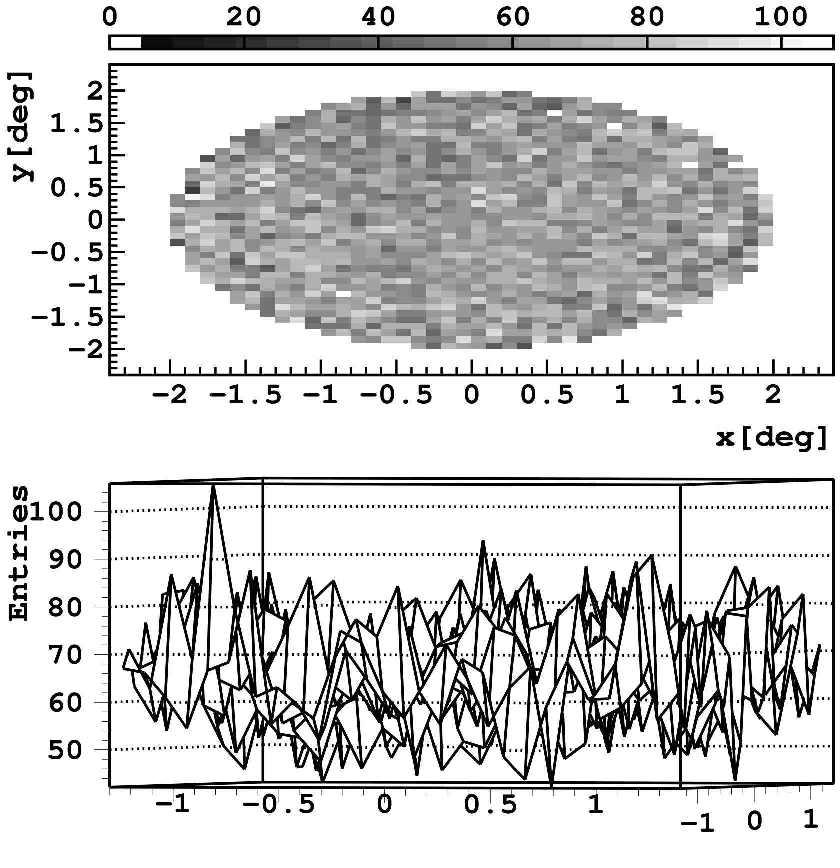

Figure 8.4: *Map of the stereo-reconstructed events detected from the direction of the Monoceros Loop SNR region. In this case, the FoV looks uniform and the correction to the ZA gradient effect is negligible (variations of 1%/deg).*

List of Figures

List of Tables

Acknowledgements

First of all, I would like to thank you Dr. M.V. Fonseca, for her support and encouragements in all the moments of difficulty; Dr. Konopelko, whom it was a real pleasure to work with and greatly contributed to my professional growth; Dr. F. Aharonian, for giving me the opportunity to stay in the HEGRA group of the "Max Planck Institute für Kernphysick" and make this thesis a reality.

I also acknowledge all the members of the HEGRA collaboration which have contributed to this work either having built the system or as shift observers or making the data calibration.

In particular, I would like to thank: M. Girma and H. Lampeitl for the helpful discussions and J.Kettler for his nicely friendship.

I thank a lot all the people here in Madrid as well, which has supported and helped me (and taught Spanish, too) all along the PhD duration: J.L. Contreras, A. Moralejo, J. Barrio, L.Padilla, A.Ibarra, I. de la Calle, M. Lopez, E. Ona, R. de los Reyes, N. Sevilla.

I would like to thank you as well all my friends in Heidelberg, who have made my stay "in the wood" very pleasant: S. Ligori, M. Marcello, S. "abbasso Roma" Salvatori, L. "Juve in B" Pentericci, C. Tomei, E. Katragkou, G. Rowell, D. Horns.

To end, a very special acknowledgement to my father, my mother and my grandma.

I apologise those ones who I forgot to mention.